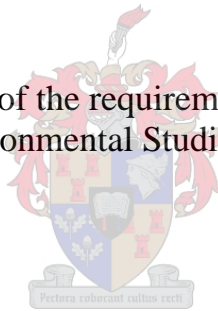# Mountain wave turbulence in the lee of the Hex River Mountains

By

Deon Van Der Mescht

Thesis presented in fulfilment of the requirements for the degree of Master of Science in Geography and Environmental Studies at the Stellenbosch University.

Supervisor: Mr PJ Eloff
Faculty of Arts and Social Sciences
Department of Geography and Environmental Studies

March 2012

Declaration

By submitting this thesis electronically, I declare that the entirety of the work contained therein is my own, original work, that I am the sole author thereof (save to the extent explicitly otherwise stated), that reproduction and publication thereof by Stellenbosch University will not infringe any third party rights and that I have not previously in its entirety or in part submitted it for obtaining any qualification.

March 2012

ABSTRACT

Despite recorded mountain wave related aircraft accidents in South Africa, very little literature exists on South African mountain waves. This study discusses the results of a mountain wave study in the Hex River Mountains in the Western Cape province of South Africa. The aim of this study was to measure mountain wave turbulence on the lee side of the mountains by conducting weather balloon soundings on the upwind and lee sides of the mountains. These soundings were performed over four days in the winter and spring, with each field day representing different synoptic scale weather conditions. Lee wave rotors were detected from several of the lee wave soundings. Significant values of horizontal vorticity around a north-south axis (y-component horizontal vorticity) were detected. The instrumentation was highly sensitive and able to measure even weak up and downdraft velocities associated with the rotors. Strong downdrafts were measured in some mountain waves, but no strong downdrafts were detected near rotors which occurred below the mountain waves. The two dimensional positions of balloons were only available after a considerable amount of reanalysis. If this data can be made available onsite shortly after soundings, it can be used to decide where to move launch sites to, in order to obtain optimal results.

Keywords: balloon soundings, mountain waves, rotors, y-component horizontal vorticity

OPSOMMING

Ten spyte van gedokumenteerde berggolf-verwante vliegongelukke, bestaan baie min literatuur oor Suid Afrikaanse berggolwe. Hierdie tesis bespreek die resultate van 'n berggolfstudie in die Hexrivier Berge in the Weskaap Provinsie van Suid-Afrika. Die doel van hierdie studie was om die berggolfturbulensie aan die lykant van die berge te meet deur middel van weerballonopstygings aan beide die wind- en lykante van die berge. Hierdie opstygings is oor 'n tydperk van vier winter en lente dae uitgevoer, met elkeen van die dae wat verskillende sinoptiese weersomstandighede verteenwoordig het. Rotors is waargeneem in die data van verskeie ballonopstygings wat aan die lykant uitgevoer is. Beduidende waardes van horisontale vortisiteit rondom 'n noord-suid as (y-komponent horisontale vortisiteit) is gemeet. Die instrumentasie was hoogs sensitief en kon selfs swak op- en afstrominge meet. Sterk afstrominge is waargeneem in berggolwe, maar nie in die omgewing van rotors wat onder die berggolwe voorgekom het nie. Die twee-dimensionele posisies van ballonne was slegs na aansienlike heranaliese van die data beskikbaar. Indien hierdie data kort na opstygings beskikbaar is tydens veldwerk, kan dit help met besluite oor alternatiewe posisies waarvandaan ballonopstygings gedoen kan word ten einde optimale resultate te bekom.

Sleutelwoorde: ballonopstygings, berggolwe, rotors, y-komponent horisontale vortisiteit

ACKNOWLEDGEMENTS

The author wishes to thank the following individuals and organizations for their support:

Dirk Uys from Aircraft Owners and Pilot's Association of South Africa for a reconnaissance flight over the study area and the use of a vehicle during the first field trip.

Intermet Africa for the use of their sounding equipment, technical support, software support and research material.

Didi and Waldo from the Matroosberg Reserve for accommodation and technical support during the first field trip.

Colleagues from the South African Weather Service: Karen Marais and Anastasia Demertzis for assistance with research material, Colleen de Villiers for supplying automatic weather station data and Tennielle Jacobs for advice on structural elements of the thesis.

Chris Booysens from the South African Aero Club for supplying topographic maps on CD.

Pilots Chris van Hoof, Richard Sandy as well as members of the Stellenbosch Flying Club for financial assistance.

Jonathan Smailes for his assistance during the second field trip.

The author's wife, Michelle, for support and patience during the months of work on the thesis.

CONTENTS

LIST OF TABLES

LIST OF FIGURES

LIST OF APPENDICES

LIST OF ACRONYMS USED IN THE TEXT

ACSL	altocumulus standing lenticularus
AIRMET	Airmen's Meteorological Information
AGL	above ground level
AMS	American Meteorological Society
AWS	automatic weather station
GMT	Greenwich Meridian Time
ISA	International standard atmosphere
JSP	Mountain Wave-Jet Stream Project
K-H	Kelvin-Helmholtz
KIAS	knots indicated airspeed
LIDAR	Light Detection And Ranging
METAR	Meteorolgical Aviation Routine (Report)
MSL	above mean sea level
NCEP	National Centers for Environmental prediction
NTSB	National Transport Safety Board
NWP	numerical weather prediction models
RAMS	Regional Atmospheric Modeling System
RASS	Radio Acoustic Sounding System
SACAA	South African Civil Aviation Authority
SAWS	South African Weather Service

SODAR   Sonic Detection and Ranging

SRP   Sierra Rotors Project

SWP   Sierra Wave Project

T-REX   Terrain-Induced Rotor Experiment

WMO   World Meteorological Organisation

CHAPTER 1 INTRODUCTION TO MOUNTAIN WAVES AND THE RESEARCH PROJECT

1.1   Definition of mountain waves

The American Meteorological Society (AMS) defines a mountain wave as an atmospheric gravity wave which forms in the lee of a mountain barrier as statically stable air passes over the barrier (AMS 2010). A gravity wave is a wave disturbance in which buoyancy acts as the restoring force for air particles that have been displaced from a state of constant density and pressure (Huschke 1959). Statically stable air is air that tends to become or remain laminar due to the effects of buoyancy (AMS 2010).

1.2   Classes of mountain waves

Caccia, Benech & Klaus (1997) explains that when wind direction is perpendicular to a mountain barrier, the air accumulation on the upwind side creates a high pressure zone. This slows the incident flow of air. Part of the air is deflected upward resulting in the formation of mountain waves on the lee side of mountains.

Two classes of mountain waves are identified: vertically propagating lee waves and trapped lee waves (AMS 2010; Barry 1981; Caccia, Benech & Klaus 1997; Vieira 2005). In vertically propagating wave theory, Barry (1981) states that no part of the air flow radiates downward. The wave amplitude does not decay with height. Vieira (2005) mentions that vertically propagating waves can extend to the troposphere. Vertically propagating waves are formed when the Scorer parameter (see Section 2.5.2) either increases with height or is more or less uniform with height (Caccia, Benech & Klaus 1997). Durran (2003) explains that vertically propagating waves tilt upwind with height.

Conversely, in the case of trapped lee waves, flow radiates downward which results in some wave energy being ducted (Caccia, Benech & Klaus 1997). According to Durran (2003) trapped lee wave amplitude decays exponentially with height and does not tilt with height. Trapped lee

waves are generally confined to altitudes below 25 000 ft (Vieira 2005). Trapped waves are formed when the Scorer parameter decreases with height (Barry 1981; Durran 2003). The satellite imagery used by the South African Weather Service (SAWS) indicate that mountain waves over the Western Cape are predominantly formed within middle level altocumulus as opposed to high level cirrus (Smit 2010, pers com). Muller (2010) states that vertically propagating waves are associated with high level cirrus cloud. This study only focuses on trapped lee waves.

1.3   Features of trapped lee waves

The features of trapped lee waves are illustrated in Figure 1.1. The windward side of the mountain in Figure 1.1 is to the left of the barrier and the lee side to the right of the barrier. The amplitude of the waves diminishes with height. Reichmann (1978) mentions that gliders flying in the actual wave crests and troughs, experience smooth flying.

Barry (1981) states that all mountain wave clouds are stationary with respect to the surface of the Earth. Within the lee wave individual clouds constantly form on the windward side of the mountain and dissipate on the lee side. Cap cloud can form over a ridge when air is forced to rise against the ridge to its saturation level (Barry 1981). On the lee side of the mountain, the cloud base is near or below the top of the barrier. The cloud mass has a smooth upper outline with the lee side often appearing as a wall with fibrous elements dissipating on the lee side, downward from the cloud. World Meteorological Organisation (WMO) (2009) add that the tops of the cap cloud can extend to several thousand feet above the top of the barrier while the bulk of cloud mass is situated on the windward side of the mountain.

When sufficient moisture is available, clouds can develop at wave crests (Welch 1973). They are called lenticular clouds. These clouds are shaped like lenses or almonds and form mostly as middle and high cloud, and seldom as low level clouds (Huschke 1959). In Figure 1.1 Hertenstein & Keuttner (2005) uses altocumulus standing lenticularus (ACSL). Barry (1981) points out that lenticular cloud appear in regularly spaced bands to the lee of the mountain.

Hertenstein & Keuttner (2005) refer to the turbulent flow (See A.1, Appendix A) below the laminar mountain wave as 'rotor'. They identify two types of rotors: a type 1 rotor occurs under the crest of mountain waves of a trapped lee wave system, while a type 2 rotor is associated with a high amplitude wave resembling a hydraulic jump associated with vertically propagating wave systems. Turbulence within the type 1 rotor is classed as moderate to severe while type 2 rotors contain severe to extreme turbulence. Type 1 rotor areas are indicated by 'R' in Figure 1.1. Given enough moisture, clouds can form in this area, which are referred to as rotor clouds or roll clouds. Rotation in these clouds is visible in time-lapse photography. These clouds mainly form under the crest of the primary wave (Barry 1981). According to Huschke (1959) rotor clouds typically belong to the cloud specie fractus, due to the ragged shredded appearance. Rotation is about an axis parallel to the mountain range. Gliders are often towed through the rotor zone by powered aircraft. Reichmann (1978) mentions that flights through the rotor area experience strong turbulence with instant altitude changes of 1600 fpm (6 ms^{-1}) to 2000 fpm (10 ms^{-1}). The red and blue arrows in Figure 1.1 show areas of downdraft and updraft respectively.
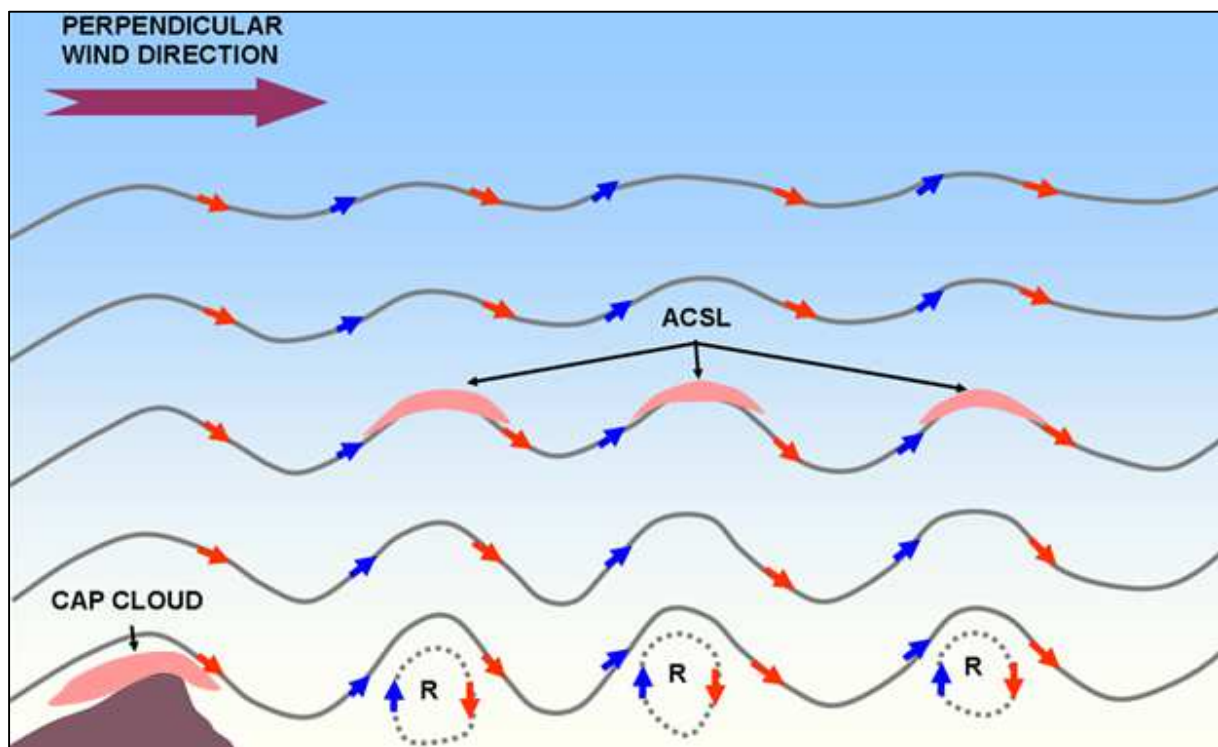
Source: Hertenstein & Keuttner 2005: 118

Figure 1.1: Features of trapped lee waves.

Along the wave itself, transition from down to updraft areas occur rather smoothly, whereas within the rotor area there are abrupt changes from downdraft to updraft. Mobbs *et al*. (2005) point out that rotors often measure less than two kilometres across, making it impossible to resolve explicitly with numerical weather prediction models (NWP). Koch *et al.* (2006) mention a very important fact that trapped lee waves could aid in the development of rotors.

1.4   Prerequisites for the formation of mountain waves

Barry (1981) states that mountain wave development requires an upwind wind direction through a deep layer of the atmosphere which is perpendicular to the mountain barrier, or at a variance of no larger than 30° from perpendicular. A summit wind speed of at least 7 ms^{-1} for mountains of about 1000 m in height and 15 ms^{-1} for mountains of 4000 m in height is a further requirement. Leeb-du Toit (2006) estimates the required speed for South African summit winds at 8 ms^{-1}. Lindsay (1962) highlights a further necessary condition of decrease in Scorer parameter with height for the formation of trapped lee waves (see Section 2.5.2). Such a decrease is attained due to either an increase in wind speed with height or a decrease in stability with height. He found that most studies showed that these speed and stability conditions co-exist during the formation of mountain waves.

Leeb-du Toit (2006) further mentions that a requirement for mountain wave development is a layer of low stability at low levels, a more stable layer above that and finally an upper layer of low stability above the stable layer (see A.2, Appendix A). Atkinson (1981) also addresses the issue of stability and states that based on results from the Sierra Wave Project, the lower layer of unstable air needs to be confined to an area below 850 hPa (5000 ft), the middle stable layer between 850 and 700 hPa (10 000 ft) and the upper unstable layer above 700 hPa. In more general terms this means that there should be marked stability at least at levels where the air is disturbed by the mountain. While the magnitude of parameters observed in the Sierra Wave Project and other studies may be significantly different from that of the Hex River data, it is expected that the basic prerequisites for trapped lee development will be detected data from this study.

The shape of the mountain barrier also plays an important role in the development of mountain waves. Barry (1981) mentions that steep lee slopes create more turbulent flow than gradual slopes. Sudden breaks in the slope causes the laminar flow of air to separate and eddies to develop. Atkinson (1981) states that the amplitude of a lee wave is determined to a larger extent by the width of the barrier than by its height. He considered different half-widths of mountains and the effect that asymmetrical ridges have on the location and amplitude of lee waves. Lilly & Klemp (1979) discussed the equations describing different mountain shapes and their effect of airflow over the tops of these shapes. They found that the equation relating to an asymmetric shape with a gradual upwind slope and a steep lee slope, served to model the real life strong lee waves well for such mountain shapes in the USA, notably in areas of the central Rockies, Canadian Rockies and Sierra Nevada. Reichmann (1978) briefly highlights three terrain features favourable for lee wave development: a relatively steep lee side slope, relatively smooth surface and a ridge line long enough so that air does not simply flow around the sides, but is forced over the top.

1.5   Literature review

1.5.1   Historic Overview

Grubišić & Lewis (2004) list papers by Queney as some of the first published studies on mountain waves. Queney investigated strong synoptic scale weather systems passing over France and Spain and moving over the Atlas Mountains in North Africa. He was able to illustrate a relationship between the wavelength of the mountain profile, stability of the atmosphere and the speed of airflow over the mountain.

Keuttner's first two papers published in 1939 mentioned the quasi stationary nature of lee waves (Alaka 1968). Being a glider pilot, he was also able to use the strong vertical currents himself to reach altitudes of 8000 m and more. He measured the up- and downdrafts of rotors and also noted that not all mountain wave events are associated with clouds. According to Grubišić & Lewis (2004), Keuttner's papers were based on a data set of 22 flight reports from 25 gliders that spent 65 combined flight hours in one wave system, on 21 May 1937.

In 1945 Manley published results of a 1937-39 study in the English Pennines (Alaka 1969). Manley noted that the lee slope winds are stronger than that at the summit. Local inhabitants refer to this wind as the Helm wind. Manley also observed the Helm Bar, which is a cigar shaped rotor cloud that forms in the western lee of the Pennines. An interesting observation that he made, was that the surface wind below the rotor was often opposite to the general direction of movement of the wave system and upper winds. Grubišić & Lewis (2004) also mention that Manley suspected that the Helm cloud was associated with a strong inversion and a stable layer of air that overlies it.

According to Alaka (1968), Förchgott wrote in 1949 about the importance of the lee slope shape and the need for increased wind speed with height, for the development of waves. Förchgott also highlighted the importance of the wind direction approximately perpendicular to the ridge and stable air upwind from the mountain barrier.

Alaka (1968) also mentions the work of Larsson, published in 1954. Larsson studied the formation of lenticular cloud in the central Swedish mountains. Larsson added a number of new ideas. He noted that ascending air into the wave cloud was often moving much faster than the descending air leaving the cloud. He also observed that the distance between the mountain top and the first wave was smaller than the wavelengths further downstream. Lastly, Larsson found that a summit wind of 20 kt (10.3 ms^{-1}) was necessary for the development of wave and for the development of stacking in the cap cloud, a 30 kt (15.4 ms^{-1}) summit wind was needed. Stacking refers to the development of multiple lenticular cloud layers developing over the mountain peak, resembling a stack of overturned dinner plates.

In the 1950s two major field experiments were conducted. These were the Sierra Wave Project (SWP) of 1951 and 1952 (Holmboe & Klieforth 1957) and a follow-up project in 1955, which Grubišić & Lewis (2004) termed the Mountain Wave-Jet Stream Project (JSP). In the first part of the SWP study, two glider aircraft were used to collect data, while being remotely tracked by theodelite. In the final two months of the SWP, a powered tow aircraft was also used for the collection of data. Since no logging of instrument data was possible, the flight instruments were

filmed and the footage correlated with other data. Further data was acquired from balloon soundings, time-lapse photography of cloud from the ground, ground based fixed weather stations and a mobile weather station. During the project a team member suggested that the theory of an atmospheric hydraulic jump to be applied to certain mountain waves. The US National Weather Service (National Weather Service 2011) defines a hydraulic jump as an atmospheric disturbance on the lee side of a mountain, within which air blows over the mountain at high speed and low depth over the mountain and changes to a an area of low speed and high depth. A hydraulic jump is thus associated with vertically propagating waves and not trapped lee waves. The 1955 JSP saw the addition of two research aircraft, both converted World War II bombers. These aircraft made atmospheric measurements between 20 000 and 40 000ft. Planning for research flights were based on forecasts performed 48 hours ahead. For the JSP a classification of mountain waves was performed (Grubišić & Lewis 2004) which is shown in Table 1.1. The maximum altitude variation is the vertical distance between a wave crest and a wave trough. Two very significant aircraft observations were made during JSP. On 1 April 1955, one of the bombers experienced 13 vertical gust velocities exceeding 9 ms^{-1}, within a 50 second period. On 25 April 1955 a glider broke up in flight due to the severe turbulence it encountered at an altitude of 17 000 ft near a rotor cloud (Ferguson 2010). The pilot parachuted to safety. He recalled how some of the lighter aircraft debris was carried upward past him, into the rotor cloud.

Table 1.1: Classification used by JSP

	STRONG	MODERATE	WEAK
Wavelength (km)	13-32	8-13	4-8
Max Alt variation (m)	1200-2400	600-1200	150-600
Vertical updraft/downdraft speed (ms^{-1})	9-18	4.5-9	1.5-4.5

Source: Grubišić & Lewis 2004: 1135

Alaka (1969) also mentions the work of Gerbier and Bérenger conducted in the winters of 1956, 1957 and 1958 in the French Basses-Alps. Constant level weather balloons, conventional weather balloons, powered aircraft and gliders were used in the investigations of mountain waves

in this experiment. Photographs taken from the ground and air were also incorporated into the study. The Gerbier and Bérenger study revealed much about the influence of the shape of topography. They found that for optimal wave development, long mountain barriers were favoured over isolated peaks, concavely shaped windward slopes favoured over convex-shaped windward slopes and on the lee side, steeper slopes were more conducive to the development of turbulent eddies than gentle lee slopes. Gerbier and Bérenger also concluded that mountain ranges that are in phase with the mountain waves, in other words mountain ranges a multiple of a mountain wave length from one another, will enhance the amplitude of the wave over the mountain downstream. Conversely, where two ranges are a distance apart that is not a multiple of the mountain wave wavelength, wave amplitude degeneration will take place. Their study further investigated the structure of the wind profile. They found that for their study area the optimal wind direction was within 30 degrees from perpendicular to the crest of the mountains, with a summit wind of at least 10 ms^{-1}. Gerbier further found that long wave lengths were associated with strong winds. When it came to static stability, he also proved that a larger than usual amount of stability was needed for wave formation with wave amplitudes increasing and wavelengths shortening with increased stability. Next Gerbier and Bérenger observed rotor formation with reversed flow near the surface of the valley and the base of the rotor at approximately the same altitude as the mountain tops. They also obtained numerical values of vertical currents.

Lindsay (1962) studied 51 cases of mountain waves in the Appalachian Mountains in the eastern United States of America. He collected data on downdrafts, updrafts and turbulence from pilot reports. His observations also included G-force estimates from the pilots and some use of radar data. Lindsay found that 80% of the mountain waves in his study occurred within 320 km of a jet stream. A jet stream is a narrow band of relatively strong, quasi-horizontal winds with speeds in excess of 50 kt (25.7 ms^{-1}) mainly found as mid latitude westerlies in the high troposphere (Huschke 1959). De Villiers & van Heerden (2001) mention that in their study of clear air turbulence, mountain wave induced turbulence was at times detected horizontally far ahead (to the east) of a jet stream as well as well below the level of the jet stream. Lindsay further concluded that winds at the 850 hPa level exceeding 40 kt (20.5 ms^{-1}) were generally too strong

to generate mountain waves. This observation was also made during SWP, where too strong jet streams wind speed would break up the wave.

In the 1970's some research was conducted on down-slope wind storms. A storm of 11 January 1972 was discussed by Lilly & Zipster (1972) where, with the help of aircraft data, a correlation between down-slope wind storms and mountain wave activity was made. Brinkman (1974) also refers to this storm in his paper where he studied the results of 20 wind storms with maximum speeds exceeding 22 ms^{-1}. He pointed out that the down-slope wind storms were linked to the stability profile of the lower atmosphere. Papers on down-slope wind storms were also written in the 1980s, with Durran (1986) making a significant contribution by discussing numerical model simulations, in the process again revisiting the Boulder, Colorado wind storm of 11 January 1972. Wolyn (2003) made use of numerical weather prediction models (NWPs) in a remote, data-scarce part of Colorado, to investigate mountain wave induced wind storms. NWP products with 40 km grid resolution were re-run for dates on which storm damage was reported.

In 1991 mountain wave experiments were conducted in the English Lake District (Vosper & Mobbs 1996). Upper air soundings were conducted in the lee of mountains with balloons launched about ten minutes apart. Observations were also gathered from a research aircraft. The different trajectories of the balloons enabled researchers to determine the vertical tilt of the waves with height. Vosper & Mobbs (1996) found that very little vertical tilt of waves was experienced in the presence of trapped lee waves. Numerical simulations of the observations were also made.

Two studies were conducted on rotors in the Owens Valley of the Sierra Nevada Range in 2004 and 2006. The first was called the Sierra Rotors Project (SRP), which is discussed by Grubišić & Billings (2007). SRP used a network of 16 automatic surface weather stations (AWS) arranged in three parallel rows; a radar wind profiler, upper air soundings as well as a radio acoustic sounding system (see Appendix A, A.3). The evolution of a single mountain wave event was observed. Over a 24 hour period a small amplitude trapped lee wave developed into a large amplitude wave which generated strong down-slope winds. Later in the evolution rotor activity was observed as well as wave breaking.

In 2004 and 2006 the Terrain-Induced Rotor Experiment (T-REX) was conducted in the Owens Valley (Doyle *et al.* 2009). This project used two Doppler LIDARs, one aerosol LIDAR, three SODARs, three radio acoustic sounding systems (see A.3 and A4, Appendix A), three radar wind profilers and the same AWS network as was used in SRP. The instrumentation successfully measured the speed of the airflow as well as the horizontal vorticity of the rotor below the wave crest. Vorticity is a vector value describing rotation in a fluid around an axis (Huschke 1959). In the case of horizontal vorticity, the rotation is along an axis parallel to the surface of the earth. In reference to T-REX, Hertenstein & Keuttner (2005) further discuss horizontal vorticity of rotors, using it to distinguish between type 1 and type 2 rotors.

According to Atkinson (1981) a complete climatology of mountain waves remains incomplete. To this end, any study of mountain waves in new areas on the planet, increases the data base in order to establish such a complete climatology.

1.5.2   Aircraft accidents: Airliners

Mountain wave turbulence has been the cause of airline accidents and incidents. Three cases are highlighted. The most recent accident report from the United States National Transport Safety Board (NTSB 2010) describes how mountain wave induced wind shear lead to the loss of directional control of a B737-500 at Denver International Airport, Denver, Colorado on 20 December 2008 during take-off. The aircraft veered off the runway and crashed. 38 occupants of the aircraft were injured. A crosswind of 15.5 ms^{-1} gusting to 20.5 ms^{-1}, was recorded.

On 31 March 1993 a Boeing 747 lost an engine in severe to extreme turbulence, believed to be caused by mountain waves, after taking off from Anchorage International Airport, Alaska (Krause 2003). The incident occurred at 2000 ft above ground level (AGL) where the aircraft experienced a sudden drop in airspeed from 245 kt to 170 kt (Flight Simulation Systems 2006). According to Davis (2010) the loss of airspeed may have been due to the pilot pulling up the nose in an attempt to compensate for loss of altitude due to a downdraft.

On 9 December 1992 a DC8 cargo aircraft lost an engine and a large part of its wing while encountering severe turbulence at 31 000 ft, 36 kilometer miles west of Denver Colorado (Aviation Safety Network 2010). Nance & Colman (2000) mention that this accident coincided with a down-slope wind storm in the lee of the mountains. According to Durran (1986) downslope wind storms can reach gusts as high as 60 ms^{-1} and are associated with vertically propagating waves.

De Villiers & van Heerden (2001) mention injuries sustained during an airline flight through clear air turbulence (CAT) over South Africa during January 1994. They do not state whether this turbulence was related to mountain waves.

1.5.3   Aircraft accidents: General aviation aircraft

The crash of a twin engine Aero Commander light aircraft in Eagleville, California on 21 November 2001 was reviewed (NTSB 2006). The five occupants of the aircraft were killed. The investigation revealed that at the time of the crash, a high likelihood existed for the presence of severe to extreme turbulence between 9500 and 11 000 ft. Updrafts of 10.1 ms^{-1} were reported, indicative of mountain wave turbulence. A severe downdraft was observed by another pilot near the crash site.

In South Africa a single engine Piper aircraft crashed on the western slopes of Table Mountain on 31 December 1985. According to Elzinga (2010, pers com) the official report issued by the Department of Civil Aviation stated that in spite of moderate south to southeast flow, turbulent conditions were expected on the lee side of the mountain. Eye witnesses reported seeing the smoke from the post crash fire move down the mountain slope, indicative of a downdraft. Take-off winds were 190° 22 kt (11 ms^{-1}) and increased to 180° 37 kt (19 ms^{-1}) by the time of the accident. The low level winds quoted in the accident report were 125° 6 kt (3 ms^{-1}) at 2500 ft and 150° 10 kt (5 ms^{-1}) at 3200 ft. These figures could only have originated from a midday balloon sounding which would have made the data at least five hours old.

On 8 January 2005 another light aircraft crash occurred in the Hex River Mountains, thus in the study area (SACAA 2010). There was one fatality and one serious injury. The South African Civil Aviation Authority sited predominant downdrafts within the valley which the aircraft was flying in as contributing factor to the accident. Malan (2010, pers com) mentioned that the pilot of a rescue helicopter, which performed the rescue of the survivor, also reported experiencing turbulence from downdrafts during the rescue operation.

The literature review summarised the history of mountain wave research, including some details on the research methodology. The dangers of mountain wave turbulence to both airliners and general aviation aircraft were highlighted by including examples from accident investigation reports. These included accidents in South Africa.

1.6 Research problem

Although the literature review revealed several large scale studies conducted over six decades in many parts of the world, only two articles were found describing South African examples of mountain waves (Leeb-du Toit 2006; de Villiers & van Heerden 2001). De Villiers & van Heerden (2001) discuss clear air turbulence caused by mountain waves. They mention that there may be a link between trough systems and the occurrence of mountain wave CAT near the Western Cape mountains. The literature review further highlighted that fatal mountain wave related aircraft accidents have been recorded in the Western Cape.

According to Bester (2010, pers com) it is common practice for gliders to be towed through certain rotor zones below wave crests by light aircraft. These light aircraft experience turbulence from the rotor zone more acutely than the gliders that they tow. The Cape Gliding Club (2010, pers com) pointed out that rotors in the lee of the Hex River mountains are particularly turbulent.

No literature could be found describing the nature of lee side turbulence associated with mountain waves in South Africa. In order to measure turbulence of such a nature, balloon soundings on the lee side of mountains need to be conducted. To improve the forecasting of

such events, the synoptic scale weather systems active during the soundings need to be documented as well.

1.7   Research aim

The aim of this study is to measure mountain wave rotor turbulence with the aid of weather balloon soundings on the lee side of the Hex River Mountains.

1.8   Research objectives

To achieve the aim of this study the following objectives were set:

1. Conduct a literature study of all the necessary aspects of mountain waves that will allow for a thorough study of its induced turbulence.
2. Identify a study area in the Western Cape where the best examples of mountain wave turbulence are likely to be found.
3. Forecast suitable weather events during which field work can be conducted.
4. Conduct weather balloon soundings on the windward and lee side of the study area.
5. Re-analyse the surface and synoptic scale weather data during each day of field work.
6. Analyse the sounding data to measure the effect of turbulence.

1.9   Study area

Following a meeting with the Cape Gliding Club, the Hex River Mountains were chosen as the study area for this project. The range is orientated approximately SW to NE. It is about 11 km wide and 45 km long. On the upwind side the terrain rises from 1200 m above MSL to an average ridge elevation of 1800 m over a horizontal distance of approximately 5 km, and drops on the lee side from the ridge to the same elevation over an average horizontal distance of 2.5 km.

The upwind atmospheric study area was situated to the west of Matroosberg in the Matroosberg Reserve (indicated by 'S1' in Figure 3.6), while the Hex River Valley (De Doorns district) on the eastern side served as study area for lee atmospheric measurements. The location of De Doorns

is indicated by a red dot in Figure 1.2. The Hex River Mountains is the mountain range situated to the north west of De Doorns.   Upwind data was limited to the lower approximate 3500 – 4000 m above MSL as above that level the balloons crossed to the lee side of the Hex River Mountains. On a second field trip the upwind sounding site was moved to the Wolseley district which resulted in the upwind data stretching to 7400 – 8000 m above MSL.
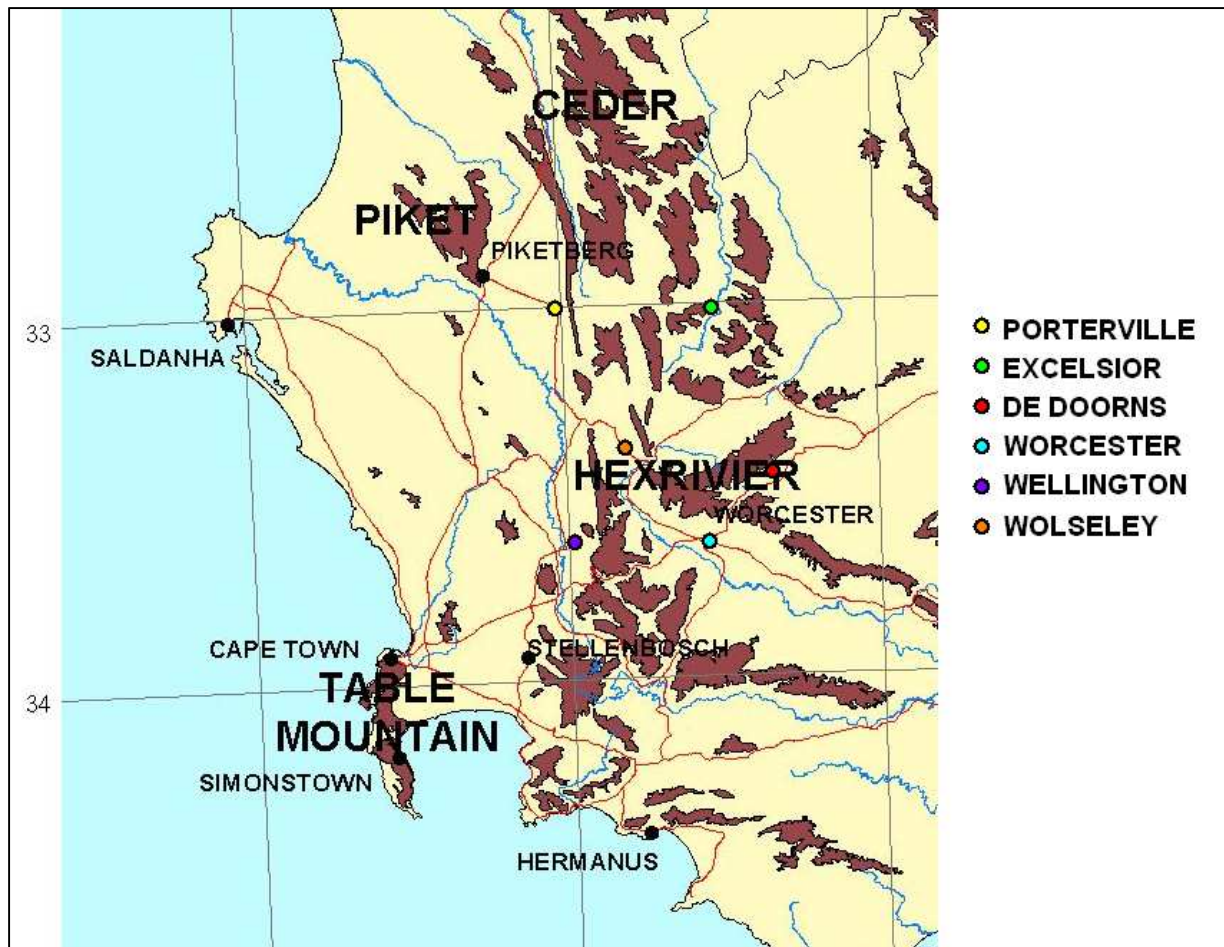
Source: Breedlove and Fraser (2011)

Figure 1.2: Map of the study area. Mountains are indicated by brown areas.

The following chapter deals with the acquisition and processing of data. The main focus is on the hardware used as well as formulas used to process the data.

CHAPTER 2 DATA COLLECTION AND PROCESSING

2.1 Forecasting mountain wave events

Leeb-du Toit (2006) explains that mountain waves in the Worcester area form in the northwest winds, ahead of an approaching cold front and after a high pressure system has created a strong temperature inversion. As an indicator of the frequency of winter mountain waves over the study area, the monthly total of Airmen's Meteorological Information reports (AIRMETs) containing mountain wave warnings over the study area was plotted for April through August for the period 2005 through 2009. This is shown in Table 2.1. Months with 15 days or more of predicted mountain wave events are highlighted in yellow. There is a clear increase in the number of mountain wave events forecasted during the last three years. This is due to the improvement in the resolution of satellite images used as a now-casting tool by the South African Weather Service (SAWS) in which all forecasters received training between 2005 and 2007 (de Coning, 2011 pers com). This data set is small but served as the best indicator during which months the mountain wave frequency peaked. Based on the data of Table 2.1, preparations were made for the fieldwork during July or August. Two mountain wave events were forecast spanning 22/23 July and 17/18 September 2010. The first field trip was conducted in pre-frontal and post frontal conditions. The second field trip was conducted during the time of an approaching cut-off low. It allowed for comparison of data under different synoptic conditions. North westerly winds ahead of an approaching trough system (Leeb-du Toit 2006), were used as the prime tool to forecast possible mountain wave events for the field trips.

Table 2.1: Monthly totals of mountain wave warnings issued

YEAR		2005	2006	2007	2008	2009
MONTH	APRIL	4	3	7	7	6
	MAY	10	9	13	17	20
	JUNE	9	9	14	16	18
	JULY	8	12	19	21	15
	AUGUST	14	9	16	16	21

2.2   Sounding hardware and software

As mountain waves are atmospheric events, their features are best detected with the use of weather balloon soundings. Sounding data often featured in large scale mountain wave research projects e.g. Vosper & Mobbs (1996), Reid (1972), Lalas & Einaudi (1980), Shun *et al.* (2004), Shutts *et al.* (1994), to name but a few.

The soundings for this study were performed using an Intermet Africa/Diel iMet-3200 portable antenna receiver unit, iMet-2-AA radio sondes, hydrogen gas and 100 g Totex balloons. Power was supplied by a laptop computer. The laptop's power was supplemented by a battery charger run from a vehicle's cigarette lighter. This set-up made the sounding equipment mobile and thus allowing up to two ascents per hour from a remote site. The radio sondes were equipped with frequency selections, which prevented the antenna from receiving a signal from a radio sonde still airborne at the time of a second sounding. Sounding data was calculated by the D-Met software from the Intermet Africa/Diel Company. It comprised one-second interval data.

2.3   D-Met sounding data

The meteorological parameters supplied by the sounding software are shown in Table 2.2.

Table 2.2: Data obtained from soundings.

PARAMETER	UNITS
Time	S
Latitude	Degrees (5 decimal places)
Longitude	Degrees (5 decimal places)
Geopotential meter above ground level	m (no decimal places)
Temperature	°C
Dew point temperature	°C
Relative Humidity	%
Wind Speed	m/s
Wind Direction	Degrees true
Mixing Ratio	g/kg
Pressure	hPa

2.4   Pilot reports

Additional information in the form of observations from aircraft have often been used in large scale mountain wave projects e.g. in SWP, JSP and the Colorado Lee Wave Observational Project (Kuettner & Hertenstein 2002). More recent studies where aircraft observations were used includes: Shun *et al.* (2004) and T-REX, described by Doyle *et al.* (2009). For this project feedback from pilots was obtained for both field experiments. Pilots approaching Cape Town from the east were requested to report turbulence. This request was posted on an aviation internet forum. It was very difficult to get reports from pilots close to the study area. Only one report was received which served to show the special extent of mountain waves over the Western Cape at a specific point in time.

2.5   Calculations used for processing the data

This section describes the parameters used to determine features of mountain waves. Each subsection defines the parameter and briefly describes the use of the parameter in the study.

2.5.1 Potential temperature

Huschke (1959) defines potential temperature as the temperature which a parcel of dry air will have when it rises or sinks adiabatically to a level where the pressure is 1000hPa. He gives the formula for potential temperature as:

$$\theta = T\left(\frac{1000}{p}\right)^{R/c_p} \qquad (2.1)$$

Where T is the temperature in K, p is the pressure in hPa, R is the gas constant for dry air, and c_p is the specific heat of dry air at constant pressure. The values of the latter two constants are 287 $JK^{-1}kg^{-1}$ and 1004 $JK^{-1}kg^{-1}$ respectively (Holton 1992). In the calculation of potential temperature this exponent was used to six decimal places, i.e. 0.285856.

Doyle & Durran (2007), Hertenstein & Keuttner (2005) and Grubišić & Billings (2007) depict in their modelling of mountain waves, a potential temperature (θ) field following the curvature of mountain waves. Stromberg *et al*. (1989) refer to lines of equal θ as isopleths. These isopleths then give a graphical depiction of the shape of the mountain waves. θ values are used in the calculation of the Scorer parameter and Richarson number.

2.5.2 Scorer parameter

Chan & Tam (1996) define the Scorer parameter as

$$l^2 = \frac{\left(\frac{g}{\theta}\right)\left(\frac{\partial \theta}{\partial z}\right)}{U^2} - \left(\frac{1}{U}\right)\left(\frac{d^2 U}{dz^2}\right) \qquad (2.2)$$

where g is the gravitational acceleration of 9.81 ms^{-1}, θ is the potential temperature in K, U is the average horizontal wind speed perpendicular to the mountain barrier through a single layer depth and z is the height above sea level. Vertical intervals of 100 m were used and all averaging was performed accordingly. Chan & Tam (1996) mention that the second term in Equation 2.2 can be ignored since it is assumed to be much smaller than the first term. Barry (1981) indeed ignores the second term. Equation 2.2 then reduces to:

$$l^2 \approx \frac{\left(\frac{g}{\theta}\right)\left(\frac{\partial \theta}{\partial z}\right)}{U^2} \qquad (2.3)$$

Equation 2.3 was used throughout this study. Both these publications used km^{-2} as Scorer units and the data from this study had the same units for comparison.

According to Durran (2003) a necessary condition for the existence of trapped lee waves is that

$$Lower\ l^2 - Upper\ l^2 > \pi^2/4H^2 \qquad (2.4)$$

is satisfied, where *Lower l^2* and *Upper l^2* refer the average l^2 value for respectively a lower and adjacent upper layer of the atmosphere and H refers to the depth of the lower layer in km. Equation 2.4 is also implemented by Shun *et al*. (2004).

2.5.3   Wavelength

According to Huschke (1959) wavelength is the distance measured along the direction of propagation of the wave from the midpoint of one crest to the midpoint of the next crest (upstream or downstream). Numerically, Barry (1981) defines wavelength as

$$\lambda \approx \frac{2\pi}{l} \qquad (2.5),$$

where λ is the wavelength in km, and l is the Scorer parameter. From this equation it is clear that a decrease in stability will increase the wavelength, which explains why the wavelength increased during the day, since the stability decreases.   Barry also gives the position of the first lee wave as approximately 0.75λ to the lee of the mountain range.

Shun *et al.* (2004) uses peaks and troughs in the Scorer graph and then uses Equation 2.5 to calculate which wavelengths would be trapped by a particular peak in the Scorer graph. An estimation of wavelength using balloon ascent rates is implemented by Shutts *et al*. (1993) and is also used in this study for comparison. From the definition of wavelength, wave crests positions can be estimated from known wavelength. This enabled the construction of isopleths estimations in this study.

2.5.4 u-wind and v-wind

u-wind and v-wind are the W-E and N-S vector components of the wind. The sounding data (Table 2.2) calculated wind direction and wind speed at one second intervals.   Both the Richardson number and horizontal vorticity equations use the u-wind component, while the Richardson number uses the v-component as well. The D-Met wind direction thus had to be converted to u and v components. The equations used were:

$$u = (wind\ speed)(sin\alpha) \quad (2.6)$$

$$v = (wind\ speed)(-cos\alpha) \quad (2.7)$$

Where the 'wind speed' is the recorded speed from the D-met data and α is the wind direction in degrees converted to radians (Finney & Thomas 1994). For summit and upwind wind speeds, true direction and speeds were used and not the u- and v-wind components.

2.5.5   Converting GPS data to change in horizontal distance along the u-component

To convert difference in longitude to horizontal distance in and along an easterly direction, a difference of 0.00001° was converted to distance in m, by using an internet based calculator (Veness 2010) for different locations in relation to a line along the ridge at a bearing of 54.5° with respect to the N-S axis. This line was drawn through Els Peak and Matroosberg (see Figure 3.48) and represented the average orientation of the Hex River Mountains. Lee side distances were calculated for points east of this line; thus with respect to a north-south rotated axis. This coordinate system was used for all calculations, so that u and v coordinates could be directly used in calculations. Given the orientation of the Hex River Mountains a northeast-southwest rotated axis would have resulted in more ideal results for north westerly upwind conditions. Some of the upwind wind directions in the data were closer to westerly than north westerly, in which case the results in this study are not completely unreasonable.

2.5.6   Vertical velocity, Balloon ascent rate and Geopotential height

Vertical velocity was determined by using the method of Grubišić & Billings (2007) where the average ascent rate of the sounding is subtracted from the instantaneous balloon ascent rate. Ansmann, Fruntke & Engelmann (2010) term negative vertical velocity downdrafts and positive vertical velocity updrafts. From the D-Met data instantaneous balloon ascent rate is the vertical distance in geopotential meter that the balloon travelled in one second. Holton (1992) defines the scale of vertical velocity as cms[-1]. The fact that the D-Met software provided no decimals, resulted in a loss of accuracy. A recalculation of geopotential height was then performed using the calculated D-Met pressure values.

Pressure is used by Holton (1992) as a vertical coordinate. He states that geopotential(Φ) may be defined in terms of gravity, as:

$$d\Phi = gdz \qquad (2.8)$$

Geopotential height is then defined as

$$Z = \frac{\Phi(z)}{g} \qquad (2.9),$$

where g equals the global average for gravity at mean sea level. The height difference between two geopotential heights is then determined by:

$$Z_2 - Z_1 = R/g \int_{p1}^{p2} \frac{T}{p} \, dp$$

$$= RT/g \int_{p1}^{p2} dlnp \qquad (2.10)$$

$$= \left[RT ln \left(\frac{p1}{p2} \right) \right] / g \qquad (2.11)$$

Where R is the gas constant 287.05307 Jkg^{-1}K^{-1}, T is the average layer temperature in Kelvin, $p1$ and $p2$ is respectively the pressure in hPa at the bottom and top of a layer of air.

Mahoney (2008) uses virtual potential temperature in the place of temperature in Equation 2.11, which he defines as:

$$Tv(p, T, RH) = \frac{T}{\left\{ 1 - \left[\frac{RH(es)}{100.p} \right] [1 - \varepsilon a] \right\}} \qquad (2.12)$$

Where p is the pressure in mmHg, T the temperature in °C, RH is the relative humidity as a decimal fraction of 1, es the saturation vapour pressure for water vapour and εa the molecular weight ratio of wet and dry air, taken as 0.622. In order to calculate es , the Antoine equation of Reklaitis (1983) was used:

$$\log(es) = A - \left(\frac{B}{T+C} \right) \qquad (2.13)$$

where es is the pressure in mmHg, T is temperature in °C and A, B and C are unique values associated with each chemical compound, with values of   8.07131, 1730.63 and 233.426

respectively associated with water, which was taken from the DDBST data bank (2011). The final calculation of *es* was performed by taking the inverse logarithm of Equation 2.13. These values were substituted into Equation 2.13, which in turn, when substituted into Equation 2.11, yielded:

$$Z_2 - Z_1 = \left[R(Tv) ln \left(\frac{p1}{p2} \right) \right] / g \qquad (2.14)$$

Equation 2.14 produced values of geopotential meter to five decimal places, overcoming the problem of loss of accuracy. The ascent rate of the balloons was taken as the difference in geopotential height between consecutive seconds of each ascent, as used by McHugh *et al*. (2008). An average ascent rate for every 50 m of altitude was calculated and used in the plotting of ascent rate against horizontal and vertical distance. For vertical distance plots, the rounded geopotential metre data as supplied by the D-Met data was used.

2.5.7   Richardson number

The Richardson number (Ri) is calculated to ascertain whether conditions are favourable for the occurrence of turbulence in layers of the atmosphere. Chan (2008) states that when $Ri < 0.25$, the atmospheric conditions are favourable for the occurrence of turbulence. This guideline is also supported by Gossard & Hooke (1975), Holton (1992) and Huschke (1959).

Holton (1992) elaborates on this critical value of 0.25 by saying, that for a statically unstable boundary layer, Ri will have values less than 0, while for statically stable layer, Ri will be greater than 0. Based on observations, he suggested that turbulence in a stable layer will only occur if Ri is smaller than 0.25. The prerequisite of stability for the development of mountain waves (see section 1.4) then dictates that Ri values lie between 0 and 0.25.

Chan (2008) defines the Richardson number as:

$$Ri = \frac{\left(\frac{g}{\theta}\right)\left(\frac{\partial \theta}{\partial z}\right)}{\left[\left(\frac{\partial u}{\partial z}\right)^2 + \left(\frac{\partial v}{\partial z}\right)^2\right]} \qquad (2.15)$$

Where u is the east-west component of the wind and v the north-south component. It was found that over 100 m intervals $\left(\frac{\partial \theta}{\partial z}\right)$ often had negative values as a result of minor fluctuations in the θ field. A larger vertical interval of 300 m was then used to smooth the data. The Richardson number is unit-less.

2.5.8   Horizontal vorticity

Hertenstein & Keuttner (2005) used horizontal vorticity values to illustrate differences between type 1 and type 2 rotors. This they defined as

$$\eta = \left(\frac{\partial u}{\partial z}\right) - \left(\frac{\partial w}{\partial x}\right) \qquad (2.16),$$

where η is the y-component of the horizontal vorticity around a north-south axis at different levels above the Earth. The first term of the equation refers to the change in horizontal speed of the u-vector or west wind speed against z, the altitude difference, with layers of approximately 100 m in depth being considered.

The first term in Equation 2.16 was determined by identifying points in the ascent at approximately 100 m vertical intervals. The u component at the bottom of such a layer was subtracted from the u component at the top of the layer. This result was then divided by the depth of the layer (top altitude minus bottom altitude).

The w value in the second term represents vertical velocity. Although geopotential was recalculated using the methods mentioned in Section 2.5.6, the per-second changes in geopotential height which produced w, often oscillated between positive to negative values. Therefore two average values of w for each layer was determined, one for the lower approximate 50 m of the layer and an upper average for the upper 50 m. The lower layer value was then subtracted from the upper layer value and divided by ∂x, the horizontal (west-east) change in position, which was described in Section 2.5.5. At times rapid fluctuations in the two dimensional track of the balloon were observed. In such cases vertical layers of 100 m were too

large and the η data did reflect the changes in balloon position well. Over such areas along the balloon track, smaller vertical were used and more data points considered.

Hertenstein & Kuettner (2005) used η values to distinguish between type 1 and type 2 rotors. Type 1 rotors are associated with mainly positive η values while type 2 rotors show significantly more negative values. The positive η values in type 2 rotors can reach 0.07 s^{-1} in magnitude with negative η values reaching -0.04 s^{-1}.

2.5.9   International standard atmosphere (ISA)

For the synoptic scale weather analysis this study used standard atmospheric levels of 850, 700, 500 and 300 hPa. According to the American Meteorological Society (2011), these levels represent a hypothetical vertical distribution of pressure (and other variables) against height, where the height is geopotential height (Air Ministry Meteorological Office 1960). These levels are shown in Table 2.3.

Table 2.3: Standard atmospheric levels according to the ISA.

ALTITUDE ft	ALTITUDE m	LEVEL hPa
5000	1524	843
10000	3049	697
18000	5488	506
38000	11585	206

Source: Cavcar (2011)

2.5.10 Half-width of mountain

Chan & Tam (1996) and Huschke (1959) define half-width (a) as the distance between two points on either side of a ridge (curve), at which the height (intensity) is half of the maximum. The Hex River Mountain topography to the east of the Sanddrif River was used to determine the half width of the mountain. The 900 m contour on both sides of the mountain was used as a base with 2000 m taken as the average ridge height. This resulted in the use of the 1450 m contour on the upwind and lee side to determine the half width. The result was a half-width of 3.78 km.

According to Chan & Tam (1996) wavelengths near the half-width of a barrier are favourable for the development of lee waves.

Koch *et al*. (2006) related half-width to the Brunt-Vaisala frequency (N) which in turn Barry (1981) uses in another definition of the Scorer parameter:

$$l^2 = \frac{4\pi N^2}{U^2} \qquad (2.17).$$

Here U is the average horizontal wind speed perpendicular to the mountain for a layer of the atmosphere.

According to Koch *et al.*(2006) trapped lee waves are primarily formed when

$$a \ll U/N \qquad (2.18),$$

where a is the half-width. Substituting Equation 2.17 into 2.18 results in the condition

$$a \ll \frac{2\pi}{l} \qquad (2.19).$$

Equation 2.19 then serves as a further test for the development of trapped lee waves.

The following chapter features the field work of 22 July 2011. The synoptic weather, locations of the launch sites and meteorological parameters measured by each balloon is discussed using the formulas from the present chapter.

CHAPTER 3: FIELD WORK 22 JULY 2010

3.1   Surface conditions (NCEP reanalysis)

The mean sea level pressure for 06:00 and 18:00 GMT is shown in Figure 3.1. The position of the 06:00 GMT surface cold front is indicated as a dotted green line, while the 18:00 GMT cold front position is shown by a solid green line.   On the 18:00 GMT image the eastward advancement of the front is clearly shown. In using NCEP reanalysis data, geostrophic flow is assumed, that is, wind direction parallel to the geopotential height lines (Lankford 2000). This geostrophic assumption leads to north westerly winds over the study area at 06:00 GMT and backing to westerly by 18:00 GMT (green arrows).
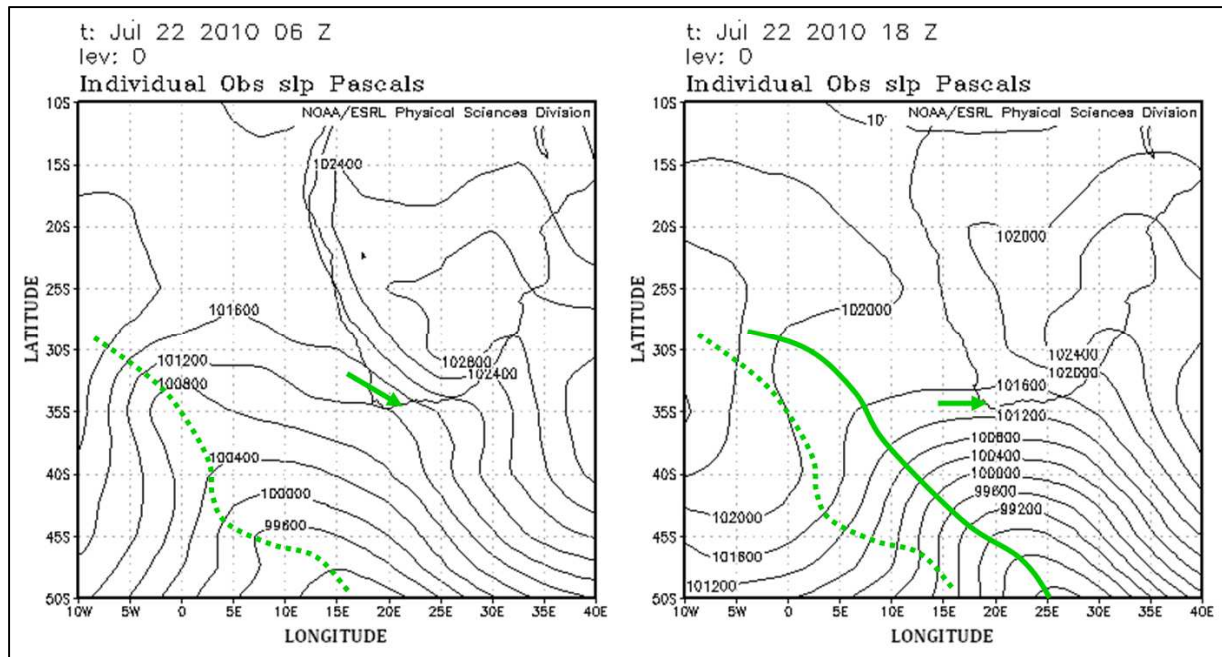
(Source: NCEP reanalysis 2010)

Figure 3.1: Sea level pressure for 06:00 GMT and 18:00 GMT on 22 July 2010.

3.2   Upper air conditions (NCEP reanalysis)

According to Cassano (2010) the 850, 700 and 500 hPa pressure levels roughly represent 5000, 10 000 and 18 000 ft on upper level weather maps. In Figure 3.2 the upper two images show the

850 and 500hPa geopotential height perturbations for 06:00 GMT, while the bottom two images show geopotential height perturbations at 18:00 GMT. Trough lines are shown as dotted lines for 06:00 GMT and solid lines for 18:00 GMT. The 18:00 GMT images show clearly that the trough lines had advanced eastwards at both atmospheric levels from the dotted line positions of 06:00 GMT. According to Highwood (2003) and Nielsen-Gammon (2010) wind direction is approximately parallel to geopotential height lines. This flow over the Hex River Valley was NW for the 850 hPa level (blue arrows) and for the 500 hPa level (red arrows) at 06:00 GMT. By 18:00 GMT (bottom of Figure 3.2) the 850 hPa wind direction had backed to W with the wind direction at 500 hPa still approximately NW.

According to Lim & Simmonds 2006 80% of mid-latitude cyclones which extend from mean sea level to above the 500 hPa level show a westward tilt with height until the surface low experiences its maximum depth (maturity). Holton (1992) states that the westwards tilt of trough lines with height is a necessary for the continued development of cyclonic waves. At the mature stage the trough lines are approximately in phase. The westwards tilt is indicated by an orange area on the 500 hPa charts in Figure 3.2. At 06:00 GMT this tilt is clear but disappears north of 42°S by 18:00 GMT. At the latitude of the study area the system had reached maturity between 06:00 and 18:00 and was no longer intensifying by 18:00.
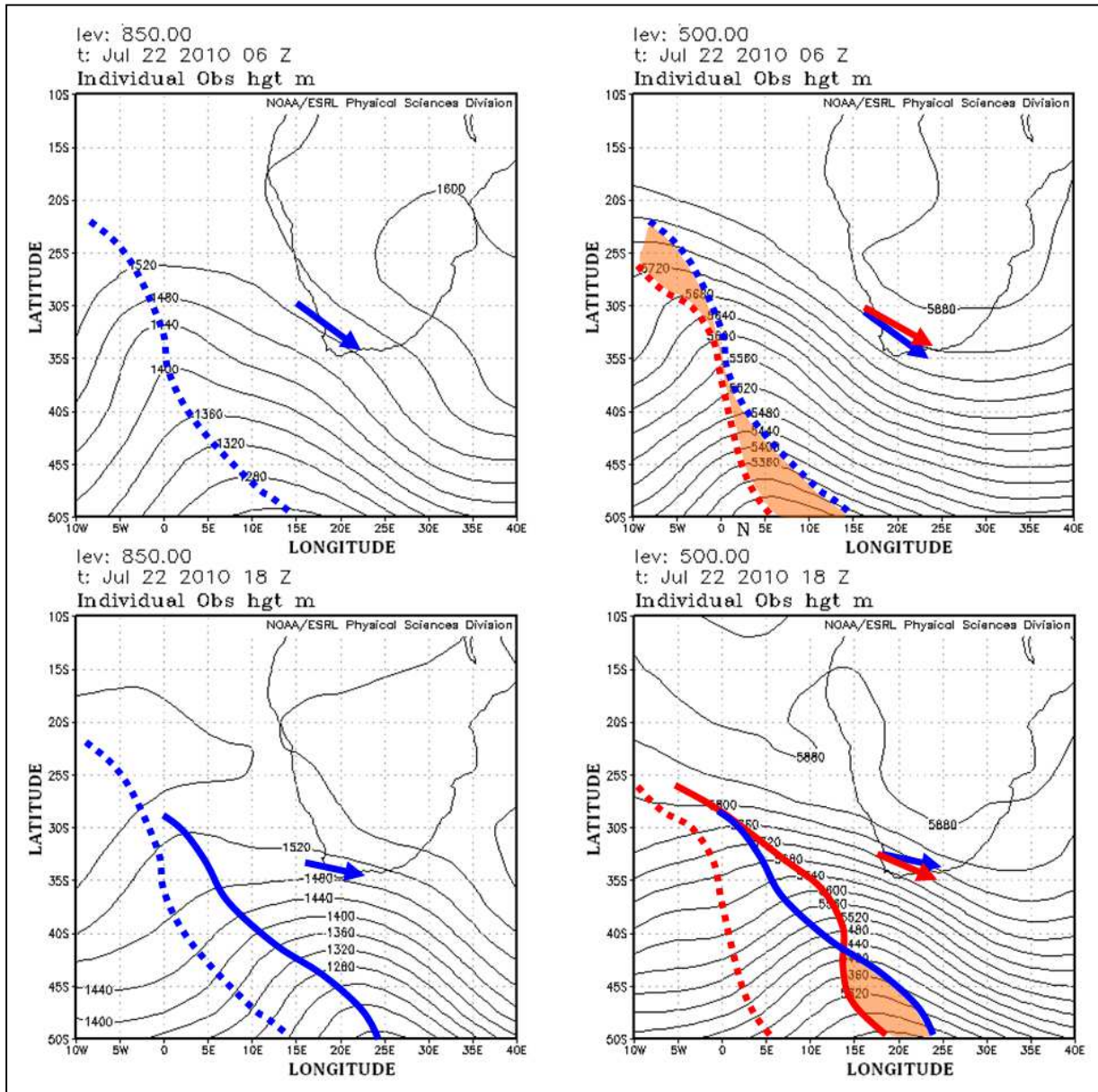
Source: NCEP reanalysis (2011)

Figure 3.2: 850 and 500 hPa geopotential height lines for 06:00 (top) and 18:00 GMT (bottom).

3.3   Upper air conditions (S1 sounding data)

The S1 sounding was conducted on the windward side of the Hex River Mountains on the morning of 22 July 2010 (See Section 3.5). The wind direction for S1 is shown in Figure 3.3. The yellow area shows wind direction which would be within 30° of perpendicular to the 54.5° orientation used for calculations (see Section 2.5.5), and according to Barry (1981) would be the preferred window of directions to create mountain waves. The wind directions at all heights up to almost 7000 m above MSL satisfy this requirement. Four altitudes near the 850, 700 and 500 hPa geopotential height lines of the NCEP reanalysis data as well as the summit altitude are marked along the wind speed graph. It shows that the summit wind exceeds 16 ms^{-1} and is thus higher than the requirement for a four kilometer high ridge (Barry 1981).
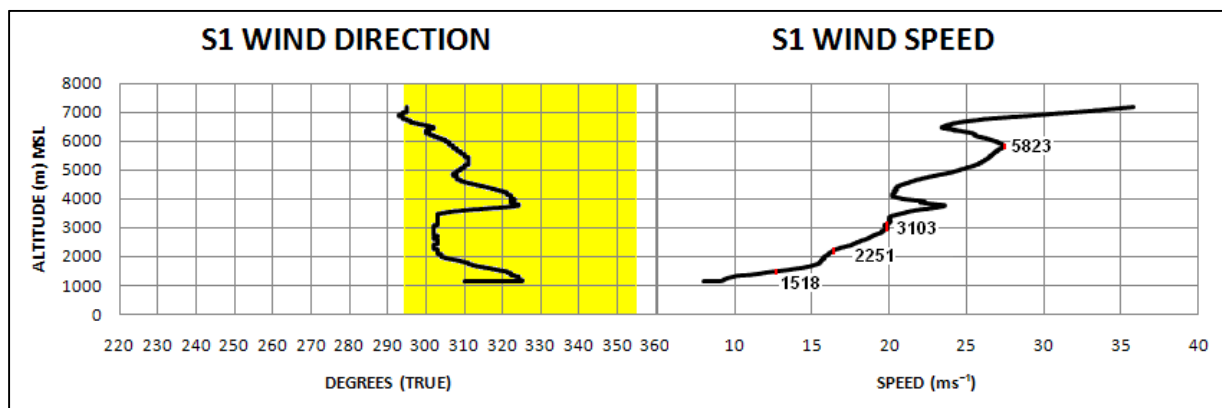
Figure 3.3: Wind direction and speed for S1.

3.4   Surface conditions (SAWS data)

With the computational orientation of the Hex River Mountains on a bearing around 54.5°, the optimal true wind direction range within 30° from perpendicular to the mountain range will be 295.5° - 355.5°. The South African Weather Service (SAWS) 15 minute averaged wind direction for three upwind stations (see Figure B.1, Appendix B) is shown in Figure 3.4 where the optimal wind direction range is indicated in yellow.

Wellington and Porterville are situated at respective elevations of 176 m and 122 m above MSL. From the Wellington and Porterville stations, on true bearings within the optimal direction range, there is very little rising terrain that can influence wind direction. In Figure 3.4 it is observed that between 12:00 and 16:00 GMT both these stations experienced mainly favourable (yellow area) winds. During this period the Wellington wind speeds ranging between 3 and 7 ms^{-1}, with an average of 4.7 ms^{-1}. The Porterville wind speed range was 1.5 - 5.1 ms^{-1} and average 3.1ms^{-1}. In spite of the stronger wind speed for Wellington during this period, its proximity to high mountains to its east created favourable conditions for wind channelling (Carrera, Gyakum & Lin 2009) with resultant N to NE wind directions.

In contrast (Ceres) Excelsior is situated at an elevation of 958 m MSL to the north of the study area, completely surrounded by mountains. Along the same bearings as mentioned before lies the Koue Bokkeveldberge which rise to elevations in excess of 1780 m. The data in Figure 3.4 shows a strong bias towards N to NE wind directions.
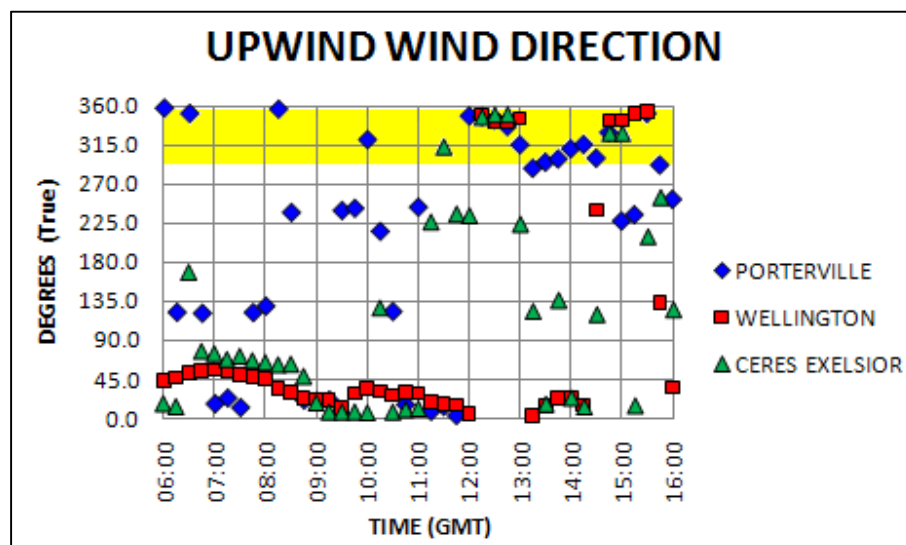
Figure 3.4: Upwind wind direction on 22 July 2010.

In Figure 3.5 the surface temperature graphs for the three upwind stations are shown. In addition to these stations Worcester data was also added in order to compare its surface temperatures with that of the upwind stations.   Worcester is situated just south west of the Hex River Valley in the lee of the Hex River Mountains at an elevation of 204 m MSL and does not represent conditions

upwind from the Hex River Mountains. Worcester showed a higher temperature than the upwind sites for the entire day. During the 12:00-13:00 GMT period the Worcester temperature of approximately 26.5°C was at least 1.5°C warmer than the upwind counterparts while the S2/S3 lee side balloon site near De Doorns reported a 28°C temperature at times during the same period. This may be the result of adiabatic warming on the lee of the Hex River Mountains (Wang & Chen 2002).
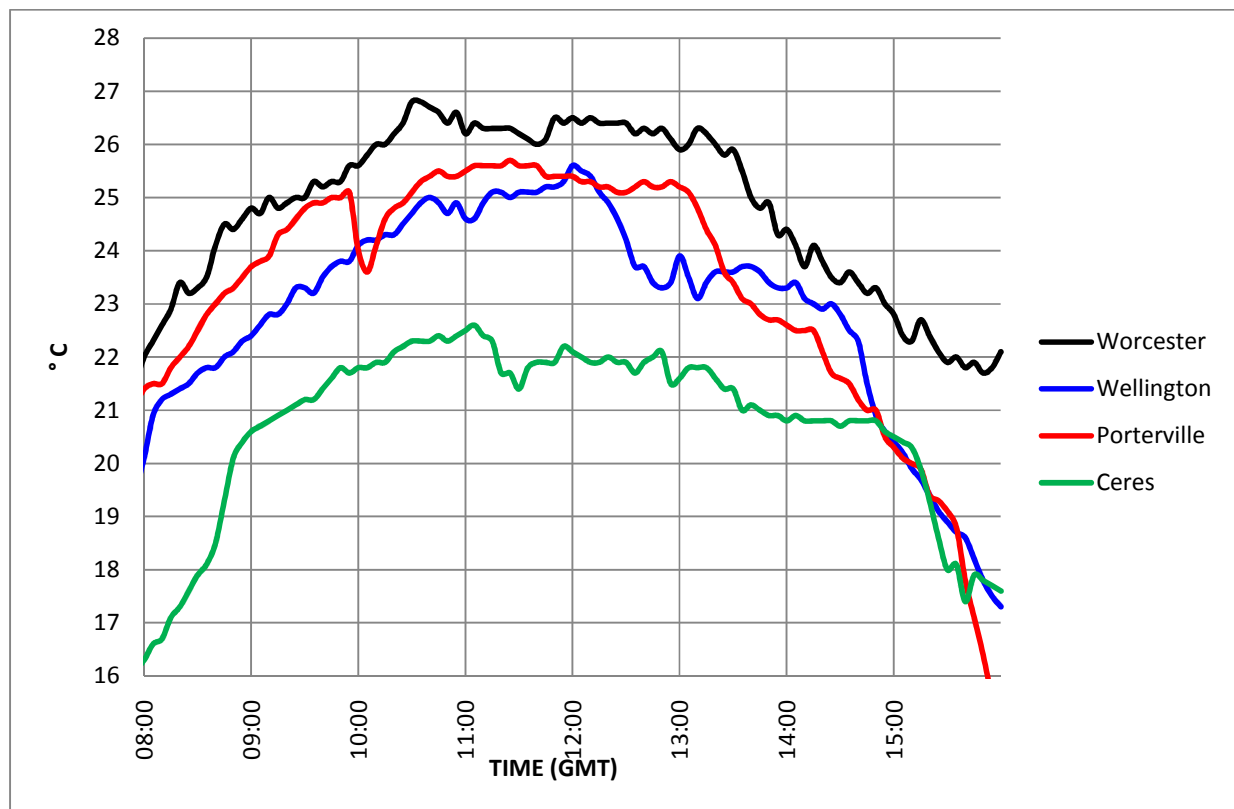
Figure 3.5: Upwind surface temperature on 22 July 2010.

3.5   Sounding locations and objectives

Over four days of experiments, 16 balloon soundings were performed. The soundings were numbered from S1 to S16. S1 through S4 were conducted on 22 July 2010. Figure 3.6 shows the positions of the launch sites as well as significant positions of the S1 balloon (blue squares) on this date.

Source: Chief Directorate Surveys and Mapping (2006)

Figure 3.6: The location of launch sites for S1, S2, S3 and S4

The purpose of S1 was to attain atmospheric data representing the upwind side of the Hex River Mountains. From this sounding the Scorer parameter of this data could be determined as well as the wavelength for mountain lee waves. The purpose of S2 and S3 were to do consecutive ascents from the same lee side site for comparison in as short a period as possible. S4 was performed as close as possible to the mountain in the hope that the sounding will be able to enter a mountain wave at an early stage and record as much data from the wave as possible. The sounding data is tabulated in Table 3.1.

Table 3.1: Launch site data for S1-S4

SOUNDING	LATITUDE	LONGITUDE	ALTITUDE	TIME OF RELEASE
	Degrees	Degrees	m MSL	GMT
S1	-33.33119	19.61134	1167	09:50
S2	-33.42417	19.68477	608	12:11
S3	-33.42417	19.68477	608	13:12
S4	-33.41224	19.69926	688	14:53

3.6 Sounding 1 (S1)

3.6.1 S1 Profile

Figure 3.7 shows the two dimensional path of distance against altitude as plotted in an easterly direction from the launch site. The most prominent feature of this plot (henceforth referred to as the profile) is the flattening in the curve observed around the 7 and 14 km marks east of the launch site.
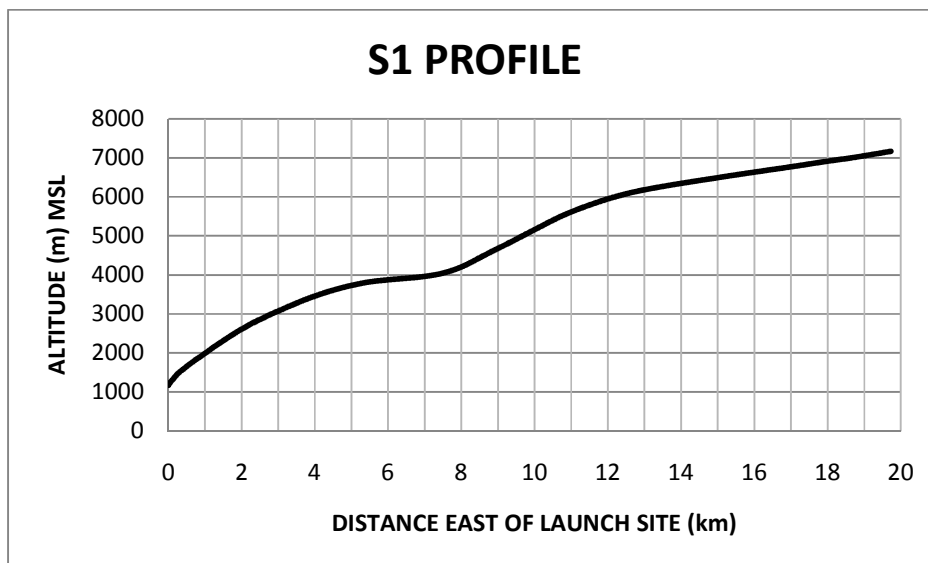
Figure 3.7: The distance east of the S1 launch site

These 7 and 14 km marks are indicated by 'S1-F' in Figure 3.6. 'S1-R' shows the position on the map where S1 passed over the ridge. Hence the flattening in the profile curve occurred to the lee of the Hex River Mountains (see also Appendix B, Figure B2 and Section 3.10).

3.6.2   S1 Potential temperature (θ)

Stability can be classified in terms of the change in θ with respect to altitude (Holton 1992; Stull 1991). This classification is summarized in Table 3.2. Several publications use potential temperature isopleths to indicate the position of mountain waves in the lee of barriers (Brinkman 1974; Durran 1986; Sheridan & Vosper 2006; Vosper 2004). These papers make no mention of the use of equivalent potential temperature. For this study potential temperature was used.

Table 3.2: Classification of stability

CHANGE IN θ WITH HEIGHT	STATIC STABILITY
dθ/dz > 0	Statically stable
dθ/dz = 0	Statically neutral
dθ/dz < 0	Statically unstable

Sources: Holton (1992) and Stull (1991)

Figure 3.8 shows the potential temperature (θ) for S1. The initial low level drop in θ is to be ignored as a computational spike which was observed in all sounding data. Overall the graph indicates an increase in θ with altitude, but at varying rates. It shows an increase in potential temperature from the surface to 2350 m, indicative of a stable atmosphere. Above this level the stability was neutral up to the 3600 m level. Between 3600 and 4000 m a 13 K increase in θ is observed, indicating a large increase in stability. The stable atmosphere continued above this level increasing at a slower rate. Thus above 3600 m the stability increased, satisfying the necessary condition of stable air at levels where the lee airflow will be disturbed by the mountain (see Section 1.4).
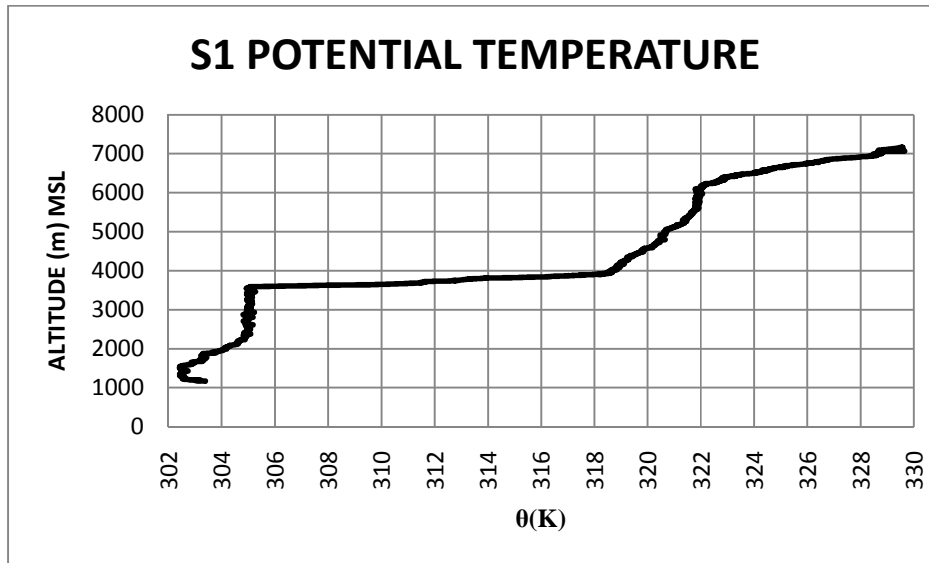
Figure 3.8: The potential temperature of S1.

3.6.3   S1 Scorer parameter

The Scorer parameter data for S1 is shown in Figure 3.9. The D-Met data shows that the balloon passed over the Hex River Mountains at an approximate altitude of 3800 m. Above this altitude the balloon was no longer upwind from the mountain and the winds used for the calculation of the Scorer Parameter are taken from areas above the lee side of the mountain. With no other data to use as reference, the assumption was made that at these altitudes the lee and upwind atmospheric conditions were approximately the same. A drop in l^2 with increased height up to 3500 m is observed. As stated by Barry (1981) and Lindsay (1962), such a drop is necessary for the development of trapped lee waves.

The S1 Scorer parameter values compare well with that found in literature. Barry (1981) places the typical range of Scorer values between 0.05 and 1.0 km^{-2}. In Figure 3.9 the majority of positive values fall within this range. The spike of 3.6 km^{-2} at the 3700 m level seem extreme at first glance. Lindsay (1962) describes Scorer profiles with values between 3 and 4 km^{-2}, while more recently Chan & Tam (1996) illustrated profiles with values exceeding 10 km^{-2}. Negative values in the Scorer parameter also fall outside of the 0.05-1.0 km^{-2} range. These negative values are the result of a decrease in potential temperature over the vertical intervals chosen, resulting in

negative $\partial\theta/\partial z$ values, which forced Equation 2.3 to become negative. Chan & Tam (1996) also published Scorer profiles with negative values.

Lindsay (1962) indicates that the altitude where local maximums occur in the Scorer graph is a good estimate for the altitude of maximum amplitude of the trapped lee wave. He was able to show how visible wave clouds were found near these maxima. The S1 data could thus indicate the existence of possible trapped lee waves below the Scorer maximum at 3700 m. This increase in l^2 corresponds to the large increase in potential temperature and thus stability as was shown in Figure 3.8.
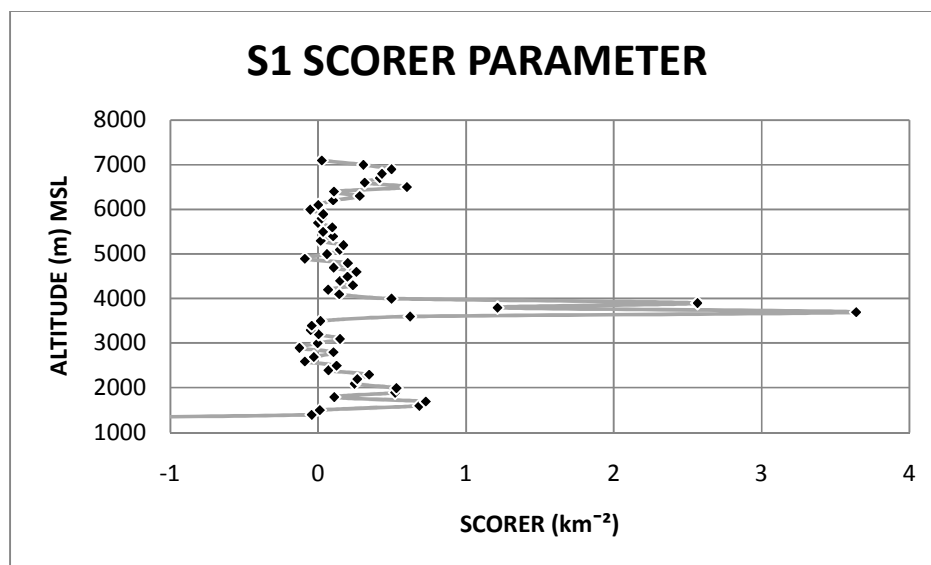
Figure 3.9: S1 Scorer parameter.

To more vigorously test for the existence of trapped lee waves, Equation 2.4 was used. The average layer Scorer value in km^{-2} is indicated for the lower red zone and upper blue zone in Figure 3.10. These values and the depth of the lower (red) zone can be substituted into Equation 2.4 resulting in $0.34677 > 0.27416$, thus satisfying the necessary condition for the development of trapped lee waves (Durran 2003). Here the lower layer H, indicated in red is 3 km deep and has a layer average l^2 value of 0.41572 and a l^2 value of 0.06895 for an upper layer (blue). This result seems to indicate that trapped lee waves could be found up to 4600 m above MSL at the top of the red layer as opposed to the 3700 m level as estimated by Lindsay (1962).
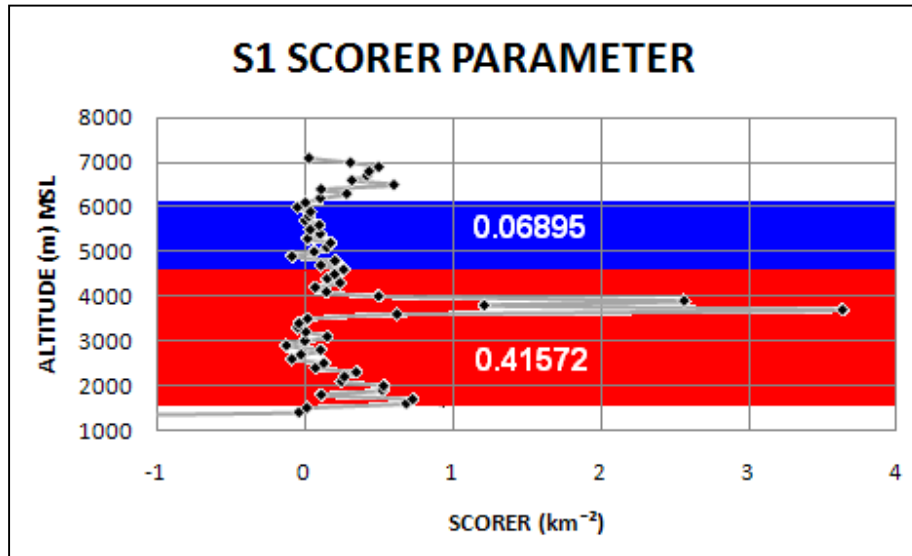
Figure 3.10: S1 data used in test for wave trapping.

A further confirmation of trapped lee waves is found by substituting the average Scorer value below 4000 m above MSL into Equation 2.19. This resulted in $a = 3.78 \ll 9.405$ which according to Koch *et al.* (2006) means that trapped lee waves are likely to be formed. The results of Equation 2.19 support the estimate of Linsday (1962). Equation 2.4 and its application in Figure 3.10 thus seem to lead to inaccurate results.

3.6.4   Lee wavelength

From the comment of Lindsay (1962) in Section 3.6.3, trapped lee waves can be expected under the red and blue peaks indicated in Figure 3.11. To test which wavelengths would be trapped, the example of Shun *et al*. (2004) was followed (see also Section 2.5.3). The values of l were determined by taking the square root of the values at a, b, c and d in Figure 3.11. These values were then substituted into Equation 2.5. The result was that for the red area all wavelengths between 3.3 and 24.3 km could be trapped within the altitude range of 3700-4200 m. Likewise wavelengths between 8.1 and 40.5 km would be trapped in an altitude range of 6500-7100 m (blue area).
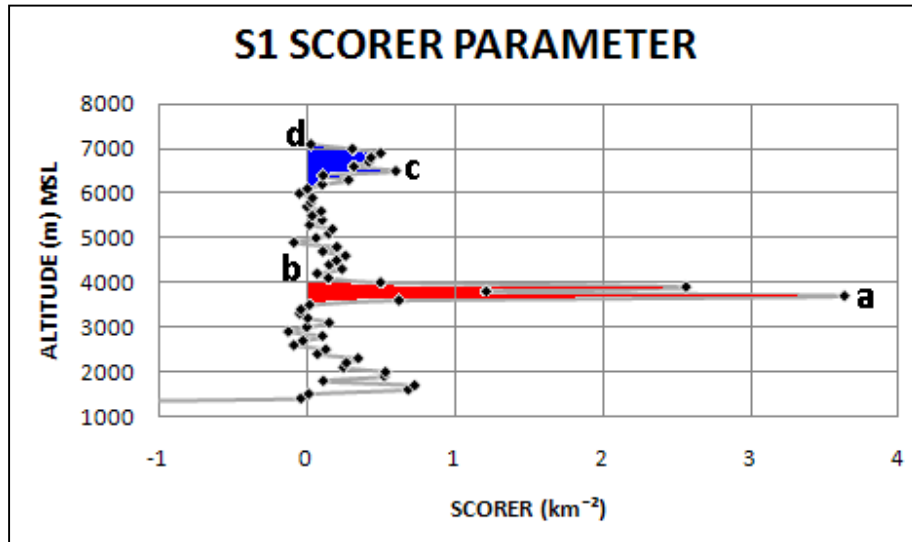
Figure 3.11: S1 Scorer parameter areas used to determine wavelengths for trapping.

From the upwind potential temperature graph and Scorer parameter analysis, it seems very likely that trapped lee waves could form on 22 July 2010 over the study area.

3.7   Sounding 2 (S2)

S2 and S3 were launched in the De Doorns district from a site marked as 'S2/S3' in Figure 3.6. These two soundings were conducted 61 minutes apart in order to compare the short term variations in lee side atmospheric conditions. The S1 data was obtained more than two hours prior to the start of S2 and the assumption had to be made that the atmospheric conditions upwind of the mountain would not have changed much during that period. The practice of using radiosonde data that is several hours old is very common. Shun *et al.* (2004) compares flight data and LIDAR Doppler data with balloon ascent data which was obtained three hours earlier. The assumption was also made that the synoptic scale weather pattern during the day changed rather slowly.

3.7.1   S2 Profile

In Figure 3.12 the ascent profile shows a rapid gain in altitude and significant horizontal fluctuation below 2500 m above MSL. The slope of the curve decreases in two places and is indicated by green areas along the curve centred about the 7 and 13km marks.
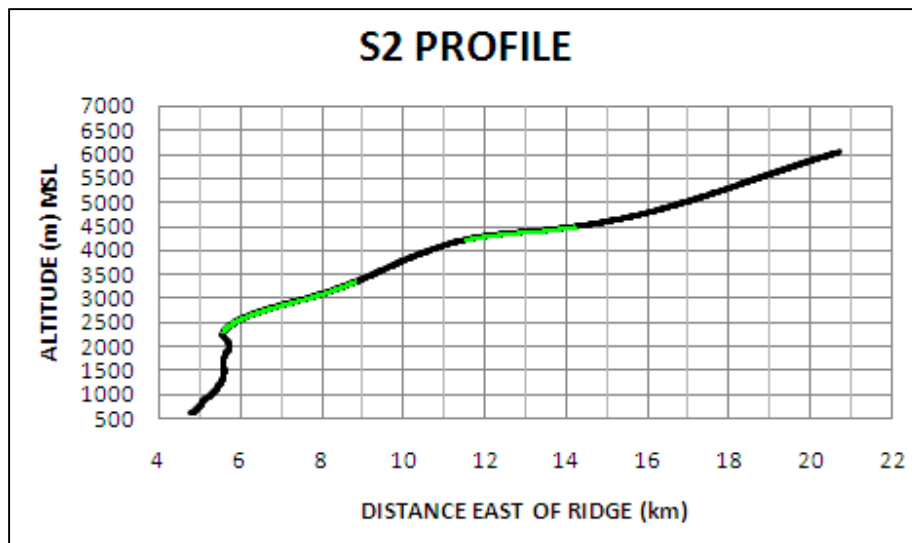
Figure 3.12: The S2 profile.

The low level fluctuation is shown in greater detail in Figure 3.13. It shows two altitude levels where the balloon experienced reversed flow, that is, flow towards the mountain (upwind): 1500 - 1650 m and 2000 - 2250 m. According to Grubišić & Billings (2007) this indicates rotor development.   They measured reversed flow of a magnitude of 3 ms^{-1}. The highest reversed flow wind speed recorded by S2 has an easterly wind component of 1.21987 ms^{-1} at 2157 m above MSL. The true wind direction vector was 5.9 ms^{-1} on a bearing of 12°.
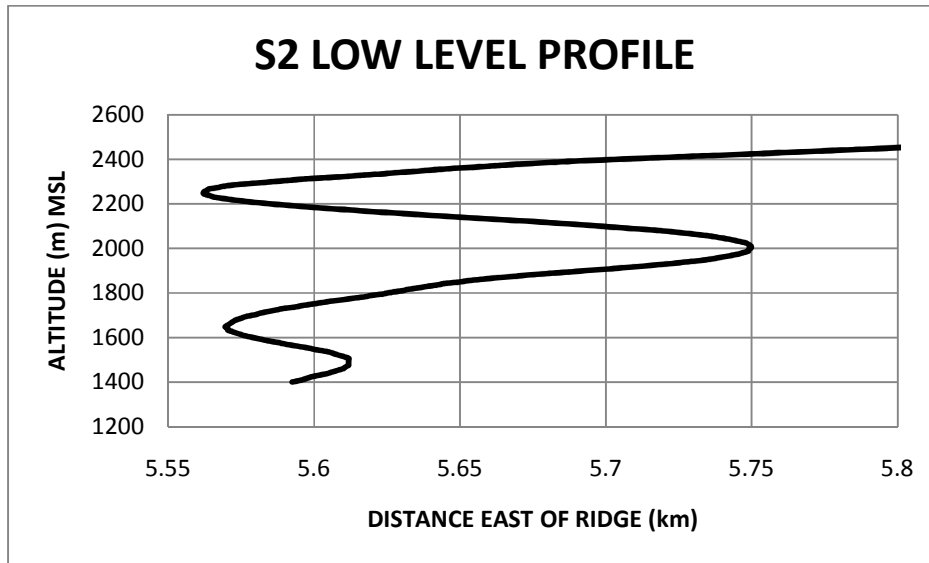
Figure 3.13: The S2 low level profile indicating reversed flow. Note: Axes are not to scale.

The fact that there are two layers where reversed flow took place is suggestive of possible sub-rotor development according to Doyle & Durran (2007). The horizontal length scales of these flows were approximately 50 m for the lower reversed flow and 190 m for the upper reversed flow. These scales represent only those parts of rotors through which the balloon passed.   The lower reversed flow was associated with a maximum wind speed of 4.7 ms^{-1} with the upper reversed flow reaching 7.3 ms^{-1}.

Through model data Hertenstein & Keuttner (2005) found that reversed flows occurred near the surface and significantly lower than the ridge height (4000 m) in the case of type 1 rotors. In the case of the type 2 rotor which Hertenstein & Keuttner mentions, a down-slope wind undercut the rotor area and elevated it. The bottom of the rotor area which they observed was situated near the summit level while the top reached nearly 2000 m above ridge height. This was a significant mountain wave event with the down-slope winds reaching 43 ms^{-1} and 53 ms^{-1} for the type 1 and type 2 rotor respectively. The horizontal extent of the reversed flow measured approximately 8 km for the type 1 and 25 km for the type 2 rotors. Considering the data at hand S2 could have experienced a type 1 rotor. Farmers in the Hex River Valley also indicated that strong damaging down-slope winds do not seem to be a feature of the weather in the valley (Malan 2010, pers com and Wium 2010, pers com).

3.7.2   S2 Richardson number (Ri)

The Richardson numbers for thirteen 300m vertical intervals of S2 are plotted in Figure 3.14. The value for each level is plotted against the altitude at the top of each layer. 85% of the values were positive, indicating that the atmosphere through these layers was stable on the lee side of the Hex River Mountains (Holton 1992). Six of the positive values were less than or equal to 0.25, which means that within these layers turbulence could have occurred. Chan (2008), Gossard & Hooke (1975), Holton (1992) and Huschke (1959) all mention this critical value as the maximum positive Ri value where turbulence can occur.   Of these six, four were found in the layer between 1200m and 2700m. The negative value within this layer (-0.019) was small enough to keep the layer average in the (0; 0.25] interval.
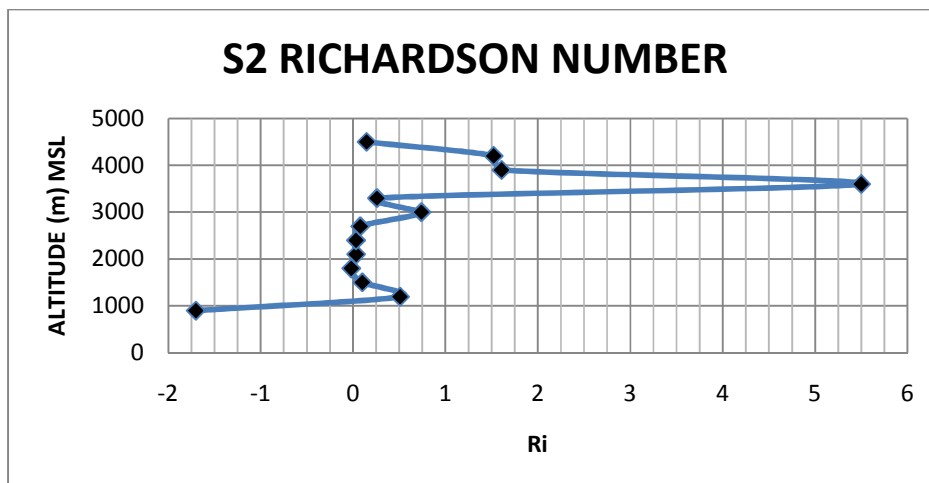
Figure 3.14: S2 Richardson number.

3.7.3   S2 Horizontal vorticity (η)

Doyle & Durran (2001) studied rotors and sub-rotors using model simulations of the y-component of horizontal vorticity (η). This value describes the rotation around a north-south axis (y-axis) parallel to the Earth's surface. Positive values describe a rotation clockwise about the y-axis. They found that within rotors underneath trapped lee waves positive vorticity

dominated and that reversed flow in some cases reached 17 ms^{-1} (Appendix B, Figure B.3). Small areas of zero horizontal vorticity are situated within the rotors, with no indication as to whether these values may actually be negative.

Hertenstein & Kuettner (2005) compared type 1 and type 2 rotors. In their simulations they used the Regional Atmospheric Modeling System (RAMS), with simulated terrain based on the Sierra Nevada Mountains and meteorological parameters based on the SWP observations. They found that the type 1 rotor mainly consisted of positive η values with negative η values associated with wave troughs and small areas within the rotor.

Figure 3.15 shows the η values for S2. Some positive η values (red areas) are observed below 2500 m above MSL which is to be expected when considering the observation of Doyle & Durran (2001) that η is predominantly positive. Two areas of negative η values (light blue and dark blue) are observed below 2100 m above MSL. Reversed flow seems to be linked to these negative η values, rather than positive values. With rotor flow below the wave being typically clockwise (thus positive η values), these negative η values do not make much sense. However Doyle & Durran (2007) show that small areas of negative η can be detected in type 1 rotors as well as in the troughs of the lee waves above them (Appendix B, Figure B.4). Hertenstein & Kuettner (2005) also mention that small areas of negative η can be found in type 1 rotors. The green negative η value is associated with a drop in the profile gradient may be indicative of a trough area in the overlying mountain wave area (Hertenstein & Kuettner 2005). Doyle & Durran 2007 also illustrates this in Appendix B, Figure B.4. The large positive η values just above 2500 m (orange) compare well with the statement of predominantly positive η in rotors made by Doyle & Durran (2001).
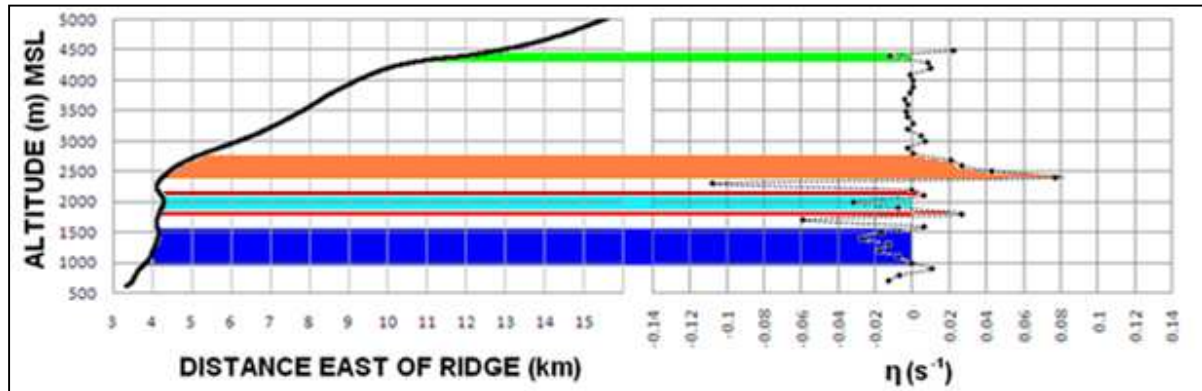
Figure 3.15: Comparison between S2 profile (left) and y-component horizontal vorticity.

3.7.4   S2 Balloon ascent rate

In Figure 3.16 the reversed flow is related to ascent rate. Yellow relates the ascent rate and profile of the lower reversed flow, red that for the upper reversed flow while blue compares non-reversed flow. During the lower reversed flow an increase in ascent rate of 0.5 ms^{-1} was recorded over a 50 m horizontal distance. The same phenomenon is observed for the upper reversed flow, which experienced a 1.6 ms^{-1} increase in ascent rate, which occurred over a 110 m horizontal distance.
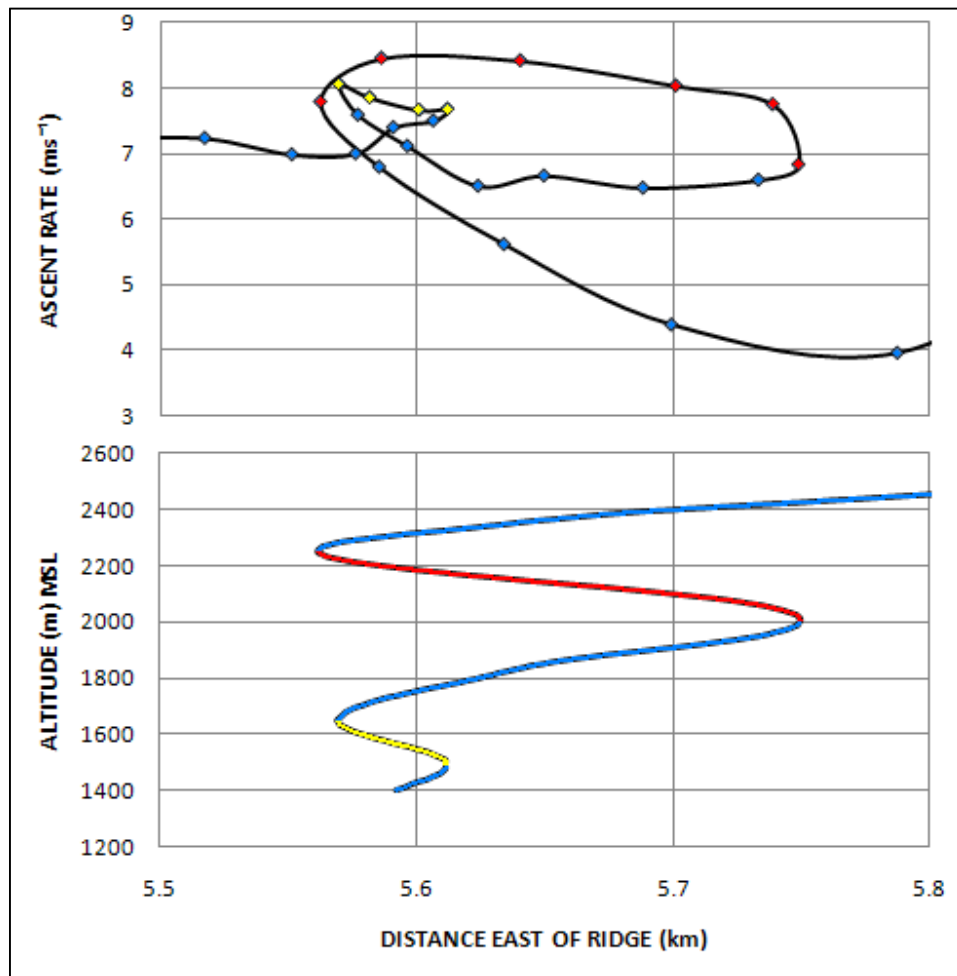
Figure 3.16: S2 ascent rate associated with reversed flow regions.

Figure 3.17 shows the ascent rate for 50 m vertical intervals for the entire sounding. From the 6 km mark, there are three peaks and two troughs in the ascent rate. According to Shutts, Healy & Mobbs (1994) the distance between the second and third peak, 10.0 km (19.7 – 9.7 km), estimates the wavelength of the mountain wave within an accuracy of 2 km. Then applying the theory of Barry (1981) the primary wave crest can be estimated to be at 0.75λ or approximately 7.5 km from the ridge along a vector perpendicular to the ridge line. This translates to 10.5 km east of the ridge line.

According to Mobbs *et al*. (2005) peaks in the ascent rate graph of their Falklands study were associated with areas of maximum updraft. The highest peak observed in Figure 3.17 is situated

between five and six kilometers east of the ridge. This peak is associated with a 4.5 ms^{-1} fluctuation in ascent between five and six km east of the ridge. Mobbs *et al*. (2005) found a fluctuation in ascent rate of approximately 7 ms^{-1} which they suggested may be the result of a hydraulic jump, thus indicative of type 2 rotors. The 4.5 ms^{-1} fluctuation in the S2 data is observed below the height of Matroosberg, the highest summit in the Hex River Mountains (see Figure 3.12). It will be shown in the following section that this fact implies that the S2 fluctuation is indicative of a type 1 rotor.
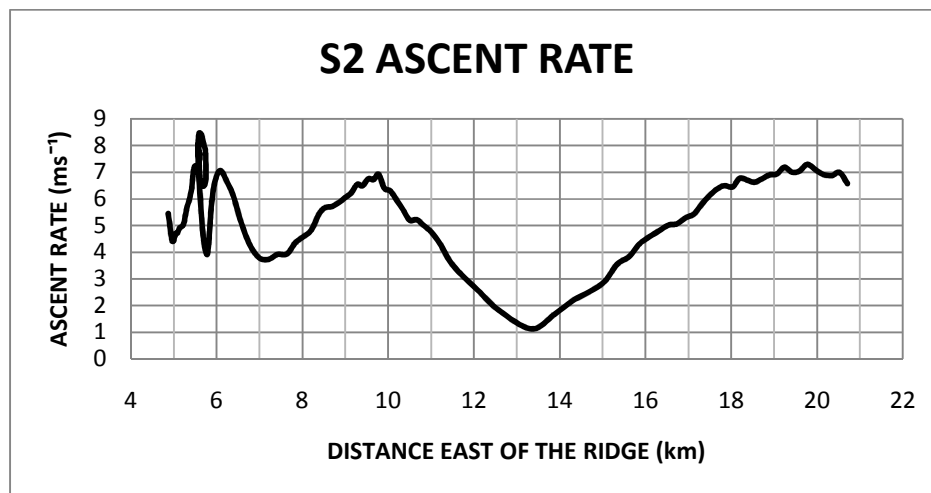
Figure 3.17: S2 ascent rate.

3.7.5   S2 Vertical velocity

Lalas & Einaudi (1980) proved statistically that sharp increases in ascent rate, of between 1.1 and 1.4 ms^{-1}, corresponded well with maxima of the wave vertical velocity. From statistical analysis they concluded that the wave itself was responsible for the fluctuations in balloon ascent rate. Subsequently Grubišić & Billings (2007) subtracted the average ascent rate of a sounding from the instantaneous ascent rate to arrive at instantaneous vertical velocity of the atmosphere along the two dimensional track of the balloon.

The average ascent rate of 5.1 ms^{-1} can be subtracted from the S2 ascent rate data. The vertical velocity data for the reversed flow regions is redrawn in Figure 3.18.   For the lower reversed flow region (yellow dots) there was a 0.48 ms^{-1} increase in updraft speed over 42 m horizontally

to a local maximum of 2.96 ms^{-1}. For the upper reversed flow (red dots) a 1.62 ms^{-1} increase in updraft speed to a local maximum of 3.35 ms^{-1} occurred over a 161 m horizontal distance. Within the rotors themselves the increases in updraft speed occurs gradually. However, if an aircraft with low wing loading is to enter the rotor zone from outside and is suddenly subjected to the updraft speed of 3 ms^{-1} it could experience moderate turbulence (Uys 2011, pers com).
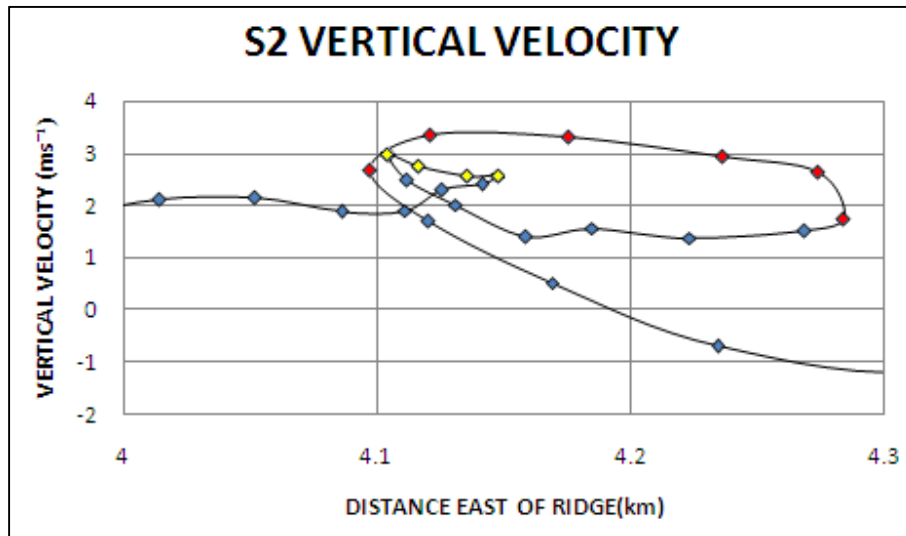
Figure 3.18: S2 vertical velocity during reversed flow.

Figure 3.19 shows the vertical velocity graph calculated for the entire S2 sounding. The high variability in the vertical velocity near the 5.5 km mark is associated with the reversed flow at low levels which was seen in Figures 3.16 and 3.18. Downdrafts are shown as green areas of negative vertical velocity and are associated with slight flattening in the profile curve, which are also shown in green. Positive vertical velocity (updraft) is associated with areas where the profile curve becomes steeper and local maxima in updrafts occur near the middle points of such steeper areas in the profile curve. With S2 negative vertical velocity did not result in drops in altitude in the profile curve. Downdraft maxima are associated with the approximate midpoints of the green areas of the profile curve. These areas were identified in Figure 3.12 as areas where the profile curve slope decreased.

For much larger mountains (4000 m summits) Hertenstein & Kuettner (2005) determined rotor updrafts speeds of 11 ms^{-1} associated with type 1 rotors and type 2 rotors. The difference was

found in the vertical distance from zero vertical velocity to the updraft maximum. For type 1 rotors this vertical distance was in the order of 4 km, confined to an area below the summit level while for type 2 rotors it was 2 km but extending to levels above the summit. As a constant value (5.1 ms^{-1}) is subtracted from the ascent rate data to yield the vertical velocity graph, the fluctuation in ascent rate (between five and six kilometers east of the ridge) which was observed in Figure 3.17, leads to a corresponding fluctuation in the vertical velocity graph. Figure 3.19 shows that the fluctuation in vertical velocity (and ascent rate) occurred below the height of the highest summit in the Hex River Mountains. It can thus be concluded that the fluctuation area was associated with a type 1 rotor (Hertenstein & Keuttner 2005).
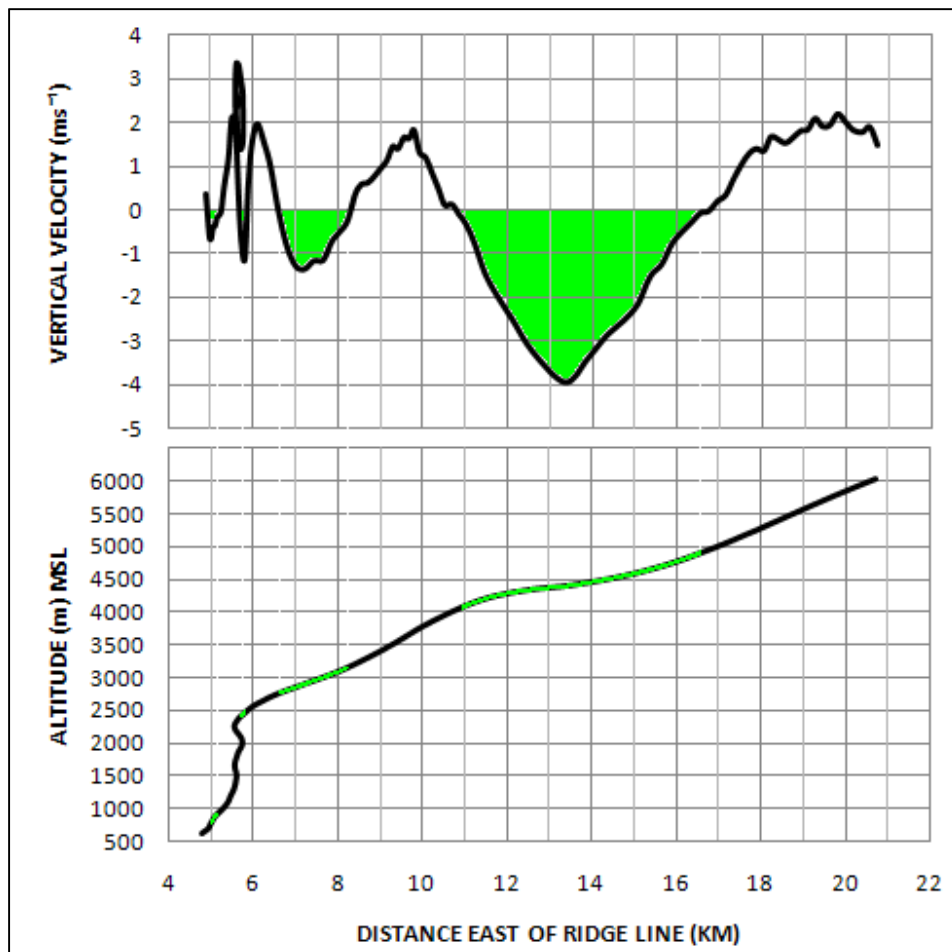
Figure 3.19: S2 Vertical velocity.

From Figure 1.1 it is expected that updrafts some distance away from the mountain are associated with parts of the leading edges of waves (blue arrows), while the downdraft areas will be situated on the trailing edges of waves (red arrows). The positions of the up- and downdrafts in relation to crests and troughs in the mountain wave will be investigated by estimating the isopleths of S2.

3.7.6   S2 Potential temperature (θ) and isopleth estimation

Doyle & Durran (2007) used model data to simulate low level rotor and sub-rotor development in the lee of terrain. Figure 3.20 shows their results for the strongest developed rotor and sub-rotor conditions in their study. The two lines represent two sets of data which they compared. It shows a three zone atmosphere with a neutrally stable zone near the surface up to 300 m, an unstable zone from 300 m to 600 m associated with a drop of 0.7 K and an upper zone above 600 m with an increase in θ in the upper zone.
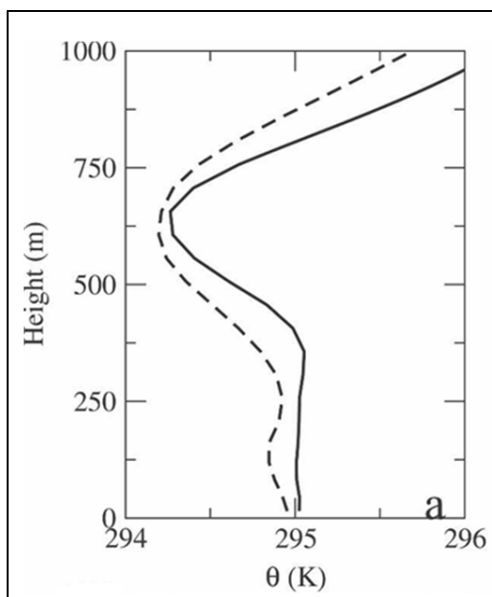
Source: Doyle & Durran (2007:4217)

Figure 3.20: Stability defined using potential temperature.

The S2 potential temperature (θ) graph for the entire sounding is shown in Figure 3.21. It does not show clear areas of instability as was observed in Figure 3.20. However a rather neutrally

stable atmosphere from the surface to 2400 m is observed, followed by a small 1.0 K increase from 2400 to 2600 m. Above the 2600 m level the atmosphere remains neutral up to 3700 m, followed by a large 18 K increase and stable atmosphere for the remainder of the sounding. When viewing the θ graph of the entire sounding, there is very little resemblance to the graph of Doyle & Durran (2007). For this reason a smaller section of the sounding data was considered at low level, where rotor turbulence was most likely to occur.
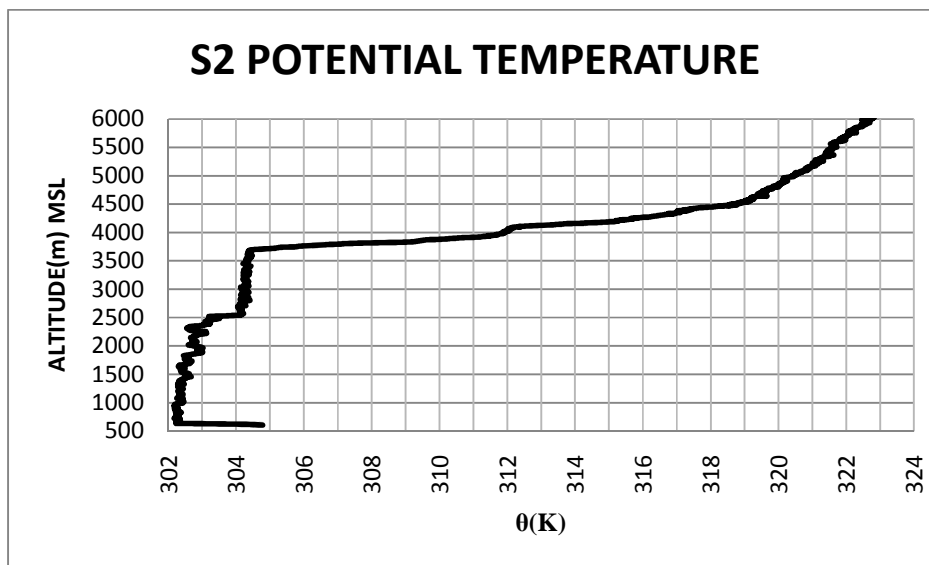
Figure 3.21: S2 Potential temperature

In Figure 3.22 θ below 2500 m above MSL is reproduced. Between 1900 and 2000 m a 0.4 K drop in θ is observed (blue line), while between 2200 and 2300 m a 0.6 K drop is observed (green line). Rather than the constant potential temperature below 300 m in Figure 3.20, the S2 data was characterised by two clusters ('cluster 1' and 'cluster 2' in Figure 3.22) of θ with negligible variability (approximately 0.1 K) below 1400 m. The low level θ graph thus resembles the graph of Figure 3.20 and shows that rotors and sub-rotors were possible for the S2 case.
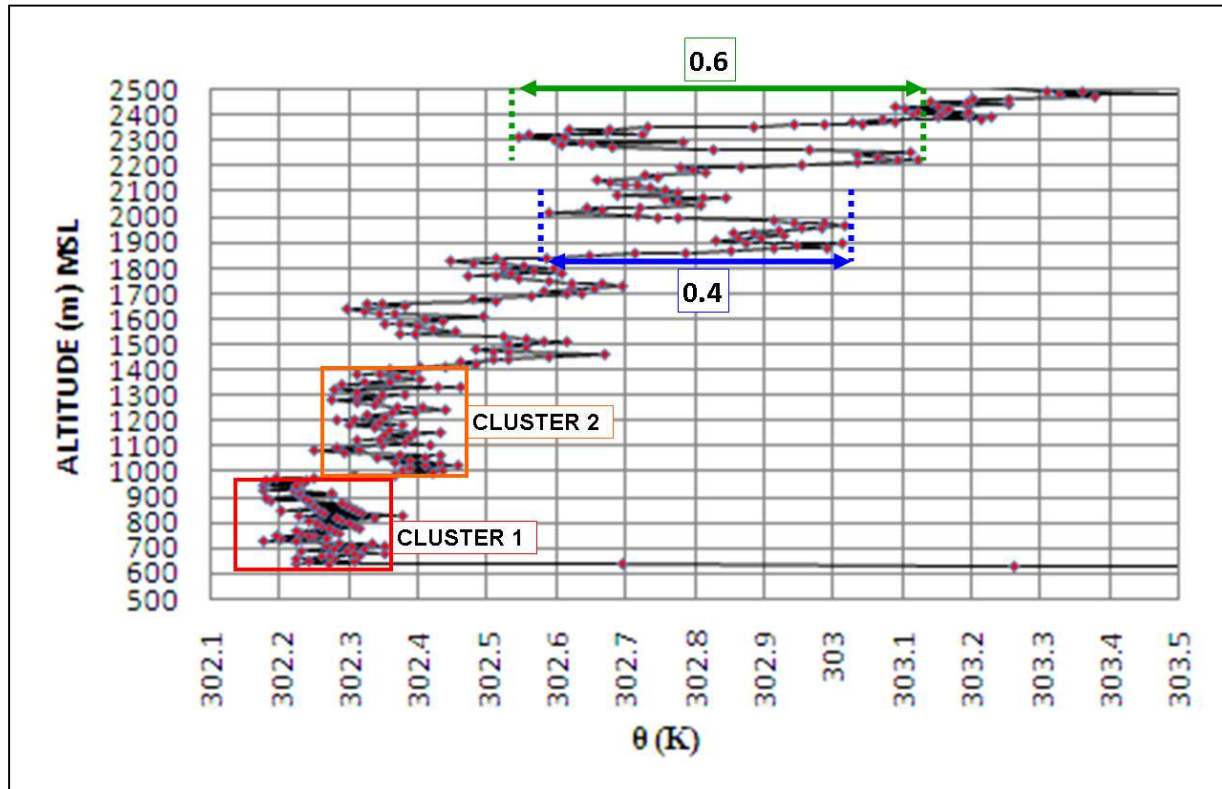
Figure 3.22: S2 stability defined using potential temperature.

Likely positions of isopleths for S2 are shown in Figure 3.23. In this study the isopleths estimation attempts to visualize the shape of lee waves as along an axis directed from the west to the east. This estimation is based on the points where potential temperature values coincided with the profile curve (black curve). Comments in red indicate the use of non-S2 data and theory to aid with the plotting of the isopleths. An assumption is made that the S2 320 K isopleth may lie very close to its S1 counterpart. In addition to this, the theory of Shutts, Healy & Mobbs (1994) using ascent rate peaks to estimate wavelength, was used to estimate the position of the secondary wave crest (red dashed lines). The first wave crest occurs near the 10.7 km mark where a downdraft is shown to commence according to Figure 3.19, which is also the point where the 308 K isopleth drops below the profile curve. A second crest can be estimated at the 20.7 km mark (Shutts, Healy & Mobbs 1994) and the 308K isopleth can be interpolated accordingly. The 10 km wavelength falls within the range of wavelengths that can be trapped in the 3700 – 4200 m altitude range, according to Section 3.6.4.

When the data from the vertical velocity graph in Figure 3.19 is compared to the isopleth estimation, it is clear that updraft peaks are situated on the leading edges of wave crests (light blue arrows) and downdrafts on the trailing edges of the crests (red arrows). This then coincides with the description of mountain waves as shown in Figure 1.1. The wave trough situated at approximately the 13 km mark supports the negative horizontal vorticity area associated with troughs as mentioned in Section 3.7.3.
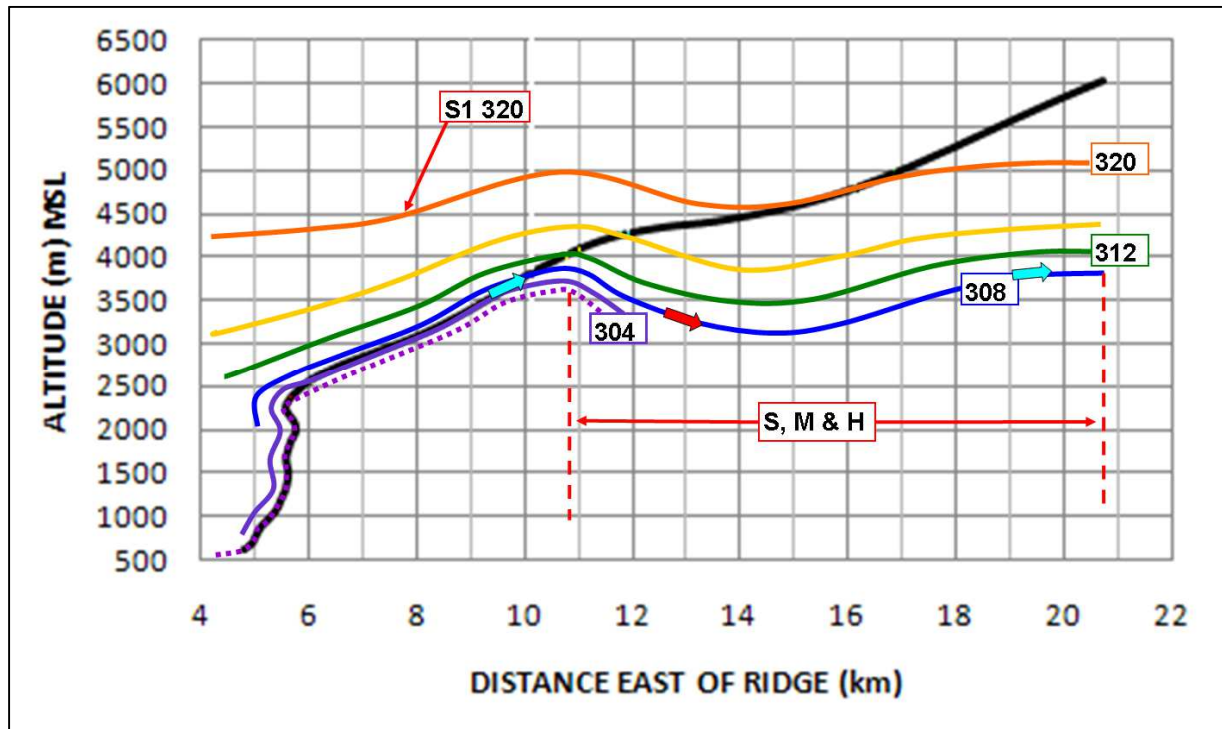
Figure 3.23: Isopleth estimation for S2.

3.8   Sounding 3 (S3)

3.8.1   S3 Profile

The profiles of S2 and S3 are compared in Figure 3.24 with S2 in red and S3 in black. Up to the 7.8 km mark in the horizontal the two profiles show very little resemblance. S2 experienced reversed flow which was not clearly seen in S3. S3 rose rapidly up to 1500 m, from where a decrease in the rate of climb is observed. A small kink is observed at the 6 km mark, in what is otherwise a smooth curve. From 7.8 km onwards the two curves are very similar in appearance,

except for S3 showing a drop in altitude from a relative maximum at 12.5 km from the ridge to a relative minimum at about 14.5 km. This drop in profile was not observed in the case of S2. A further discussion on the drop in the S3 profile curve follows in Section 3.8.4.
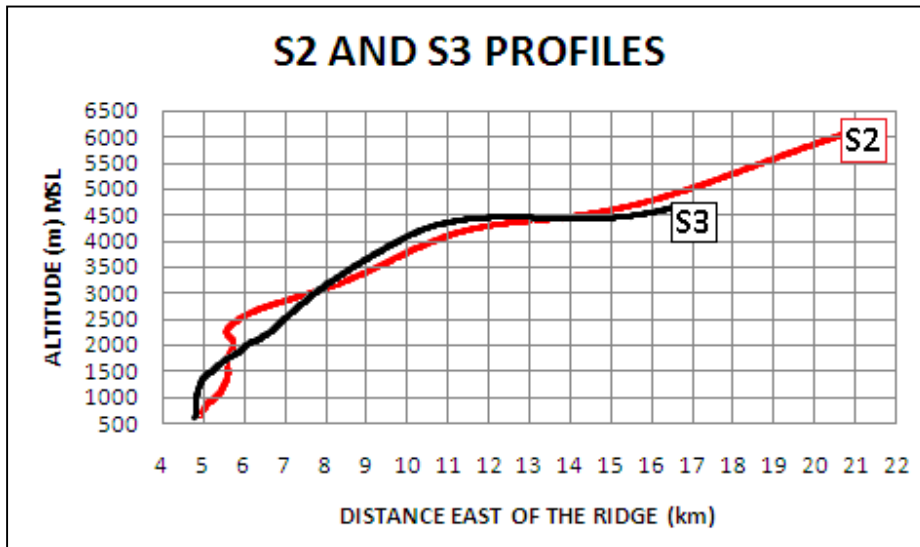
Figure 3.24: S2 and S3 profiles compared.

The profile for below 2200 m above MSL is shown in Figure 3.25. A red circle highlights a near vertical part of the curve. The one second D-Met raw data shows this vertical section containing reversed flow of about 1.8 m, which is not visible in Figure 3.25. Two blue circles mark areas where a slight drop in the slope of the profile curve is observed.
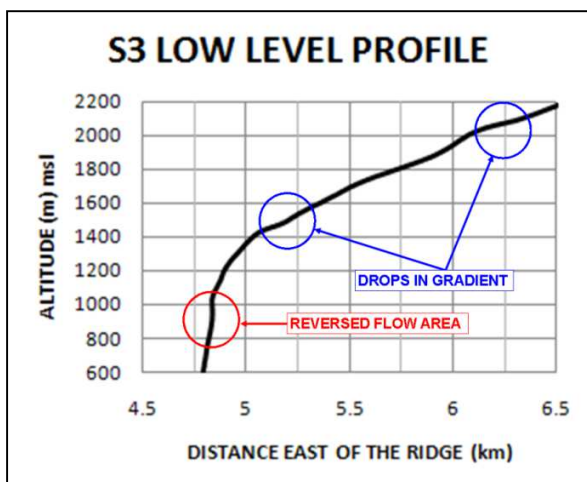
Figure 3.25: S3 low level profile showing reversed flow and flattening areas.

3.8.2 S3 Richardson number (Ri)

The S2 and S3 Richardson numbers (Ri) for 300 m vertical intervals are shown in Figure 3.26 with values plotted against the upper limit of each level. The S3 data is shown as black crosses with grey dotted lines joining consecutive points, while S2 data is shown as red diamond shaped points, joined by red dotted lines. The 12 layers above 900 m were compared. For S3 75% of the atmosphere was stable (Holton 1992). Four values, representing the layer between 900 and 2100 m, lay within the critical interval of (0; 0.25], indicating areas within the stable atmosphere where turbulence may occur (Chan 2008; Gossard & Hooke 1975; Holton 1992; Huschke 1959). In contrast 92% of the layers above 900 m were stable in the case of S2, with the critical layer lying between 1200 and 2700 m. The comparison proves that a low level layer, where turbulence was possible, was sustained during the one hour period between the two soundings. Although the upper and lower limits of the turbulence areas were different, turbulence could at least be sustained through a 900 m depth of the atmosphere between 1200 and 2100 m above MSL.
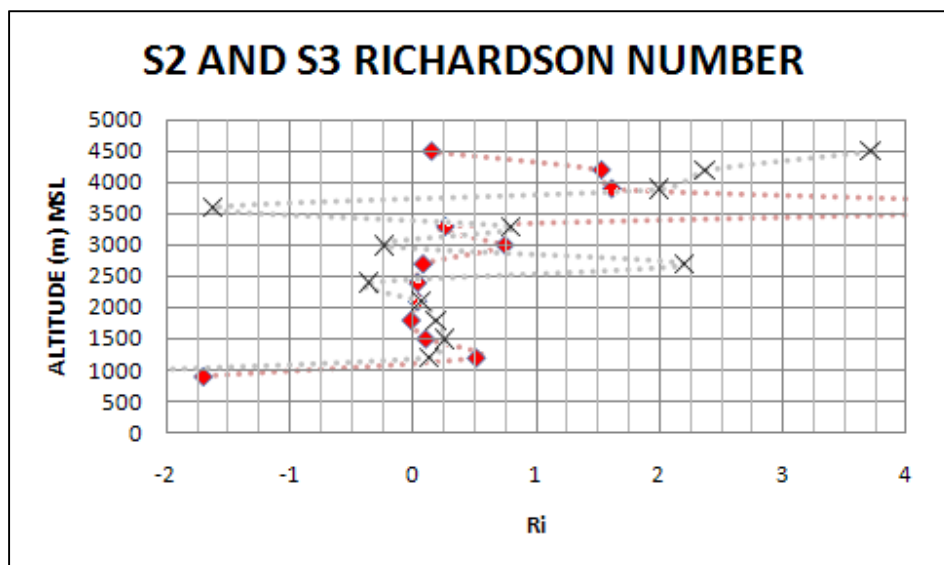
Figure 3.26: Comparison between the Richardson numbers of S2 and S3.

3.8.3 S3 Horizontal vorticity (η)

Figure 3.27 compares the S3 y-component of the horizontal vorticity (η) with the S3 profile. The red area represents a large area at low levels where η is positive. Any rotor development below the main wave will then correspond to type 1 rotor development (Hertenstein & Kuettner 2005). The light blue area of negative η is very small and coincides with a very slight counter clockwise curvature in the profile curve between 1750 and 2100 m above MSL. The most prominent feature is the negative η value of -0.24 s⁻¹ associated with the counter clockwise curvature observed near the 4400 m level and indicated by green. This curvature occurs over a horizontal distance of about 2 km. According to Hertenstein & Kuettner (2005) and Doyle and Durran (2001), this negative η area is typical of a wave trough and also appears to be a trough from the profile shape in Figure 3.27.
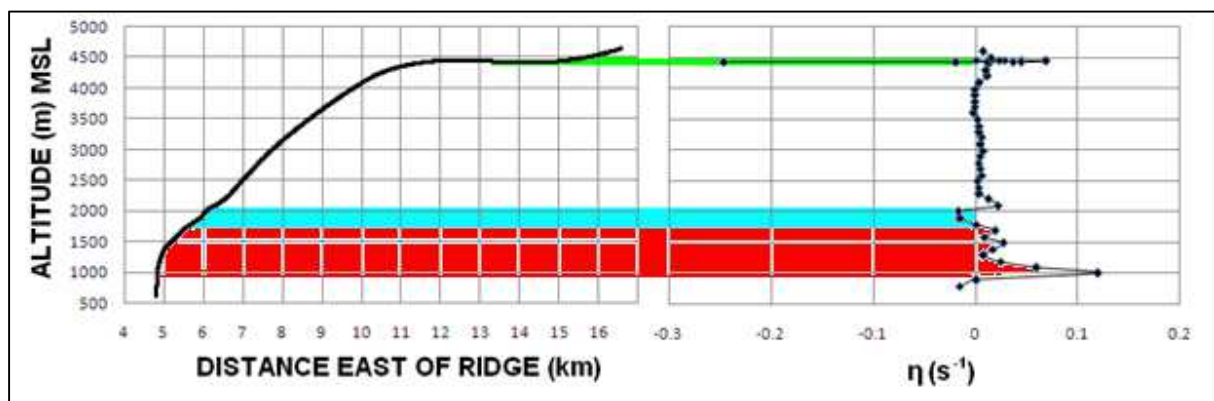
Figure 3.27: Comparison between S3 profile and y-component horizontal vorticity.

In Figure 3.28 η values of S2 (red) and S3 (black) are compared. At or below the 2000 m level, the S2 data show two excursions into negative η values, in an area where S3 experienced positive η values (indicated with red). The S3 data thus conform better to the ideas of Doyle & Durran (2001) regarding predominantly positive η in rotors, than in the case of S2. S3 shows two smaller areas of negative η (blue and green areas). The green area of negative η more or less coincides with a similar area in the S2 data, but its higher negative value of -0.24 s⁻¹, is associated with a drop in the profile curve, not merely a decreased gradient as was the case with S2.
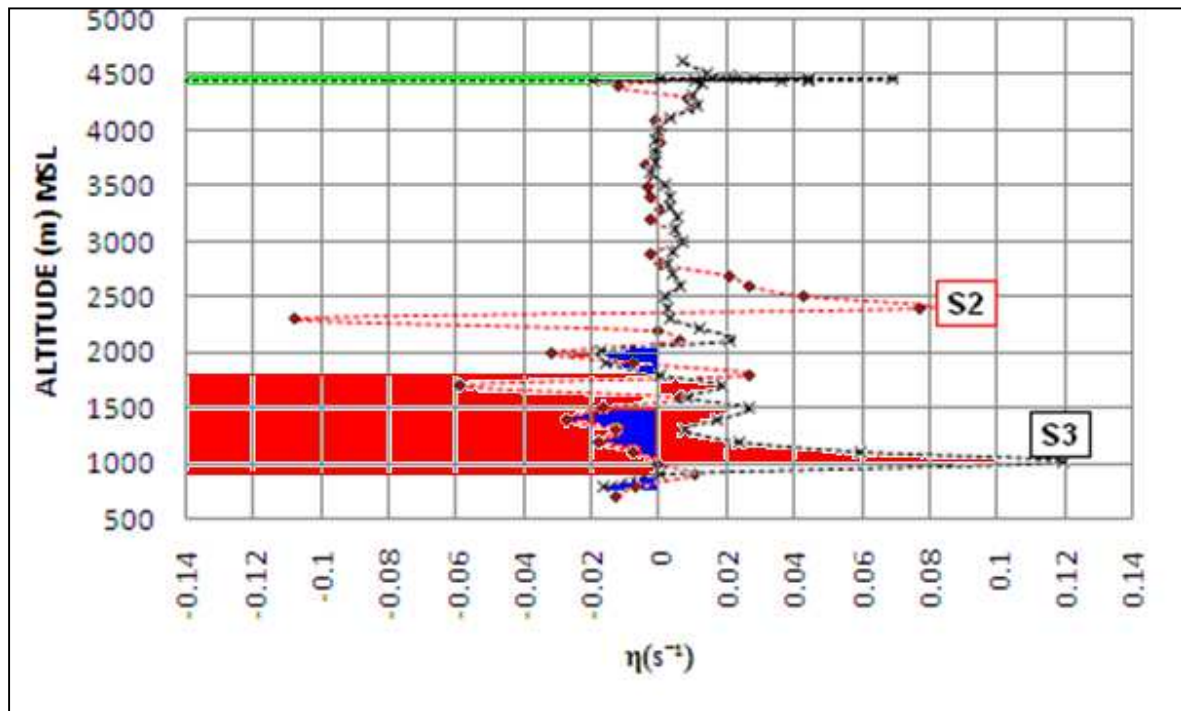
Figure 3.28: Comparison between S2 and S3 y-component horizontal vorticity.

3.8.4   S3 Balloon ascent rate

The S2 and S3 ascent rates are compared in Figure 3.29 with red representing S2 data and black S3 data. Vosper & Mobbs (1996) had results from soundings conducted from the same launch site in the Falkland Islands between five and eight minutes apart as opposed to the 61 minutes between the S2 and S3 launch times. They showed that the peaks and troughs of the ascent rate against horizontal distance aligned well. To this phenomenon they referred to as phase line tilt. The two graphs bear little resemblance for the first 9.5 km east of the ridge. Thereafter they compare well, suggesting that phase line evidence could be found for the data beyond the 9.5 km mark.   Like the case of S2, the S3 ascent rate graph also shows a fluctuation between five and six kilometers east of the ridge. The magnitude of this fluctuation was 3.8 ms^{-1}.
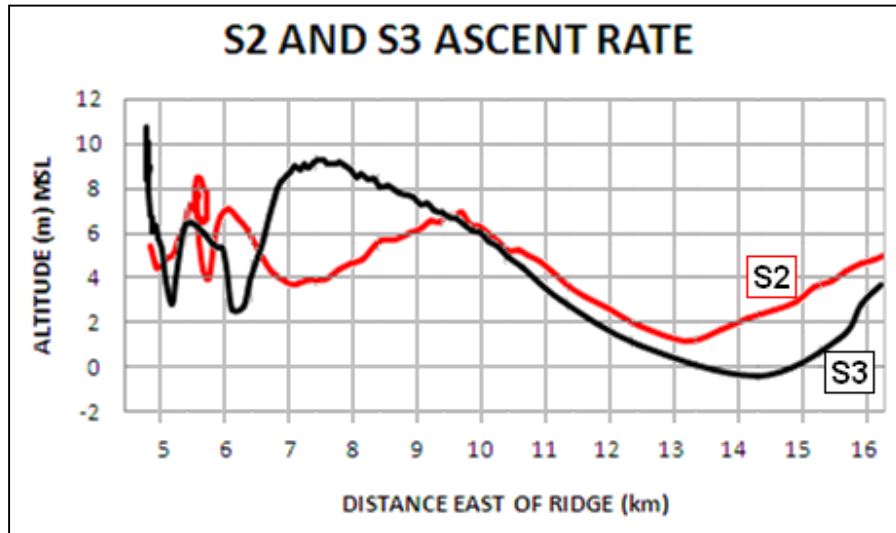
Figure 3.29: The ascent rates of S2 and S3.

The S3 ascent rate dropped from an initial high ascent rate to a local minimum value at the 5.2 km mark. This minimum coincides with a momentary flattening of the profile curve shown as a green area on the profile curve in Figure 3.25. A second local minimum at 6.25 km also coincides with a profile flattening (yellow area in Figure 3.25). Since a second ascent rate peak was not measured, peak to peak distance for wavelength calculation (Shutts, Healy & Mobbs 1994) could not be measured. By interpolation, assuming the gradient between 14.3 and 16.3 km to be maintained, a theoretical peak could be assumed to lie at the 18.7 km mark. This produces a wavelength of approximately 11.2 km (18.7 – 7.5 km). The negative ascent rate observed between 13.3 and 15.0 km corresponds well with the area of descent observed in the S3 profile (Figure 3.24).

3.8.5   S3 Vertical velocity

As was the case was with S2, the methods of Grubišić & Billings (2007) were used to calculate vertical velocity for S3. The results are shown in Figure 3.30 where downdrafts (green areas in upper part of the image) are associated with flattening in the profile curve (green parts of the bottom curve). Up to the 6.5 km mark this effect is slight with vertical velocity reaching approximately -2 ms^{-1} and the associated flattening in the profile curve being marginal.

However, from the 10.6 km mark the vertical velocity drops to -5 ms^{-1} over a much longer horizontal distance with a visible drop in the profile curve. Near the same distance from the ridge the S2 curve experienced flattening, but not a drop in altitude, with the associated downdraft of -4 ms^{-1}. For the size of balloon used in this study, it would thus appear that the downdraft speed needs to exceed -4 ms^{-1} for the balloon to lose altitude – the latter being indicated by a dip in the profile curve.

Areas in Figure 3.30 not marked with green represent updrafts where the velocity values are positive. Peaks in the vertical velocity curve that mark local maximum updrafts are observed near the midpoints of steepening areas in the profile curve. From the discussion in Section 3.7.6 it is expected that the areas of updrafts and downdrafts of S3 will be visible in the isopleths estimation that follows.

While the fluctuation in ascent rate between the five and six kilometers marks (Figure 3.29) are indicative of possible rotor activity, Figure 3.30 shows that the associated updraft occurred below the summit level. Thus according to Hertenstein & Kuettner (2005) the rotor was a type 1 rotor.
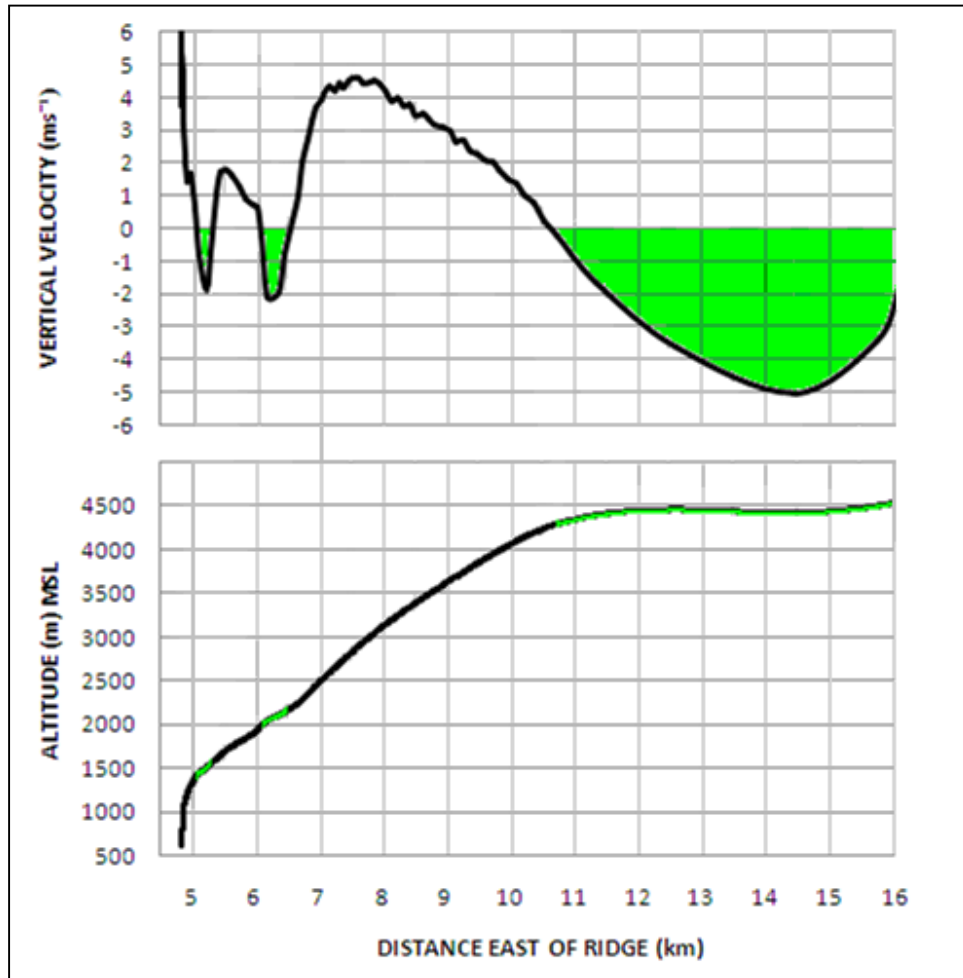
Figure 3.30: S3 vertical velocity.

3.8.6 S3 Potential temperature (θ) and isopleth estimation

Ignoring an initial spike, the S3 potential temperature (θ) graph in Figure 3.31 shows a general increase in θ and thus atmospheric stability up to 2500 m above MSL (Doyle & Durran 2007). An area of neutral stability lies between 2500 and 4000 m, above which a sharp increase in θ indicates very stable air above 4000 m.
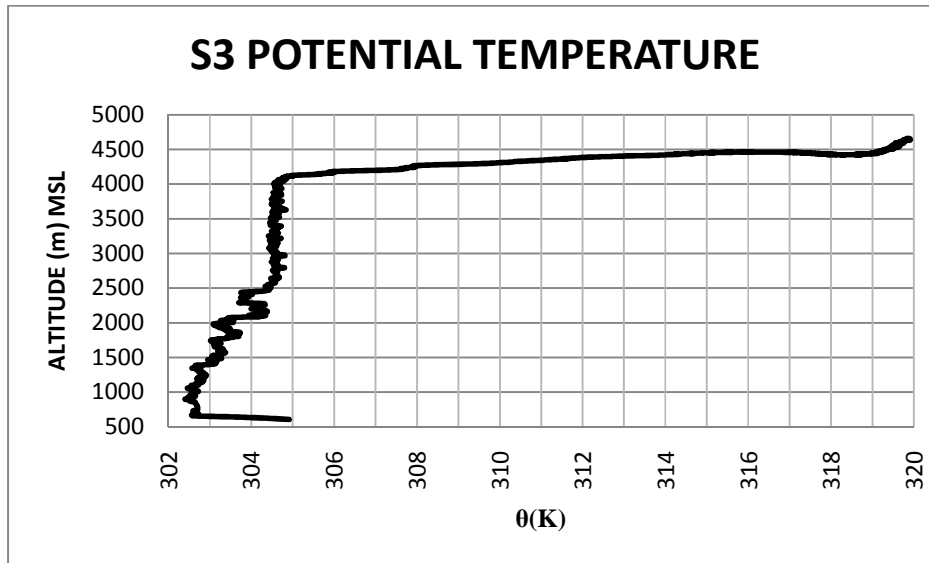
Figure 3.31: S3 Potential temperature.

The θ graphs of S2 and S3 below 2500 m above MSL are compared in Figure 3.32. S2 data is shown in red and S3 data in blue. At these lower levels the S3 θ values were higher than that of S2. The general trend at these levels was for a sharper rise in S3 θ, thus at first glance S3 appears more stable than S2 below 2500 m according to Doyle & Durran (2007), Holton (1992) and Stull (1991). However, the S3 θ showed larger amounts of decreased θ (instability) and deeper layers of instability than S2, with drops of 0.6 K between 1850 and 2000 m (indicated by green arrow) and 0.7 K between 2150 and 2300 m (light blue arrow). The S2 unstable regions were represented by a 0.4 K drop between 1800 and 1900 m (yellow arrow) and a 0.6 K drop between 2200 and 2300 m (orange arrow). Both soundings showed these unstable areas at approximately the same levels. S3 thus also showed favourable conditions for rotor and sub-rotor development, with stronger instability than the S2 case. The fact that the sounding profile failed to show reversed flow is probably a function of the trajectory of the S3 balloon and does not disprove rotor development in the S3 atmosphere. In the Falkland Island study Mobbs *et al.* (2005) also found that consecutive balloon soundings did not always show the same features as a result of different balloon trajectories.
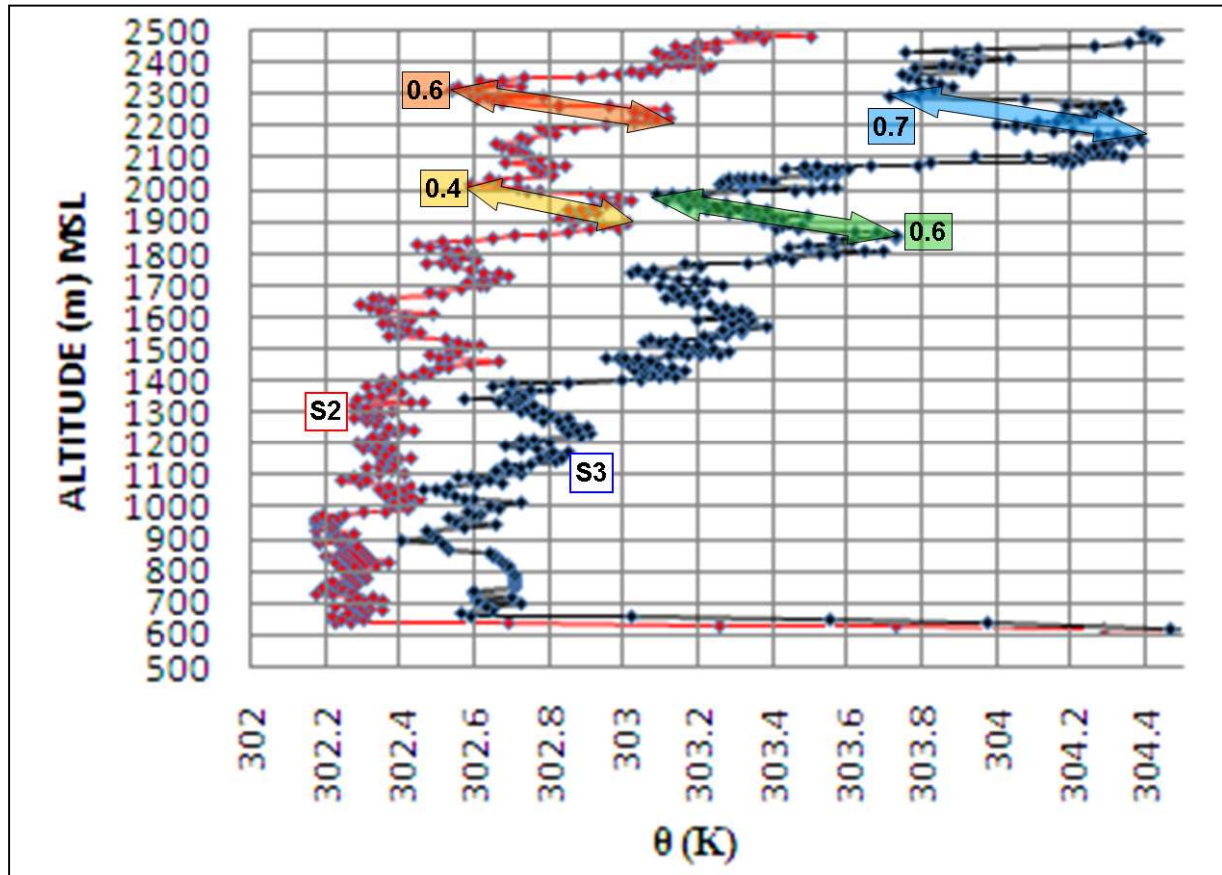
Figure 3.32: S2 and S3 Potential temperature comparison for the sub-summit levels.

The isopleth estimation for S3 is shown in Figure 3.33. The 304.5 K isopleth follows the profile line (black) for approximately 1450 m of altitude. Guided by the position of the 303 K isopleth, the 304.5 line follows the profile line closely. Using these two isopleths the 308 K isopleth could be interpolated to where it crossed the profile line 10.6 km east of the ridge. This is also the point in the vertical velocity curve where the most prominent downdraft starts (see Figure 3.30) so that the primary wave crest is estimated to lie at 10.6 km east of the ridge line. The 308 K isopleth for S3 attained a higher altitude than its S2 counterpart, indicating an increase of approximately 450m above MSL in the amplitude of the wave. The 318 K isopleth crosses the profile curve near the 14 km mark. At that point the vertical velocity graph (Figure 3.30) shows a value near -5 ms^{-1} forcing the balloon to lose altitude. This information helped in placing the isopleth in a downward configuration on the lee of a mountain wave crest. The 312, 360 and 320 K were interpolated from the positions of the other isopleths.

The maximum updraft and downdraft positions are indicated with respectively light blue and red arrows. The updraft occurred on the leading edge of the primary wave with the downdraft on the lee side of the wave crest.
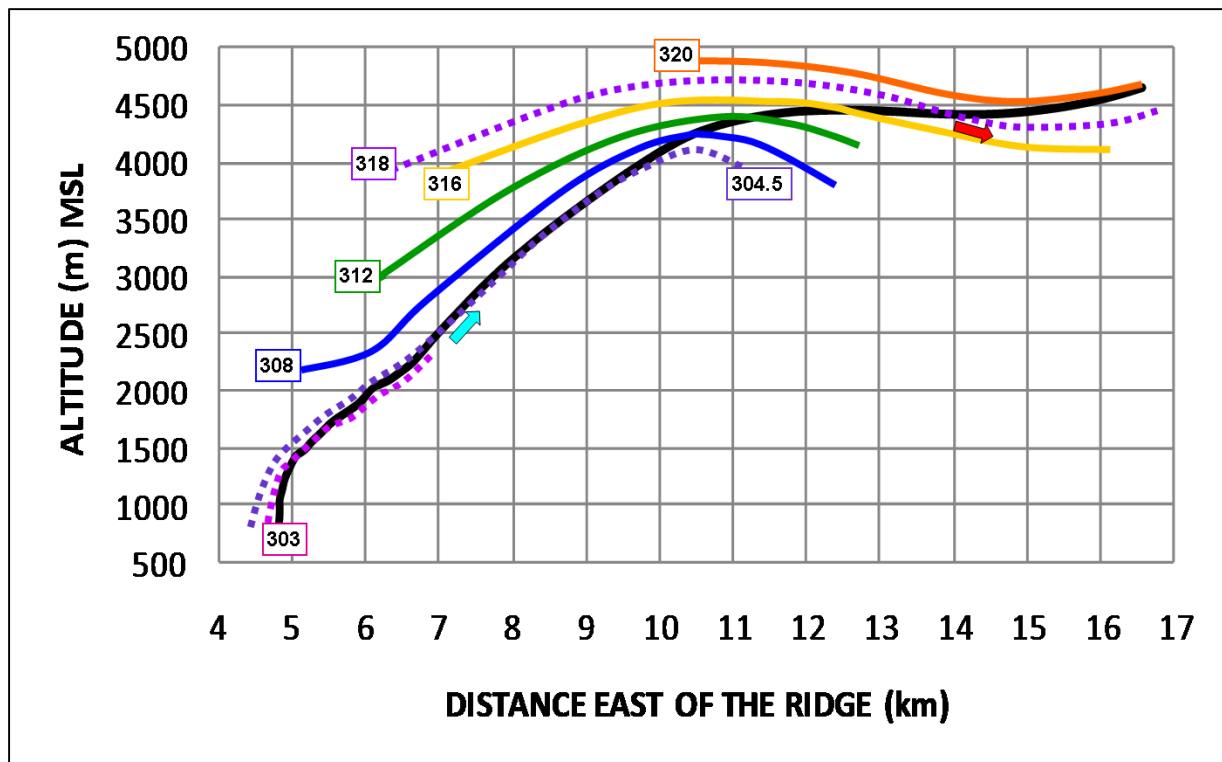
Figure 3.33: Isopleth estimation for S3.

3.9   Sounding 4 (S4)

3.9.1   S4 Profile and track

Figure 3.34 shows the ascent profiles for S2, S3 and S4 in respectively blue, red and black. Like S2, S4 shows reversed flow at low levels. This reversed flow occurred below 1500 m while that for S2 occurred between 1500 and 2500 m. This may indicate that the rotor was encountered in the S4 case much earlier than was the case with S2. The S4 profile further shows an abrupt drop in altitude of 160 m during the low level ascent, which neither S2 nor S3 shows. Like S3, the S4

profile shows a drop in altitude near the 4500 m above MSL level, but some 3 km further downstream.
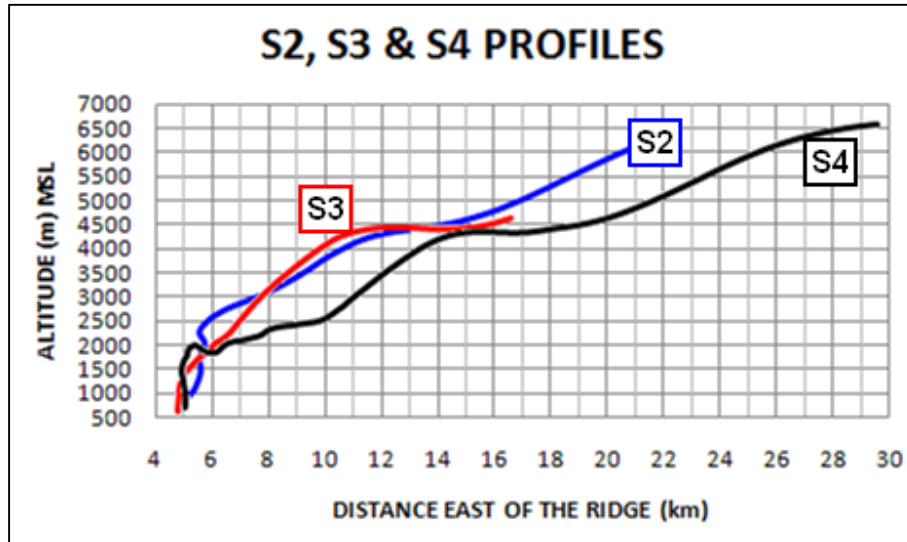
Figure 3.34: S2, S3 and S4 profiles.

In order to visualise the reversed flow better, the tracks of S2, S3 and S4 are shown in Figure 3.35 as respectively red, black and blue curves. S2 and S3 share an origin, but S2 shows nearly 1000 m of movement in an ENE direction, before it encounters reversed flow and finally reaches the overhead NW wind-driven zone of the main wave.   The reversed flow area was about 232 m long along a W-E axis. In contrast S4 shows reversed flow much sooner, with an estimated W-E distance of 167 m.
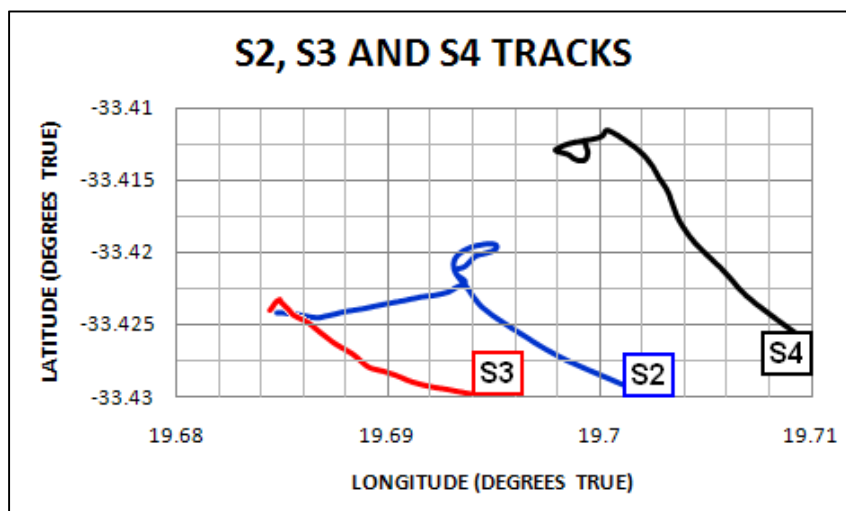
Figure 3.35 Sounding tracks for S2, S3 and S4.

3.9.2   S4 Richardson Number (Ri)

The Ri values for S4 are shown for 300 m vertical intervals in Figure 3.36 as blue diamond shapes, S3 as black crosses and S2 as red dots. The entire S4 sounding above 1000 m passed through a stable atmosphere as is evident from the positive Ri values (Holton 1992). The entire set of data also lay below the 0.25 critical value indicating that the stable air could sustain turbulence (Chan 2008; Gossard & Hooke 1975; Holton 1992; Huschke 1959). In comparison to the S2 and S3 Ri data, S4 showed sustainable turbulence at all levels between 1000 and 3500 m, compared to smaller layers of sustainable turbulence by S2 (1000-2100 m) and S3 (1500 and 2700 m). There was thus a vertical increase in the layer of the lower atmosphere that could sustain turbulence as measured by S4 later in the afternoon.
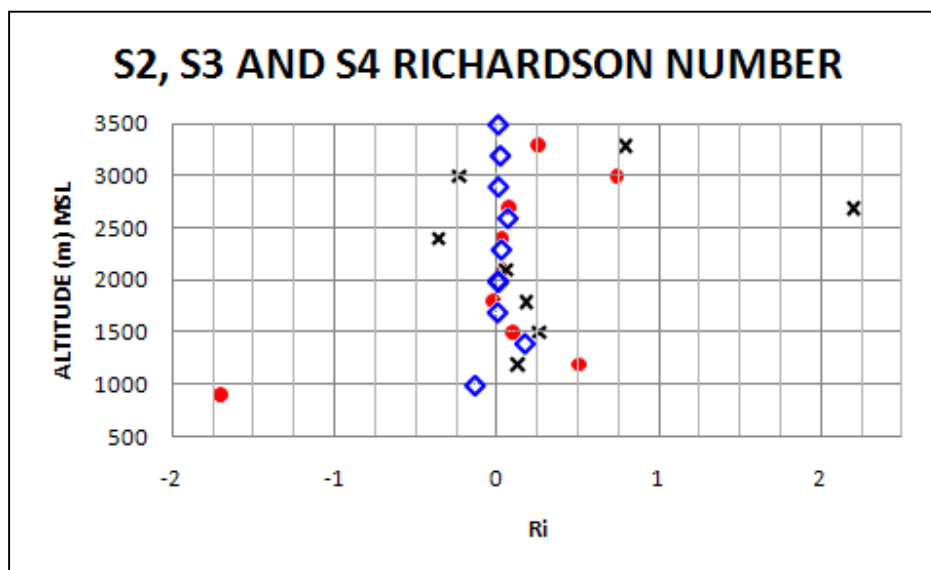
Figure 3.36: The Richardson numbers for S2, S3 and S4.

3.9.3   S4 Horizontal Vorticity (η)

Figure 3.37 compares the profile curve and η for S4. At 1400 m above MSL the reversed flow shown is associated with a η value of -0.04 s^{-1} and is marked by the dark blue line. More distinct counter clockwise curvature around the y-axis is associated with negative η values indicated by

light blue, light green and dark green. Light blue shows an area of -0.06 s^{-1} which is associated with the sudden 160 m drop in altitude which occurred between 1750 and 2000 m above MSL. This is indicative of a trough in the wave (Doyle & Durran 2007; Hertenstein & Kuettner 2005). A red line indicates the most prominent feature in Figure 3.37. The high positive η value indicates a vorticity strong enough for the balloon to have lost altitude. The value itself compares well with the results of Doyle & Durran (2001) indicated in Appendix B, Figure B.3. The wind speed detected by the balloon prior to the dip indicated reversed flow of only 2.8 ms^{-1} and appears to have been measured on the leading edge of a rotor. In Appendix B, Figure B.3 Doyle & Durran (2001) indicate a 17 ms^{-1} reversed flow in the centre of the rotor. Had the trajectory of the balloon been slightly further east of the mountain, a stronger reversed flow was likely to have been detected.

The negative η values of the light green area may once more show evidence of a trough in the main wave. Another trough in the wave is indicated by a negative η value of -0.24 s^{-1} at approximately 4300 m. Like the case with the 4400 m level of S3, this drop occurred over a large horizontal distance. Vertical resolution for the η graph is 100 m, except where the sounding profile showed drops in altitude. For such incidences the vertical intervals were adjusted to downward and upward movement of the balloon. From Figure 3.27 and 3.37 it is observed that drops in the profile curve are associated with η values of -0.06s^{-1} or lower.
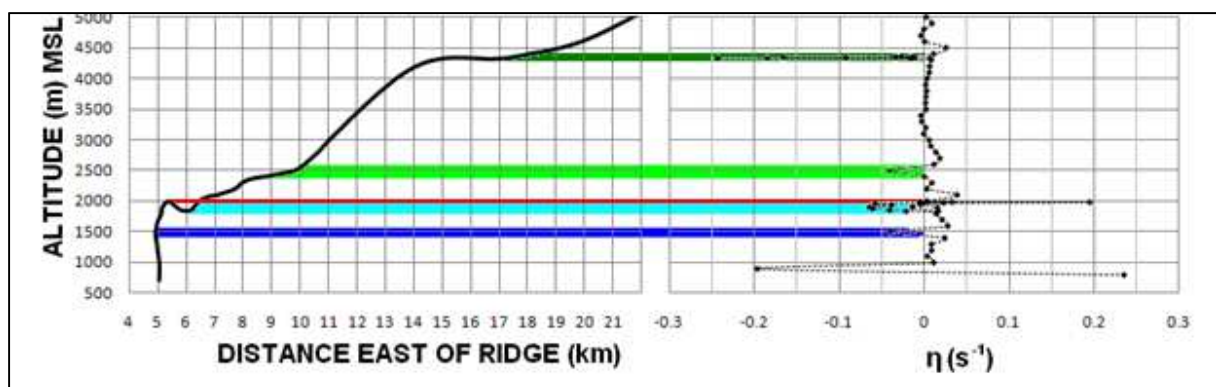
Figure 3.37: Comparison between S4 Profile and y-component horizontal vorticity.

3.9.4   S4 Balloon ascent rate

The relationship between reversed flow and ascent rate is shown in Figure 3.38. The first average value (11 ms^{-1}) was identified as a spike in the data where after the values are in order. Points indicated in red represent reversed flow. This is associated with an increase in ascent rate of 2 ms^{-1}. This increase took place over a horizontal distance of 140 m. This can be compared to S2 which experienced reversed flow over a horizontal distance of 110 m with 1.6 ms^{-1} increase in ascent rate.
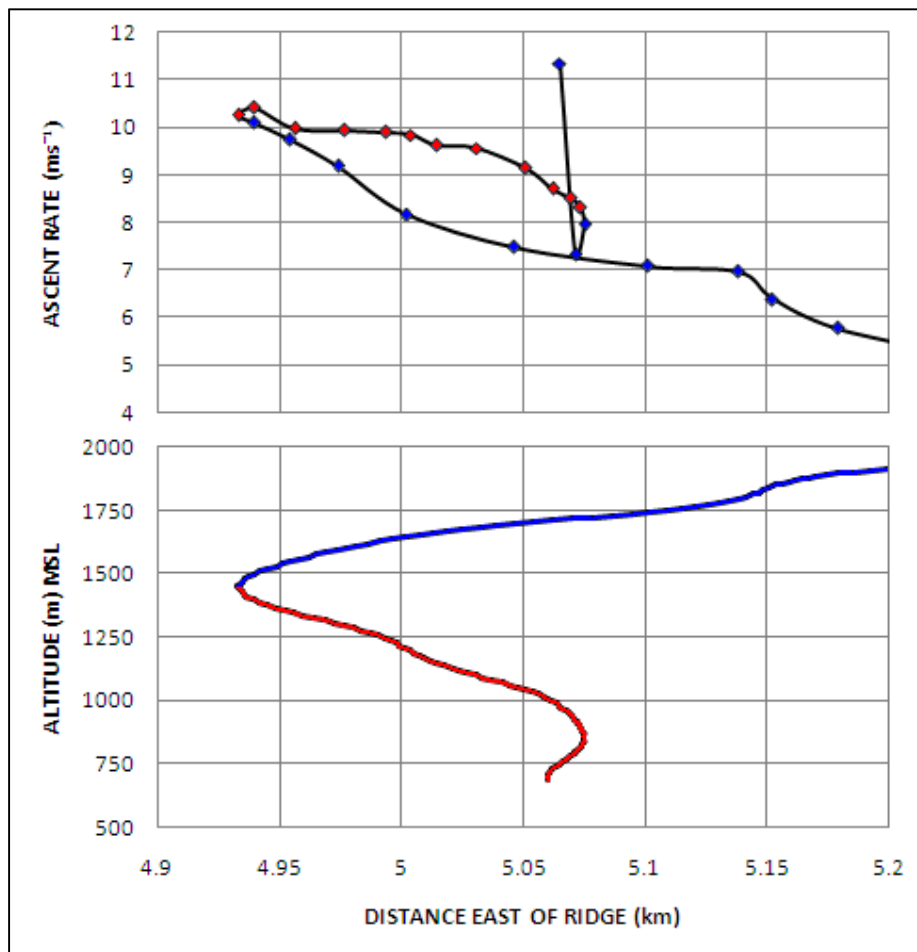
Figure 3.38: S4 ascent rate against reversed flow.

The entire ascent rate curve is shown in Figure 3.39. The thickening in the ascent rate curve near its start is the result of the reversed flow mentioned earlier. Like the ascent rates of S2 and S3,

S4 was marked by an abrupt decline in ascent rate early in the ascent to a minimum at the 5.6 km mark just before the balloon reached the local profile relative minimum at 6.0 km. The 6.4 and 8.0 km mark peaks in the ascent rate are associated with slightly steeper rises in the profile. The midpoints of the other peaks in the ascent rate curve match the approximate midpoints in the rises between 11 and 14 km and 23 and 25 km along the profile curve well. Between the two peaks the local minimum in the ascent rate curve occurs just before the local minimum in the profile curve is reached at 17 km.

Figure 3.39 shows a very significant fluctuation in the ascent rate curve up to about 6.5 km east of the ridge. This fluctuation includes both a 13 ms^{-1} drop in ascent rate and a 7.5 ms^{-1} increase in ascent rate. Both of these measurements exceeded the value of 7 ms^{-1} from the Falklands study of Mobbs *et al*. (2005), which may suggest the existence of a type 2 rotor, provided that the fluctuation occurred up to an altitude exceeding that of the mountain ridge (Hertenstein & Keuttner 2005).
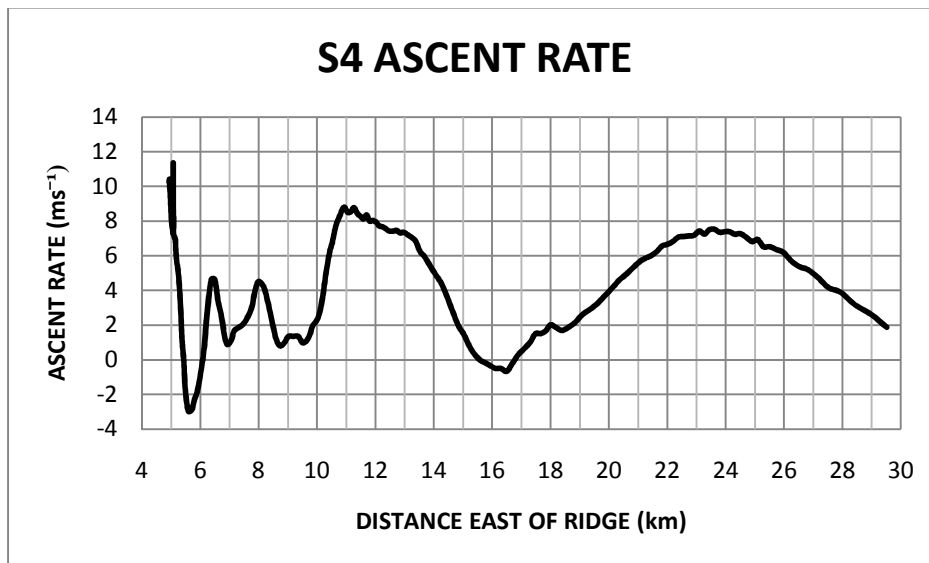
Figure 3.39: S4 ascent rate

Peak to peak distances can then be taken as 23.5 – 11.0 = 12.5 km which is an estimate of wavelength according to Shutts, Healy & Mobbs (1994).

3.9.5   S4 Vertical velocity

In Figure 3.40 the red points indicate vertical velocity for the reversed flow area. The blue value above the 7 ms^{-1} was identified as a spike. The data shows that the reversed flow started at 5.07 km east of the ridge and moved the balloon 140 m westward. Over this distance the updraft speed increased from 4.1 ms^{-1} to 6.2 ms^{-1}. S4 thus experienced a larger rotor updraft than either of the S2 sub-rotors.
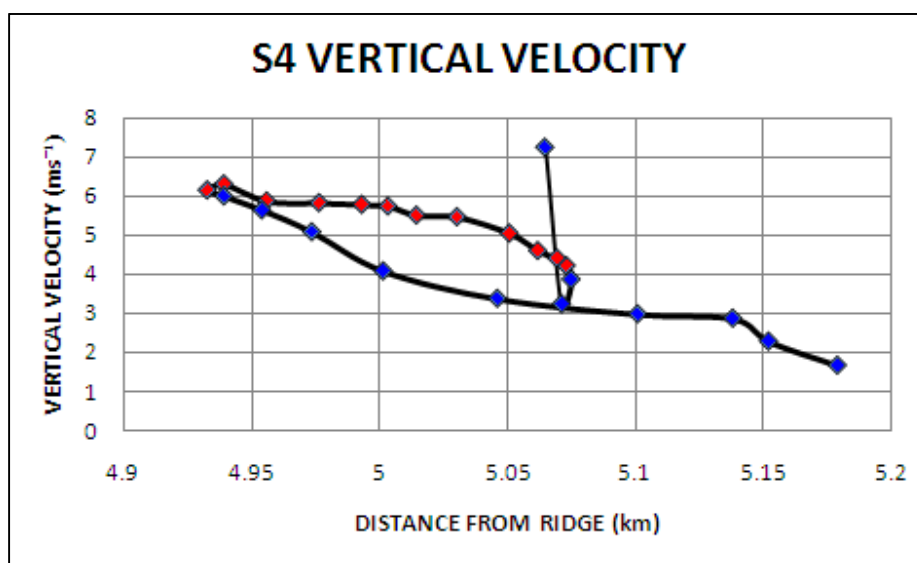
Figure 3.40: S4 vertical velocity during reversed flow.

Figure 3.41 compares the entire S4 vertical velocity and profile. The vertical velocity (up- and downdraft velocity) was determined by subtracting the average S4 ascent rate of 4.1 ms^{-1} from the actual ascent rate as was performed for S2 and S3 (Grubišić & Billings 2007). Areas of downdraft occurred more frequently for S4 than the previous ascents. All areas of downdraft were again marked in green and coincided well with flattening in the profile curve between the 7 and 10 km mark and beyond the 28 km mark. The two most prominent downdrafts were associated with drops in altitude in the profile curve. The first one of magnitude -7 ms^{-1} is observed near the 6 km mark and is associated with a drop in the profile curve of 160 m. The other such downdraft was approximately -5 ms^{-1} in magnitude and is associated with a small profile drop of 20 m. As was the case with S3, the downdraft velocity exceeded -4 ms^{-1} in

association with a drop in the balloon altitude (see Section 3.8.7). This downdraft occurred very gradually over a horizontal distance of 2000 m to where its negative peak was reached. In contrast the downdraft at the 6 km mark reached its negative peak within 310 m of horizontal distance.

From Figure 3.41 it is observed that the fluctuation in vertical velocity (and ascent rate) up to 6.5 km east of the ridge occurred below the level of the highest summit in the ridge. Thus any rotor development associated with these fluctuations are then associated with type 1 rotors (Hertenstein & Keuttner 2005).
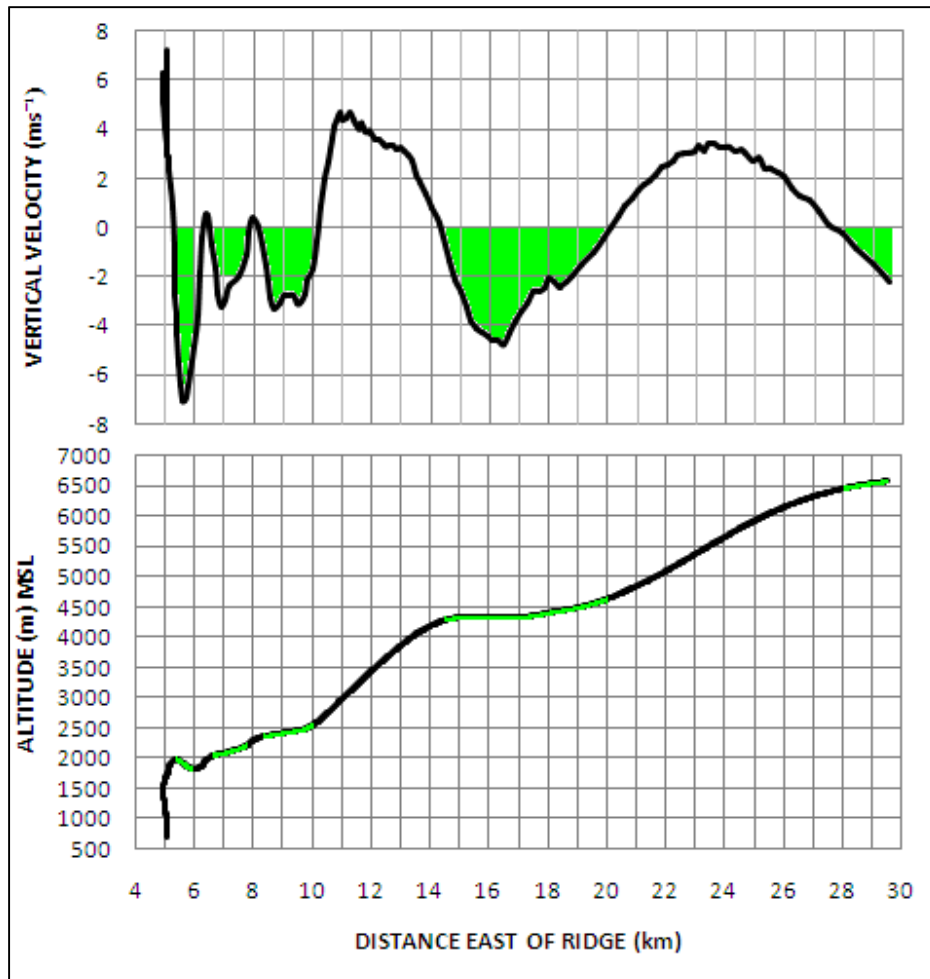
Figure 3.41: S4 ascent rate against profile.

This higher vertical velocity later in the day was a prominent feature in the SWP rotors as mentioned by Keuttner & Hertenstein (2002), when the rotors would reach a maximum intensity. The SWP observations also showed an increase in surface potential temperature of 2 K during the later part of the afternoon. The S2/S3 and S4 launch sites were not at the same altitude, thus a similar comparison could not be made.

A greater threat to flight safety than the updrafts of S4 is the downdraft observed commencing at the 5.6 km mark and attaining a maximum speed of -7 ms^{-1} over a 300m horizontal distance. This translates to a 1378 ft/minute downdraft.   Most single engine aircraft would struggle to maintain altitude in a downdraft of greater than 1000 ft/minute (Davis 2011, pers com). This downdraft was associated with flow of the main wave system rather than rotor flow underneath the wave. This is evidenced by the wind direction data near the 5.6 km mark where the drop in the profile occurred with which this downdraft is associated. The wind direction reached a NW true direction at an altitude of 1916 m above MSL.

3.9.6   S4 Potential temperature (θ) and isopleth estimation

The potential temperature (θ) plot for the entire S4 ascent (Figure 3.42) shows a slow rate of increase of about 3 K from the surface to 4100 m. Over the next 900 m of altitude, θ increased by 16 K.   The atmosphere thus appears stable on average (Doyle & Durran 2007; Holton 1992; Stull 1991) up to 4100 m, with a further increase in stability above that level.

S4 POTENTIAL TEMPERATURE
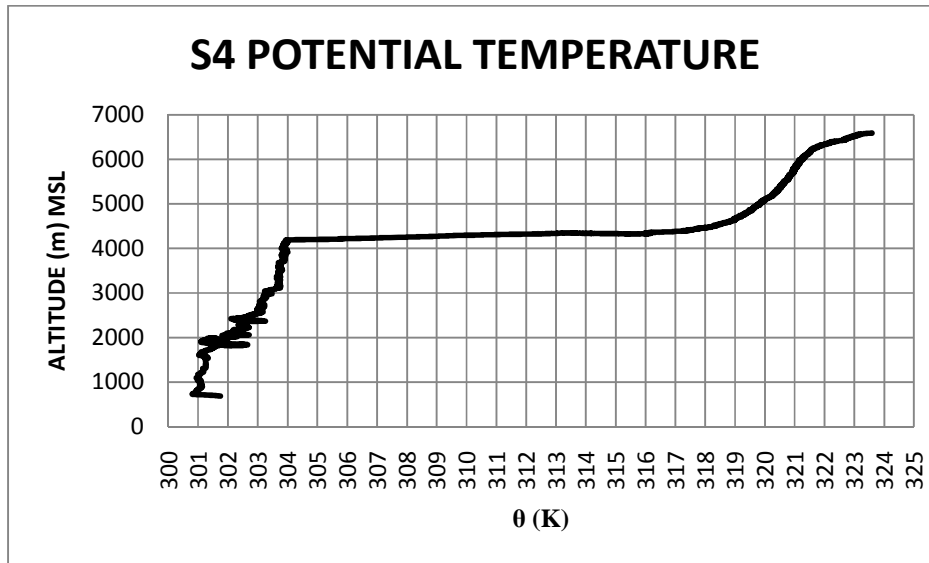
Figure 3.42: S4 Potential temperature

The largest variability in the graph lies below 2500 m. A comparison with θ values below this level is shown in Figure 3.43 with data for S2, S3 and S4 represented by green, red and blue respectively. S4 had the lowest potential temperature values of the three soundings. All three curves showed a small variation in potential temperature below 1400 m. S4 shows a slight drop in θ in the 900-1100 m layer (yellow layer) indicating slight instability (Doyle & Durran 2007). In this layer reversed flow occurred, hence according to Grubišić & Billings (2007) this area can be identified as a rotor area. Above 1800 m all three curves show unstable areas. Since the S4 balloon experienced a drop in altitude, its θ curve is more erratic than that of the other two soundings. The layer where S4 experienced a drop is highlighted with orange.
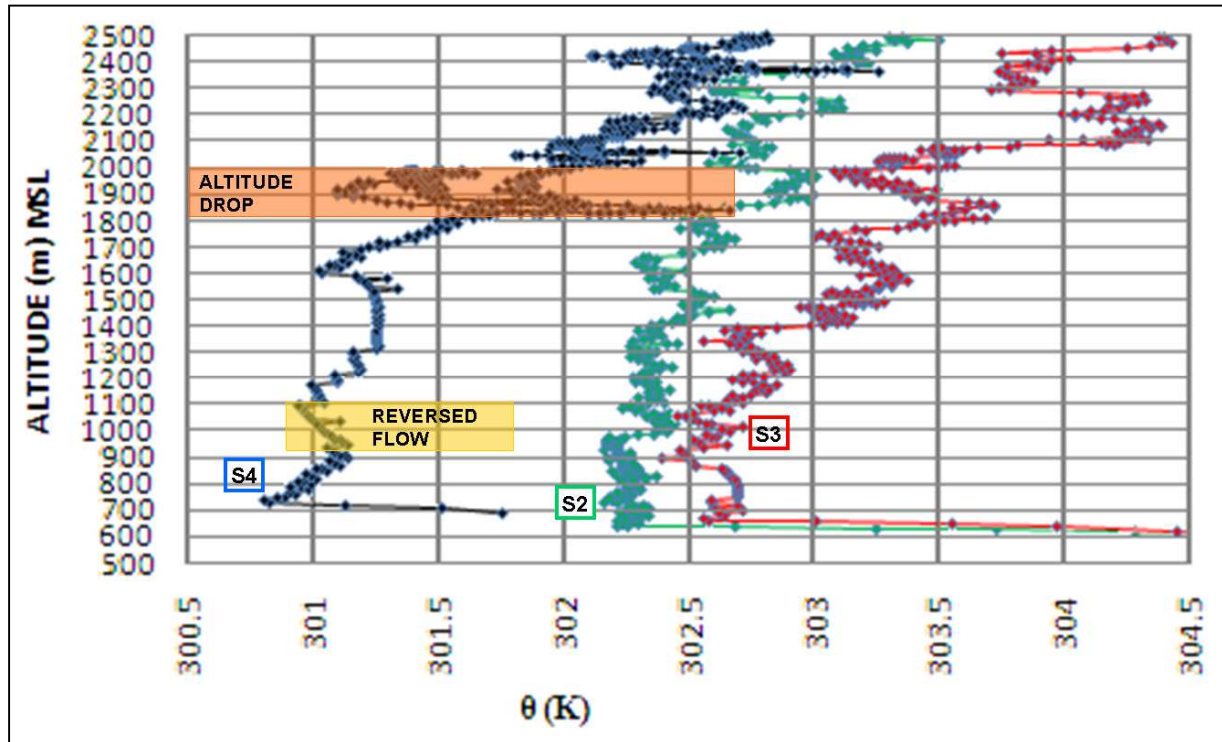
Figure 3.43: Potential temperature of S2, S3 and S4 below 2500m above MSL.

In order to show greater detail in the S4 θ curve, higher resolution graphs are produced in Figures 3.44 and 3.45. Figure 3.44 shows the period of the sounding when the balloon lost and gained altitude in the vicinity of the six kilometer mark east of the ridge. This period of the sounding was associated with the main wave rather than sub-wave rotors (Figure 3.41).

In Figure 3.44 three distinct colours are used to show the progression in time from an initial period in blue, through green to a final period in red. Pale blue areas highlight drops in θ in the 1840-1890 m and 1975-1990 m layers, marking unstable areas according to Doyle & Durran (2007). After the balloon reached approximately 1850 m it descended (green period). Slightly later the balloon rose again (red). During this period two more layers of instability are highlighted with pale red: 1865-1875 m and 1885-1915 m.
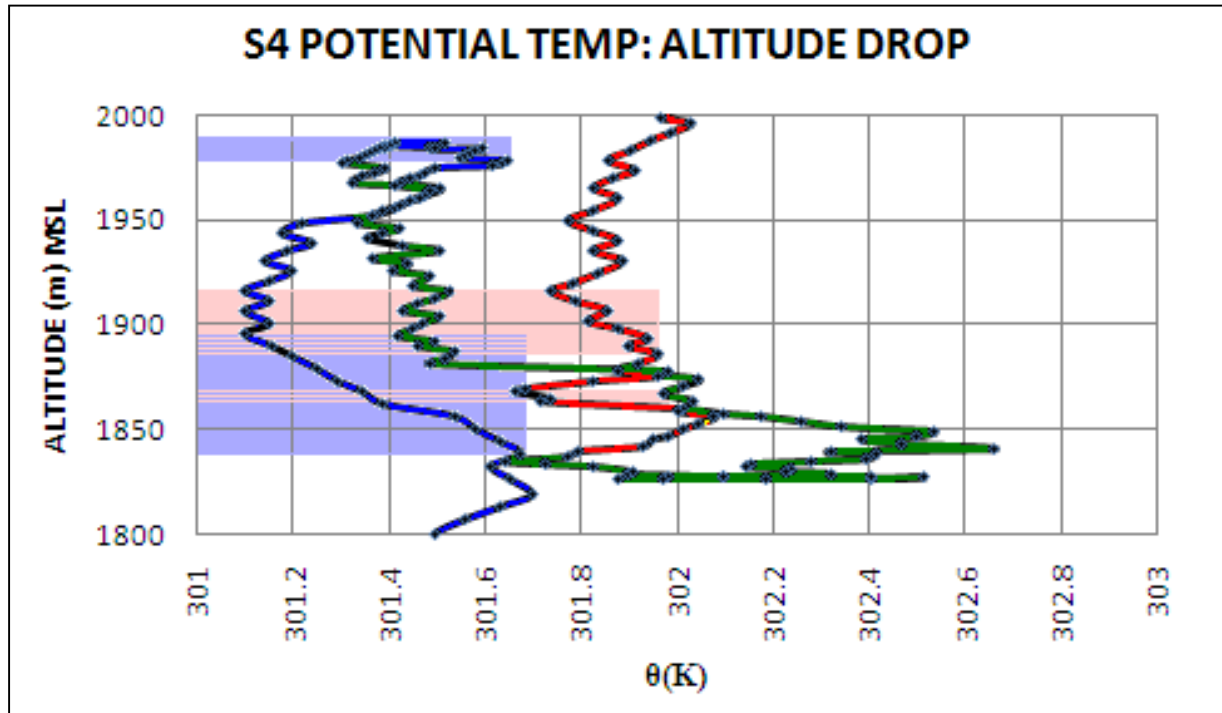
Figure 3.44: S4 Potential temperature for reversed flow region.

An unstable area is also identified for the 2360-2400 m above MSL layer where a 1K drop in θ was experienced (Figure 3.45). This part of the ascent was again associated with the main wave and marks a flattening in the profile curve near the nine kilometre mark (Figure 3.41).
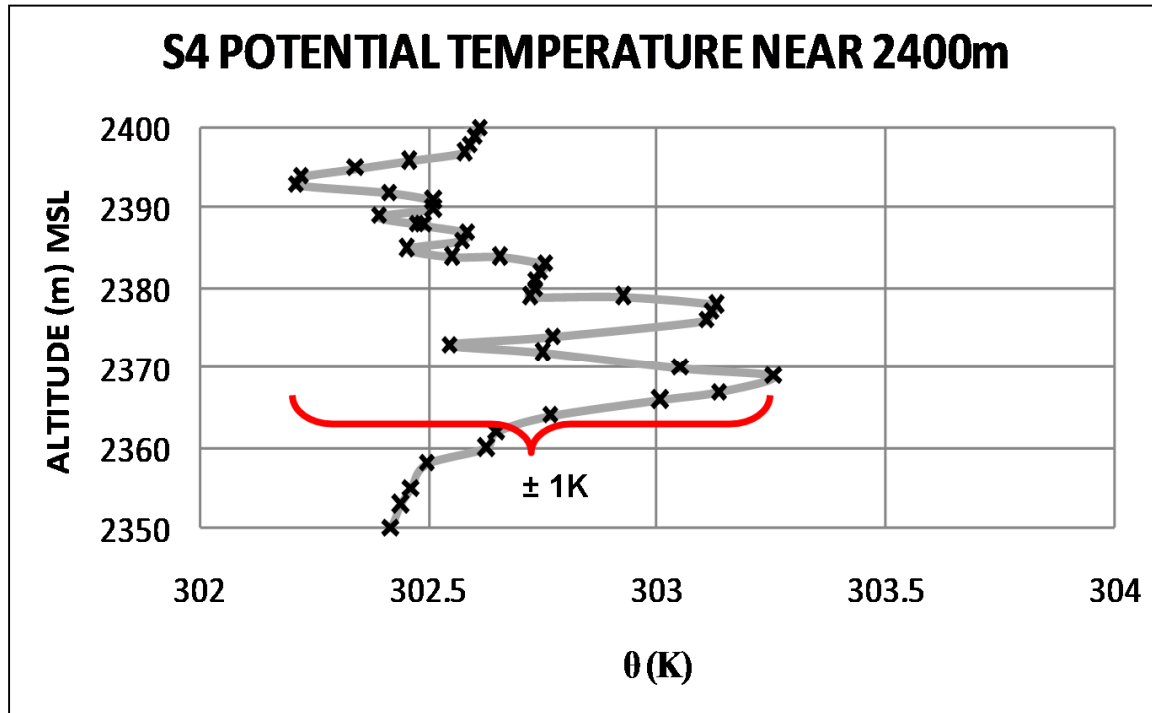
Figure 3.45 S4 Potential Temperature near 2400m above MSL

The isopleth estimation is shown in Figure 3.46. The 308 K isopleth intersects the profile curve at about 14.3 km east of the ridge. This point coincides with the start of a downdraft in Figure 4.36, making the 308 K isopleths once more a good estimator for the primary wave position. This position is indicated by red and purple dashed lines near the centre of Figure 3.46. From the theory of Shutts, Healy & Mobbs (1994) in Section 3.9.4, another red dashed line shows the position of the secondary wave crest at 26.8 km. Using the downdrafts from Figure 3.41, the secondary wave position can be placed at 27.5 km (purple dashed line) where the 322 K isopleth intersects the profile curve at the 6300 m altitude. Since it was established in Section 3.6.4 that trapped lee waves were likely, it can be assumed that phase lines tilt is vertical, according to Vosper & Mobbs (1996). If it is further assumed that trapped lee waves continued for the S4 case; then the 308 K isopleth has a crest directly below the 322 K isopleths, allowing for further interpolation of the lower isopleths. The wavelength determined by the use of downdrafts is well within the 2 km accuracy of the 12.5 km wavelength determined by the theory of Shutts, Healy & Mobbs (1994). The isopleth analysis supports the longer wavelength better. Updraft and downdraft maxima are indicated by light blue and red arrows respectively.
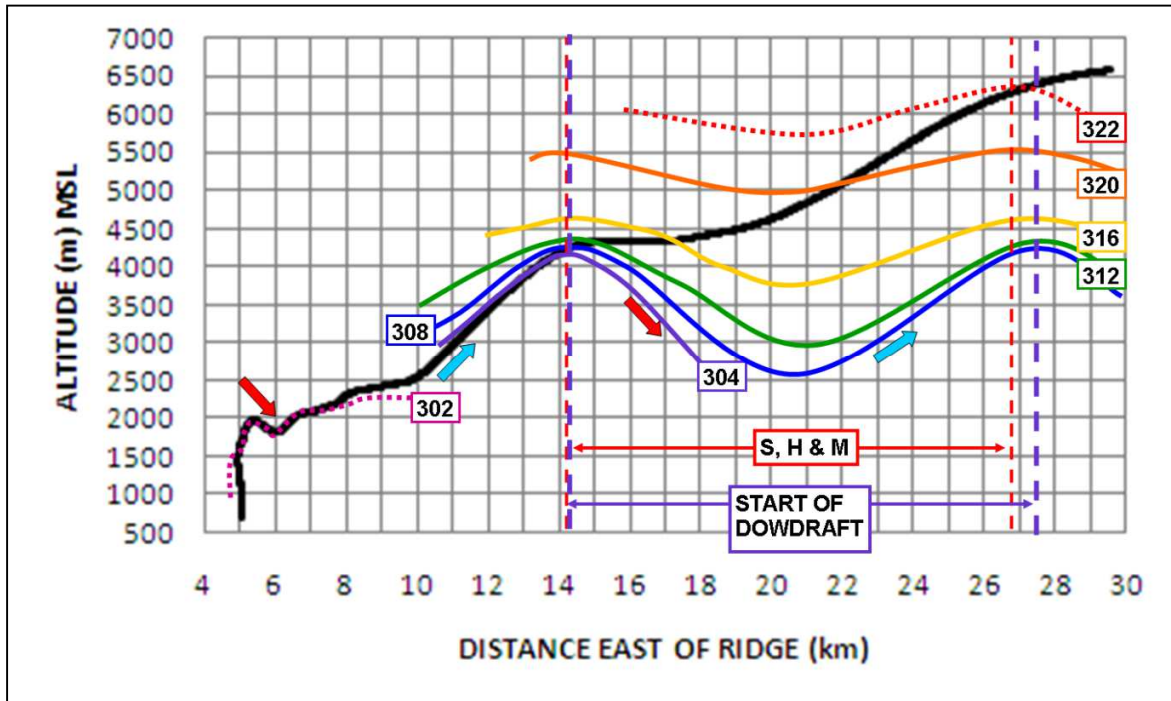
Figure 3.46: S4 Isopleth estimation

3.10   Comparison between S2, S3 and S4 features

In Figure 3.47 the primary wave positions as indicated by the 308 K isopleths of S2, S3 and S4 are compared. The S2 and S3 primary waves are at approximately the same position east of the ridge (10.6 - 10.7 km). However there is a clear increase in the amplitude of the waves over time, with S3 having wave amplitude 440 m higher than that of S2. The S4 primary wave position has shifted some 3.7 km eastwards from that of S2 and S3.
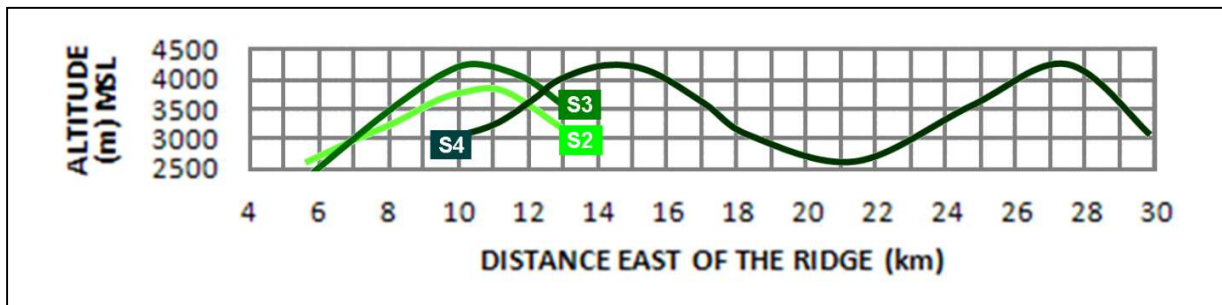
Figure 3.47: 308 K Isopleth comparisons.

According to Barry (1981) such an increase in wavelength with time is the result of an increase in the windward side surface temperature, which reduces the lapse rate. This in turn reduces the Scorer parameter.   According to Equation 2.5 in Section 2.5.3, a reduction in the Scorer parameter (denominator) will increase the wavelength. The SAWS weather stations all show a drop in temperature having taken place by the time of the release of S4. In spite of this drop in surface temperature, it seems that the increase in temperature up to the maximum was sufficient to still have afforded an increase in the wavelength during the day. Evidence of an increase in the wavelength was found by calculating the Scorer parameter for a depth of atmosphere from the summit to 700 hPa from the lee side data. This data is displayed in Table 3.3. The S4 wavelength is calculated to have increased by 33.5% from that of the S2 wavelength. From the isopleths analysis in Figures 3.19 and 3.46 an increase in wavelength of 32% was determined which is in very good agreement with these calculations. A similar comparison with S3 data failed as a result of the slower increase in θ, highlighted in orange in Table 3.3.

Table 3.3: Lee side Scorer and wavelength calculations.

	SUMMIT m MSL	700hPa m MSL	SUMMIT WIND	700hPa WIND	θ SUMMIT	θ 700hPa	l km^{-1}	Λ km
S2	2253	3115	8.6	22.2	303.11	304.31	0.435359	14.43802
S3	2250	3115	18.4	21.3	304.33	304.47	0.115036	54.64132
S4	2251	3117	18.3	22.6	302.56	303.75	0.326021	19.28009

Another comparison between the lee waves is shown in Figure 3.48, together with some prominent positions of the S1 balloon. The blue line represents the line along the Hex River mountain ridge used for calculations. For S1 the point where it crossed the ridge is indicated by S1-R while S1-F shows the area where S1 experienced a flattening in its profile curve. An analysis of the vertical velocity profile of S1 (see Appendix B, Figure B.2) shows that the flattening in the S1 profile curve is associated with downdrafts. Thus downdraft areas existed between the Mountain ridge and the S2 launch position prior to the start of the S2 launch.

The advancing of the S2, S3 and S4 wave crests progressively further from the ridge line are indicated by S2-C, S3-C and S4-C respectively.
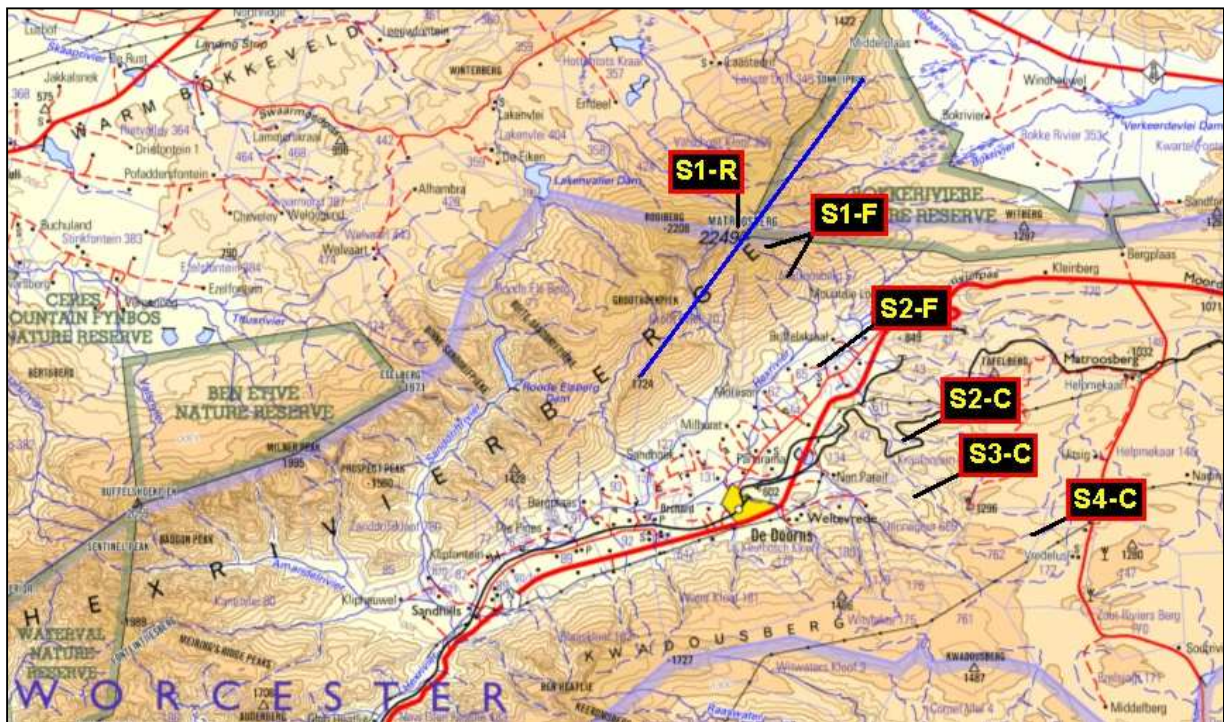
Source: Chief Directorate Surveys and Mapping (2006)

Figure 3.48: Selected positions in the profile curves and θ curves.

3.11 Aircraft observations

One report from a pilot was received about mountain wave turbulence encountered near Beaufort West on 22 July 2010 (Barker 2010, pers com). This area is too far from the study area for the observed conditions to represent conditions in the lee of the Hex River Mountains, but proves that the synoptic conditions were such that almost the entire Western Cape Province was affected by mountain wave turbulence.

3.12 Overview of 22 July 2010

The data from S1 could successfully be used to determine which wavelengths could be trapped in the lee of the Hex River Mountains. S2 and S3 were launched from the same site, but followed two different trajectories through the atmosphere. S2 showed strong evidence of a

rotor due to reversed flow. From fluctuations in ascent rate and vertical velocity, observed below summit level, this rotor could be identifies as a type 1 rotor. A type 1 rotor was also observed in the S3 data at approximately the same distance from the mountain as the S2 rotor. The S3 rotor showed smaller magnitudes of ascent rate and vertical velocity fluctuations as well as shorter horizontal distances in reversed flow compared to the S2 data. The type rotor observed in the S4 data was associated with larger reversed flow, as well as larger updraft velocity and fluctuations ascent rate than was the case in S2 and S3 data. Both S3 and S4 showed evidence of loss of altitude in the main wave.

The chapter that follows covers the data collected on the second day of the first field trip. It also contains summaries of the two days.

CHAPTER 4: FIELD WORK 23 JULY 2010

4.1   Surface conditions (NCEP reanalysis)

Figure 4.1 shows the position of the sea level pressure isobars for 06:00 GMT and 18:00 GMT on 23 July 2010. At 06:00 GMT the cold front passed through Cape Town and advanced to a position south east of Port Elizabeth by 18:00 GMT. To the west of the cold front the 1024 hPa isobar also advanced from about 7°E at 06:00 GMT to beyond 30°E by 18:00 GMT. Assuming geostrophic balance, wind directions parallel to the isobars estimate the surface wind direction (Lankford 2000). This direction is indicated by green arrows, showing a backing of the 06:00 GMT south westerly wind to south easterly at 18:00 GMT over the study area.
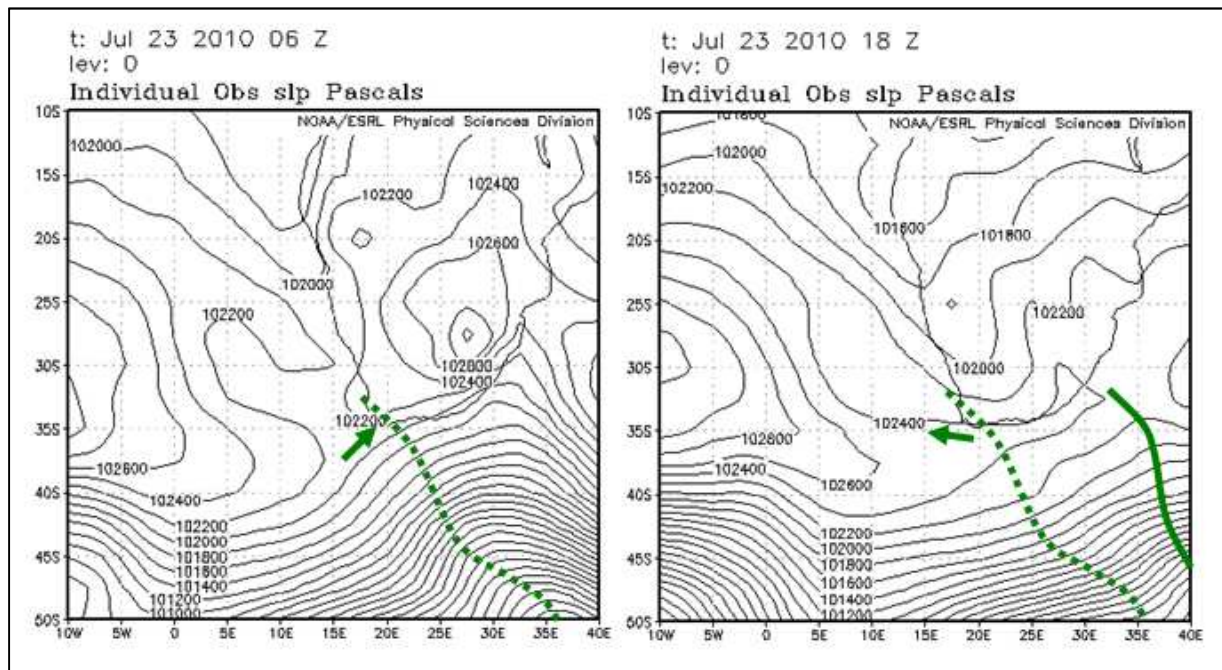
Source: NCEP Reanalysis (2011)

Figure 4.1: Sea level pressure for 06:00 and 18:00 GMT on 23 July 2010.

4.2   Upper air conditions (NCEP reanalysis)

The 850 and 500hPa geopotential height lines for 23 July 2010 are shown in Figure 4.2 with trough lines shown as dotted lines for the 06:00 GMT period and as solid lines for the 18:00 GMT period, with blue representing data at 850 and red data at 500 hPa levels. The bottom

images in Figure 4.2 clearly show that the trough lines at both geopotential levels had advanced eastward. A further degeneration of the westward tilt of the trough lines is observed from that shown in Figure 3.2 (22 July data).   It is clear that the cyclonic system has weakened substantially from 22 to 23 July. At 850 hPa the winds parallel to the geopotential height lines were westerly throughout the day with the wind direction at 500 hPa maintaining a north westerly direction.
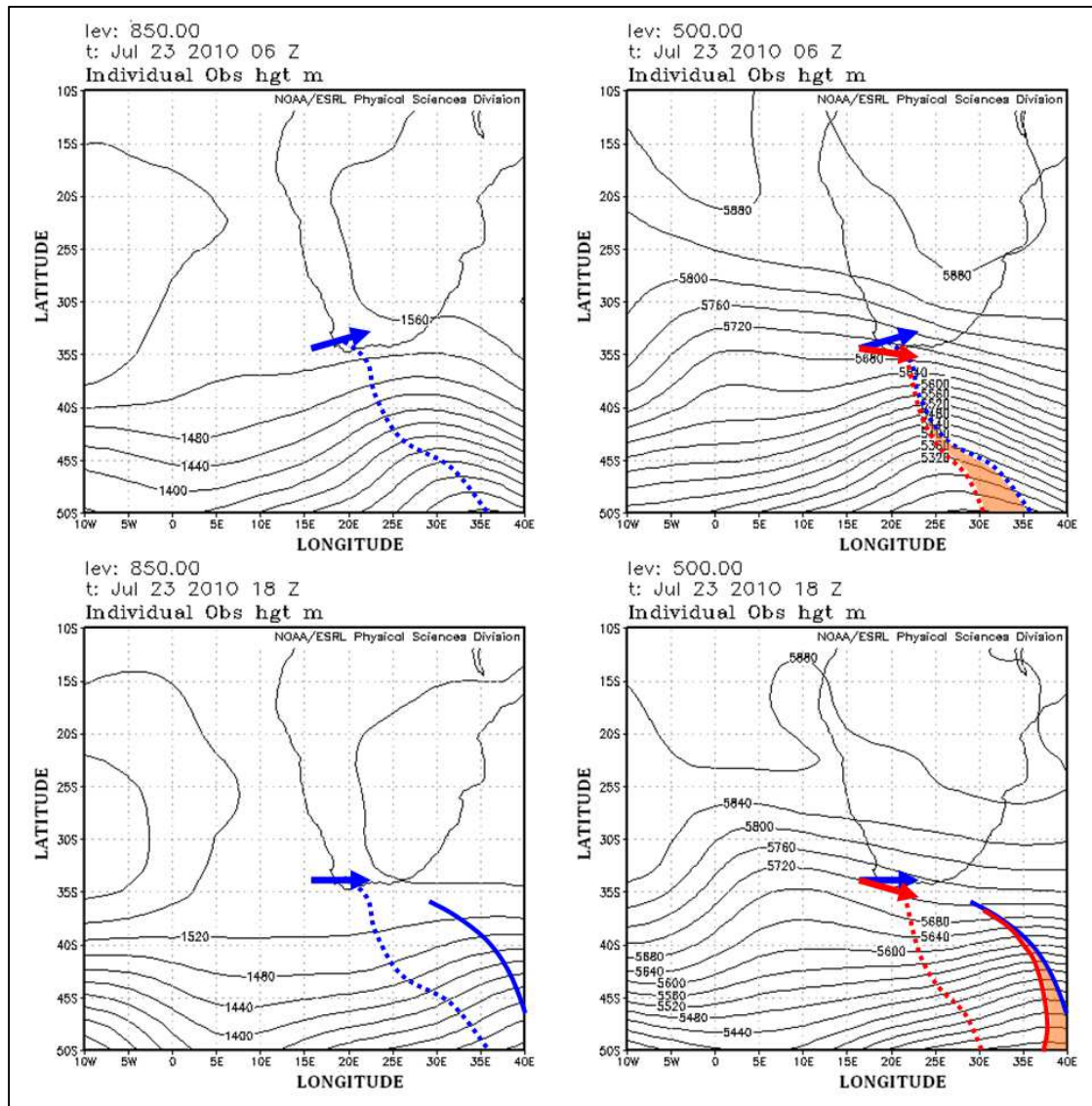
Source: NCEP Reanalysis (2011)

Figure 4.2: 850, 700 and 500hPa geopotential height lines for 06:00 (top) and 18:00 GMT (bottom).

4.3 Upper air conditions (S5 data)

Figure 4.3 shows the upwind wind speed and direction as calculated by the upwind balloon, S5 (see Figure 4.6), on 23 July 2010. Wind direction for the entire sounding lay outside of the yellow area which indicates the favourable range for near-perpendicular winds. Therefore the wind direction at first did not appear to be favourable for the development of mountain waves (see S4.7.1 comment). Wind speed increased steadily with height. The summit level wind speed at 2249 m above MSL was approximately 14 ms^{-1} thus sufficiently strong for the development of mountain waves for 1000 m high barriers and just short of the 15 ms^{-1} requirement for 4000 m barriers (Barry 1981). There is good agreement between the NCEP wind directions and that measured by the S5 balloon.
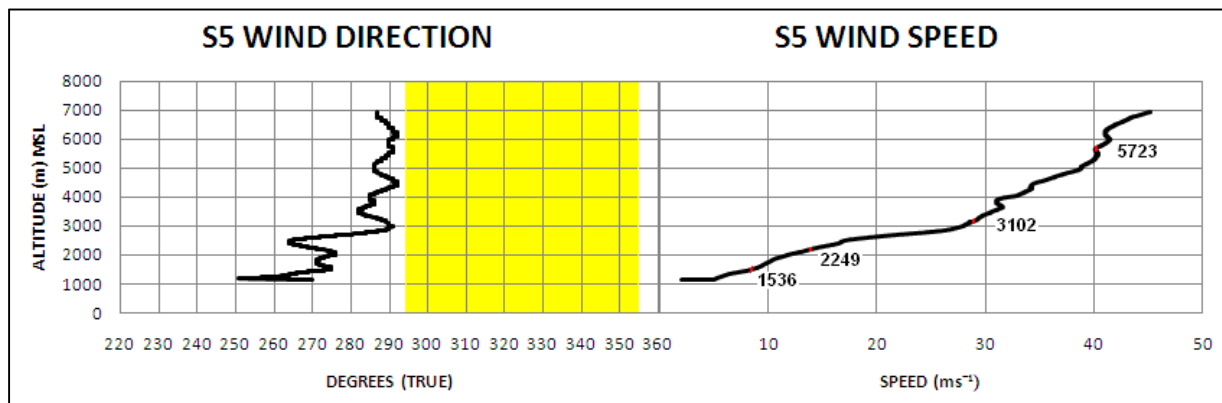
Figure 4.3: S5 wind direction and speed.

4.4 Surface conditions (SAWS data)

The surface wind direction for the three upwind stations is summarised in Figure 4.4. Both Wellington and Excelsior failed to maintain a near-perpendicular direction to the Hex River Mountain orientation (yellow area). Only Porterville showed signs of near-perpendicular wind direction, but this may be the result of channelling between Piketberg and the Olifantsrivierberge. Further evidence in support of channelling was the oscillation between NW and NE at this location. Excelsior showed a near constant WSW flow, which again may have been the result of channelling. The wind direction for these three stations did not show a clear

concentration in the near perpendicular belt as was the case during the 12:00 – 16:00 GMT period of the previous day (see Figure 3.4).
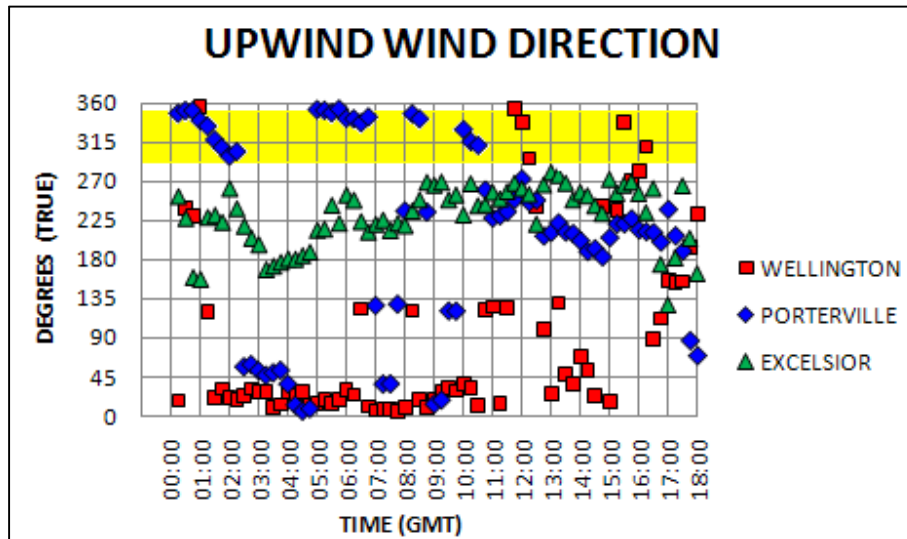
Figure 4.4: Upwind wind direction on 23 July 2010.

The temperature graphs of the upwind stations as well as Worcester are shown in Figure 4.5 for part of 23 July 2010. In comparison to the graphs of the previous day (see Figure 3.5) a significant drop in surface temperature from 22 to 23 July is observed. The 12:00 GMT maximum temperatures measurements dropped by 8.0 to 10.8 °C for each station. The temperatures seem to indicate the passage of a cold front (Lankford 2000). In support of this are the upper air temperature drops of 11.3 and 3.3 °C at 850 and 700 hPa from the first to second upwind sounding. The surface temperatures all increased up to at least 10:00 GMT.

The half-hourly aviation weather observations (METARs) from Cape Town International Airport also reveal the passage of the cold front. During the entire 22 July the surface winds were prefrontal north westerly winds. Cloud reached the airport at 15:00 GMT. By 19:00 GMT the first rain had fallen, still during northwest winds. At 06:00 GMT on 23 July the cold front passed through Cape Town with the wind rapidly backing from NW to SSE (Smit 2011, pers com). The data shows the ridging of the high pressure behind the cold front starting between 08:00 and 09:00 GMT.
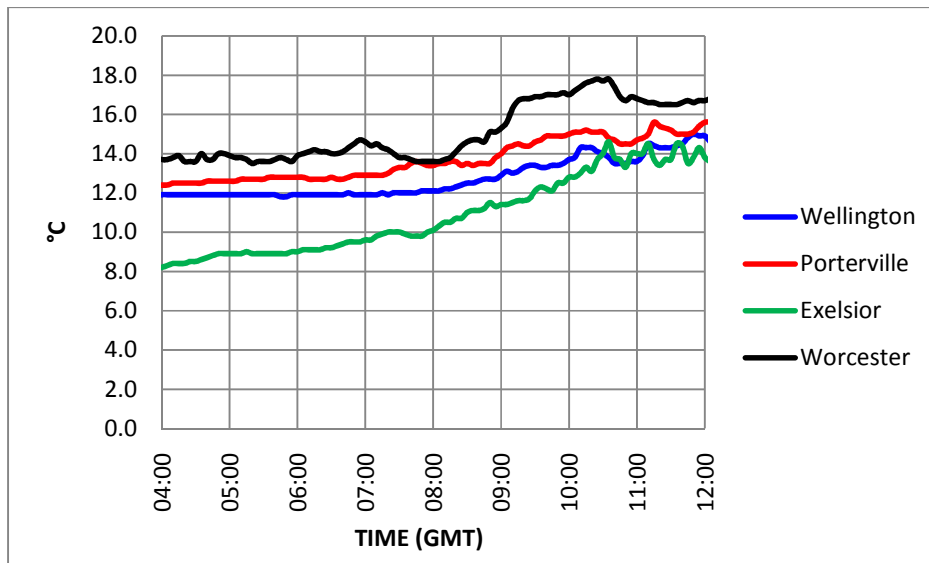
Figure 4.5: Upwind surface temperature on 23 July 2010.

4.5   Surface conditions (onsite)

During the launch of the S5 balloon, the weather upwind from the Hex River Mountains was completely overcast with light rain and cloud bases down to 800 ft above ground level (AGL). Surface wind direction was observed to be westerly. The lee side of the mountain had cloud spilling over the Hex River Mountains. During the performing of the lee side soundings, a gap in the cloud cover was observed over the central parts of the valley with cloud forming further downwind against the mountainous terrain east and south east of De Doorns.

The westerly surface flow was indicative of post frontal conditions. It was therefore expected that the depth of near perpendicular upwind flow was much diminished, with conditions no longer favouring the development of trapped lee waves. The lee side gap in cloud was expected to be due to downdrafts in the wave system where the wave had dropped below the condensation level.

4.6 Sounding locations and objectives

Four soundings, S5 - S8, were performed on 23 July 2010. The locations are indicated in Figure 4.6. Blue boxes indicate positions of flattening in the upwind soundings. S5 served the same purpose as S1 and was launched from the same site upwind of the Hex River Mountains. The initial raw data from S4 viewed during the field work, showed more evidence of reversed flow and downdrafts than was the case with S2 and S3. S6 was launched from the same site as S4 in order to see whether similar data to that of S4 could be obtained. S7 and S8 were both launched further downwind from the mountain in order to measure features further away from the mountains.
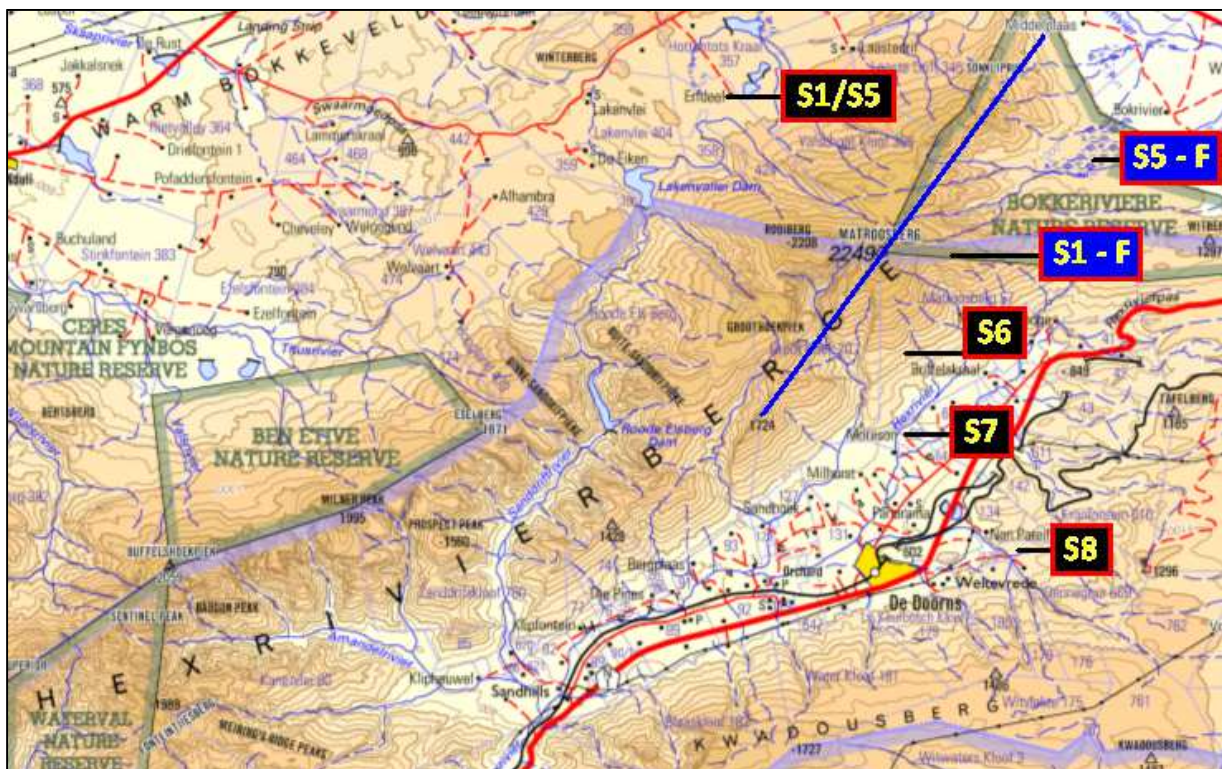
Source: Chief Directorate Surveys and Mapping (2006)

Figure 4.6: The location of launch sites for S5, S6, S7 and S8.

Details of the sounding times and locations are shown in Table 4.1.

Table 4.1: Launch site data for S5-S8.

SOUNDING	LATITUDE	LONGITUDE	ALTITUDE	TIME OF RELEASE
	degrees	Degrees	m MSL	GMT
S5	33.33096	19.61135	1167	05:19
S6	33.41161	19.69926	668	07:12
S7	33.43929	19.67829	503	08:44
S8	33.46637	19.70609	562	09:40

4.7   Sounding 5

4.7.1   S5 Profile

The sounding profiles for S1 and S5 are shown in Figure 4.7. The S1 profile (red line) shows a clear decrease in the gradient of the curve at the 7 km mark east of the launch site. The S5 curve (black) shows only a very slight decrease in gradient in the profile between the 10 and 14 km marks.
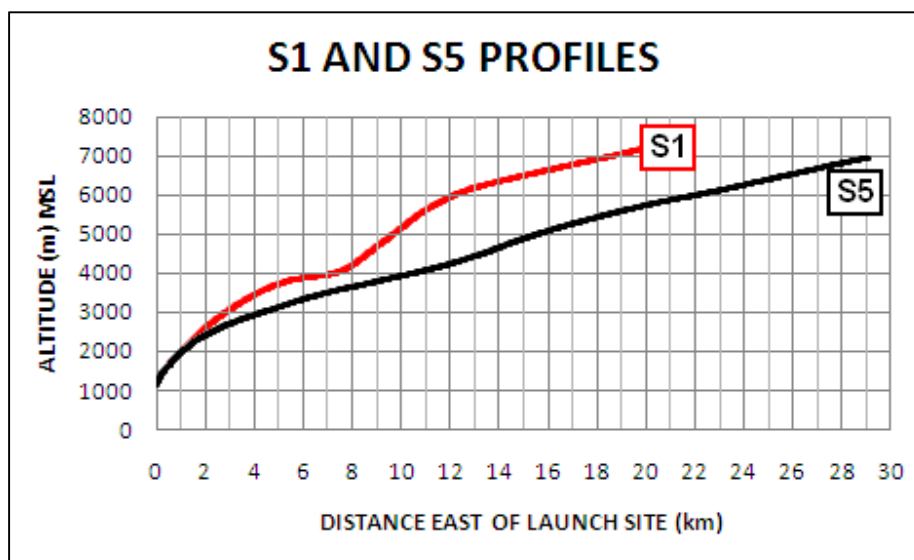
Figure 4.7: S1 and S5 profiles.

In Figure 4.6 S1-F and S5-F show the position of the midpoints in these drops in gradient of the profile curves for S1 and S5 respectively, with S1-F clearly closer to the blue ridge line (approximately half the distance that S5-F).

4.7.2   S5 Potential temperature

The potential temperature (θ) graphs for S1 and S5 are shown in respectively red and black in Figure 4.8.   The S1 curve shows prominent vertical or horizontal sections.   Vertical areas represent areas of constant θ through large depths of the atmosphere (2300-3600 m) while vertical areas represent constant altitude for a variety of θ values (e.g. 305 – 310 K). In contrast the S5 curve is a lot smoother and shows much smaller parts of the graph being vertical or horizontal.   The general trend for S5 is an increase in θ with height, indicating a stable atmosphere according to Doyle & Durran (2007), Holton (1992) and Stull (1991). The stability of the upwind atmosphere of S5 was thus favourable for the development of mountain waves (Atkinson 1981).
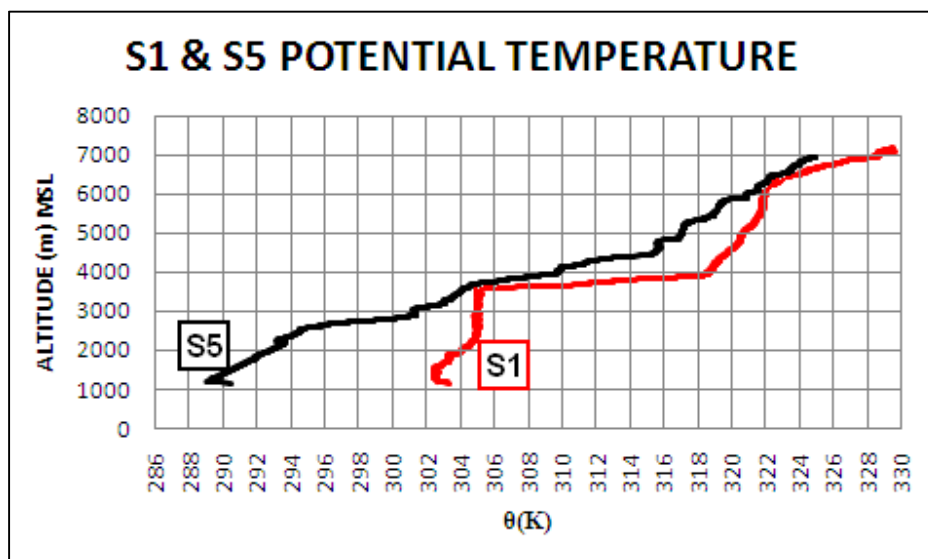
Figure 4.8: S1 and S5 potential temperature.

4.7.3   S5 Scorer parameter

The S5 balloon crossed the Hex River Mountain Ridge line at an altitude of approximately 3200 m above MSL. The assumption is again made that at this altitude and above, the atmospheric conditions on the lee and upwind sides were approximately the same. Figure 4.9 shows the Scorer parameters of S1 (red) and S5 (black) with respectively transparent red and grey lines joining adjacent values. Both the curves show an overall drop in the Scorer parameter with height, with the S5 values being generally higher than the S1 values. An increase in Scorer values for S5 to about 1.75 km^{-2} occurred at 2700-2800 m, making the 2800 m level a maximum amplitude level for trapped lee waves (Lindsay 1962). This was significantly lower than the similar peak for the S1 data at 3700 m. At these two levels the corresponding θ graphs of Figure 4.8 were horizontal showing large increases in θ and stability (Doyle & Durran 2007).
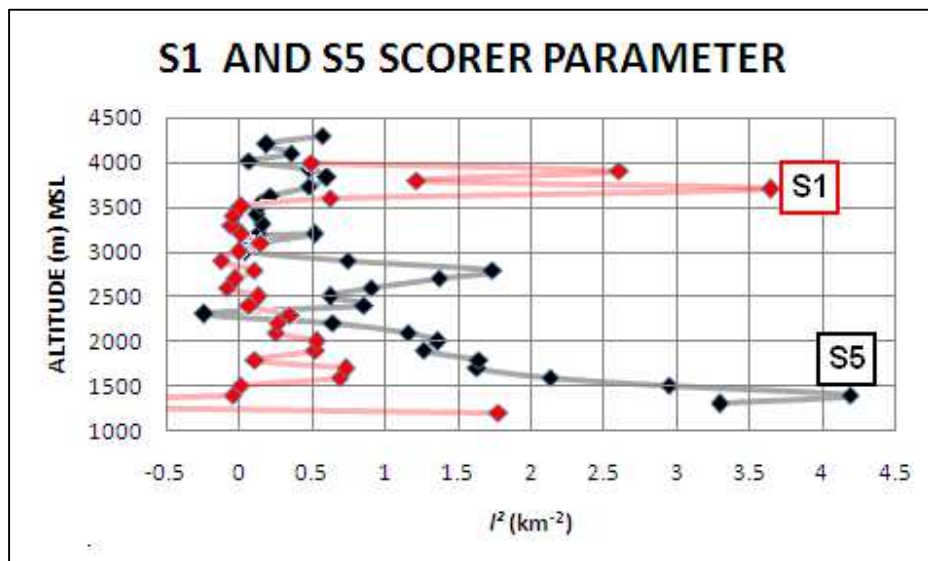
Figure 4.9: Scorer parameters of S1 and S5.

Figure 4.10 shows the two layers and average Scorer values (l^2) used to substitute into Equation 2.4 to test for the existence of trapped lee waves. The result is $1.164861 > 0.76154$, which satisfied the necessary condition for the development of trapped lee waves (Durran 2003) despite the fact that the upwind wind direction fell just outside the near-perpendicular direction needed for wave formation.
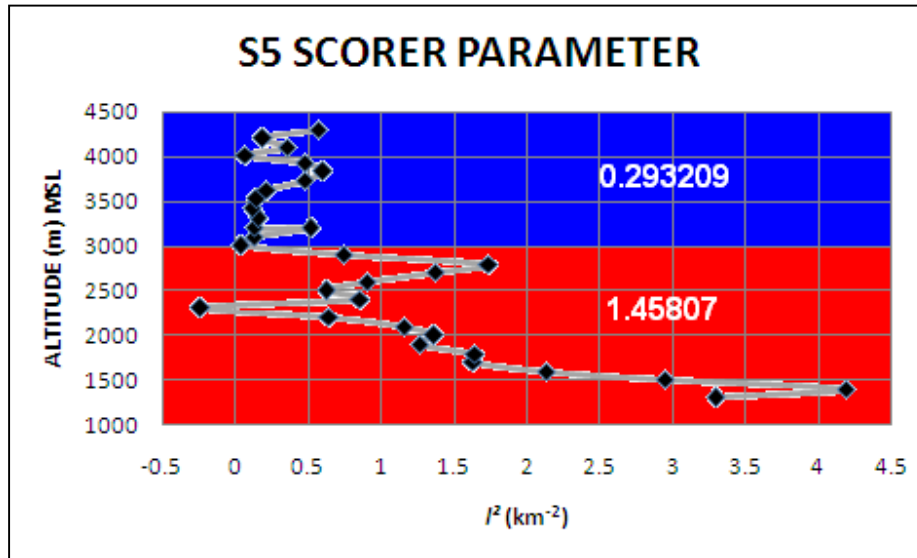
Figure 4.10: S5 data used to test for wave trapping

Using Equation 2.19 and the average scorer parameter below 4000 m above MSL, it can be shown that $a = 3.78 \ll 6.257$ indicating that trapped lee waves are likely to develop (Koch *et al.* 2006).

4.7.4   Lee wavelength

Figure 4.11 shows the area defined to test which wavelengths were likely to be trapped on the lee side of the Hex River Mountains. Using the same methodology described in Section 3.10 the square roots of *a*, *b*, *c* and *d* in Figure 4.11 were substituted into Equation 2.5. The result proved that all wavelengths between 4.77 and 34.9 km could be trapped in the altitude range of 2700 - 3000 m and wavelengths between 8.1 and 24.4 km could be trapped in the 3700 - 4000 m range.
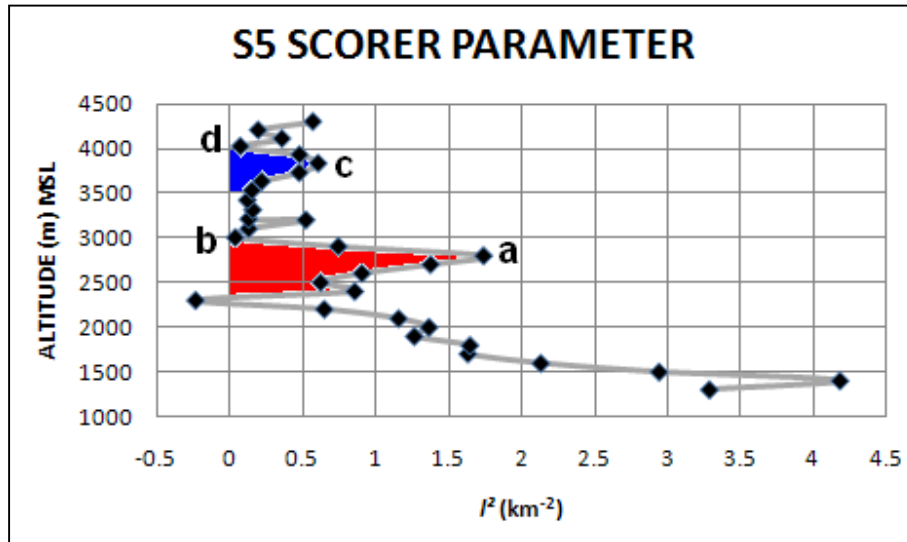
Figure 4.11: S5 Scorer parameter areas used to determine wavelengths for trapping.

4.8 Sounding 6 (S6)

4.8.1 S6 Profile and track

S6 was conducted from the S4 launch site. Figure 4.12 compares the profiles of S4 and S6 in red and black respectively. The S6 curve shows no prominent local maximum or minimum as was the case with S4. The curves are reproduced for altitudes below 2200 m above MSL in Figure 4.13. It shows larger distances of reversed flow for S4 (about 135 m westwards) than for S6 (about 65 m westwards). This reversed flow could not have been the result of synoptic scale flow. This is explained in section 4.9.1 as S7 experienced larger reversed flow. Another feature of the comparison is the fact that the S4 curve attains an altitude of 1440 m above MSL during the reversed flow, while S6 attained 1000 m above MSL.
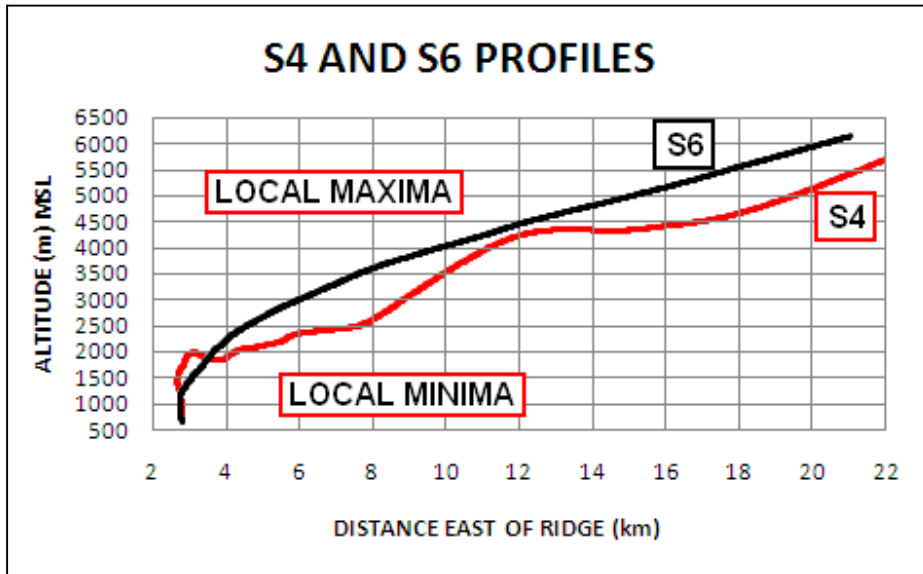
Figure 4.12: S4 and S6 Profiles.
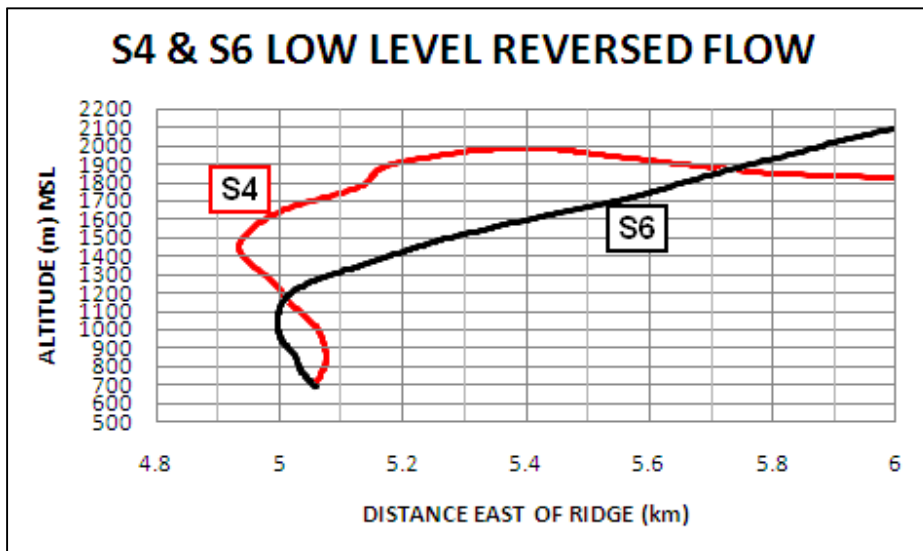
Figure 4.13: S4 and S6 Profiles below 2200 m.

4.8.2   S6 Richardson Number (Ri)

Figure 4.14 shows the S6 Ri values for 300 m vertical intervals. Of the 18 data points three were discarded as spikes. The data shows all Ri values were positive, indicating a stable atmosphere according to Holton (1992). All the values of S6 exceeded the 0.25 critical value, thus S6 was unable to sustain turbulence within a stable environment as mentioned by Huschke (1959), Gossard & Hooke (1975), Holton (1992) and Chan (2008).
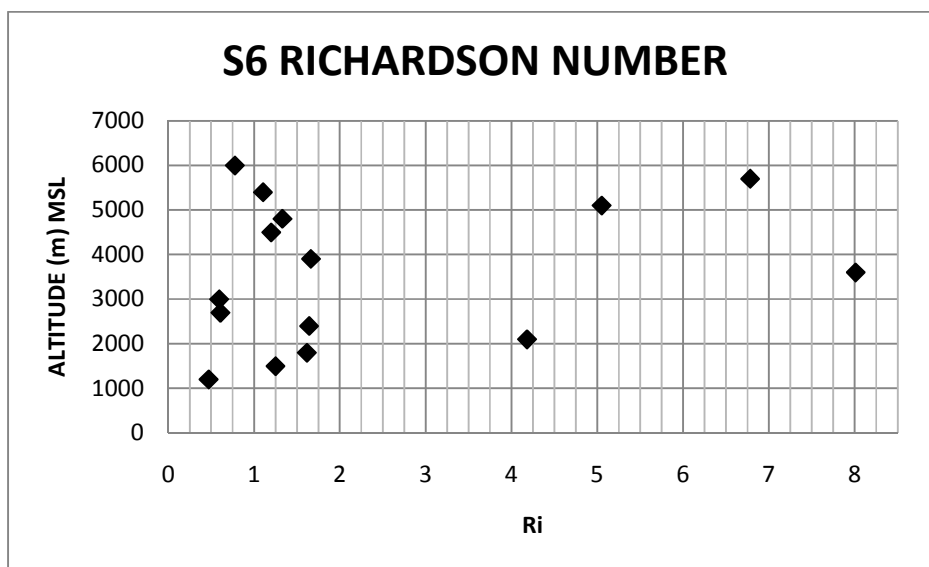
Figure 4.14: S6 Richardson Number

4.8.3   S6 Horizontal Vorticity (η)

The η values for S6 shown in Figure 4.15 are predominantly positive. Negative η values are indicated in blue, but are insignificant.
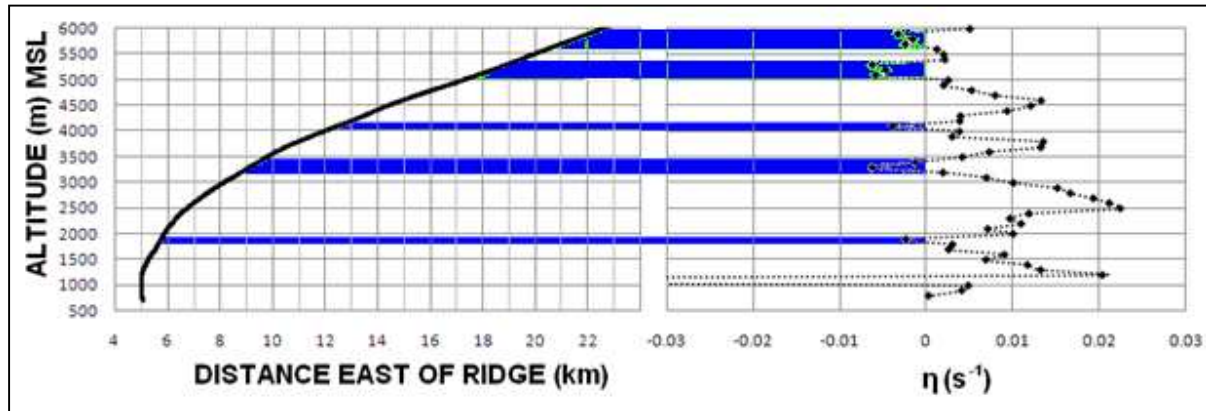
Figure 4.15: Comparison between S6 Profile and y-component horizontal vorticity.

4.8.4   S6 Balloon ascent rate

Figure 4.16 shows the ascent rate graph for S6 for 50 m vertical intervals. Beyond the 7 km mark there are three peaks in the graph. The space between the first two peaks is approximately 6.3 km, while the second space is approximately 6.2 km. According to Shutts, Healy & Mobbs (1994), the wavelength can then be estimated to be between 6.2 and 6.3 km long. A 1.8 ms^{-1} increase in ascent rate data is observed between five and six kilometres east of the ridge, thus in the same general area where such a phenomenon was observed in the S2 and S3 data.
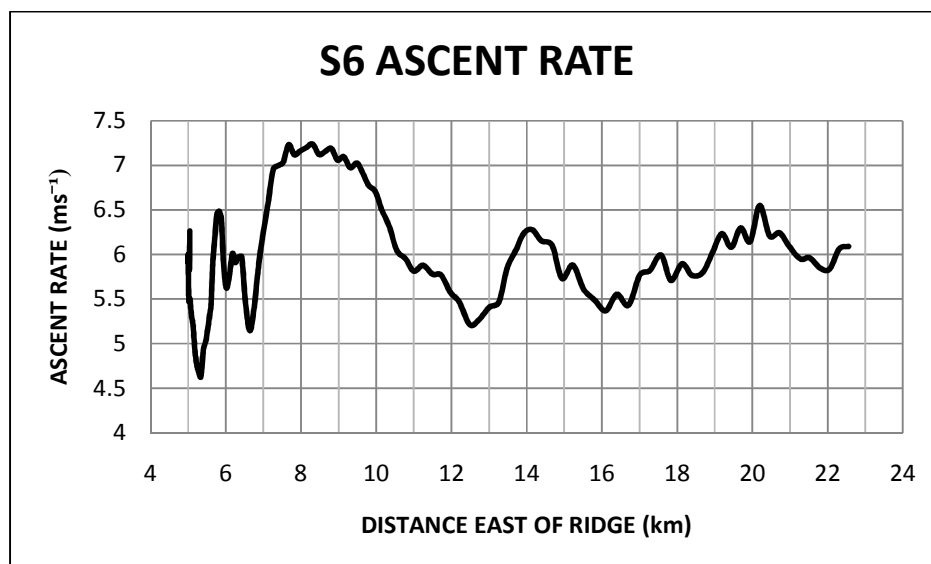
Figure 4.16: S6 Ascent Rate

4.8.5   S6 Vertical velocity

In Figure 4.17 the vertical velocity is plotted for the reversed flow period. The first value in the top right hand corner is a computational spike. Red represents the reversed flow data. The reversed flow is associated with an increase of 0.169 ms^{-1} in vertical velocity with a maximum updraft speed of 0.039 ms^{-1}. The reversed flow was 60 m along a westerly vector.
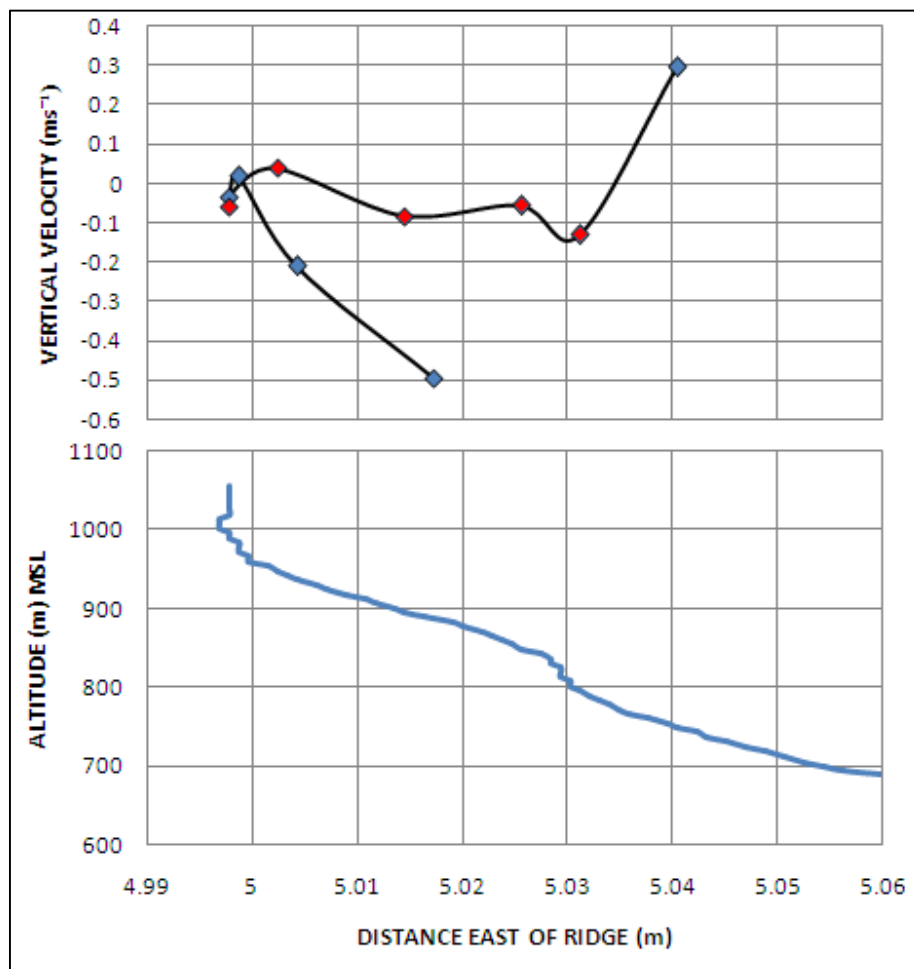
Figure 4.17: S6 vertical velocity and reversed flow

The S6 vertical velocity curve together with the profile curve is shown in Figure 4.18. The downdraft areas are highlighted in green. As was the case with S2, no drop in the profile curve was observed. The downdrafts, although frequently encountered were not strong enough to

create dips in the profile curve as was also the case with S2. Compared to the -4 ms^{-1} maximum downdrafts of S2, S6 experienced a maximum downdraft of less than -1.5 ms[-1.] The effect of this is evidenced in the profile curve in Figure 4.18 which shows only very slight flattening in the green areas as opposed to the S2 data in Figure 3.19. Both the reversed flow and increase in ascent rate (and subsequently vertical velocity) is indicative of a type 1 rotor (Hertenstein & Keuttner 2005).
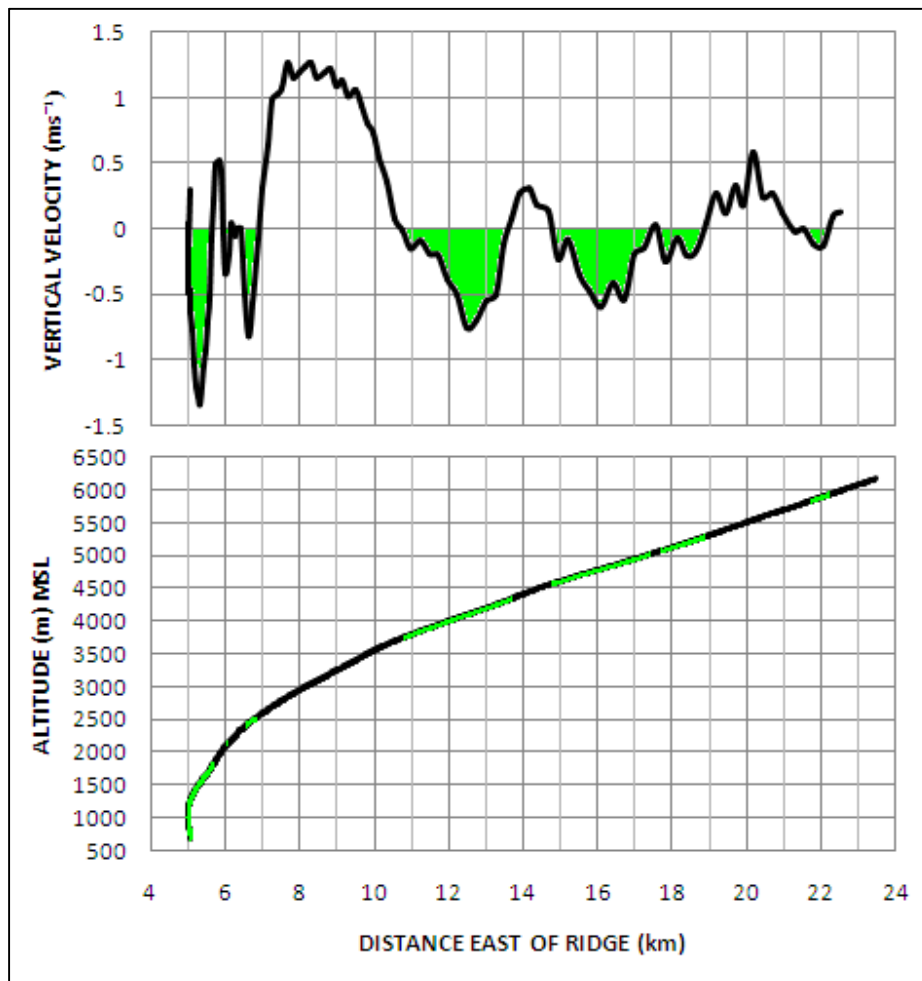
Figure 4.18: S6 vertical velocity

4.8.6   S6 Potential temperature and isopleth estimation

In Figure 4.19 it is observed that θ starts at the surface at much lower values than what was the case for the previous day. This is due to the large drop in surface temperature that was

experienced – the temperature dropped 10°C from the start of S4 to the start of S6. The S6 θ curve shows no evidence of the large low level areas of constant θ observed the previous day. Instead the curve rises gradually at approximately a constant rate. A few areas are observed where the θ values remain constant for small vertical depths of around 200 m. No areas of significant fluctuation within small vertical distances are observed.
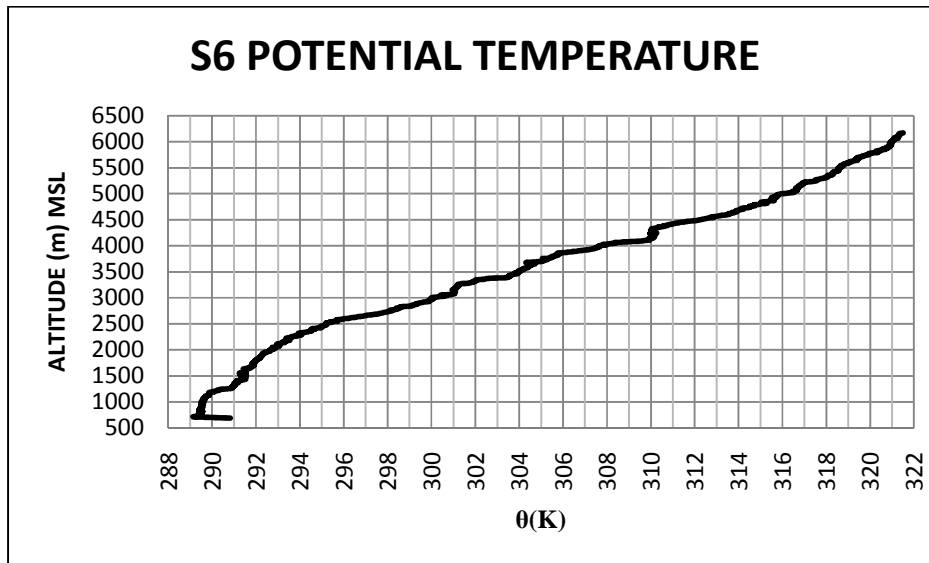
Figure 4.19: S6 Potential Temperature

In Figure 4.20 the θ values between the dotted blue lines show a drop in value with increased height, which according to Doyle & Durran (2007), Holton (1992) and Stull (1991) indicate areas of instability. This drop of 0.28 K is smaller than those experienced from the lee soundings of 22 July and occurred over a vertical depth of about 30 m compared to depths of 100 – 150 m in the case of S2 and S3. Thus the 22 July soundings showed more prominent unstable areas than what was measured by S6.
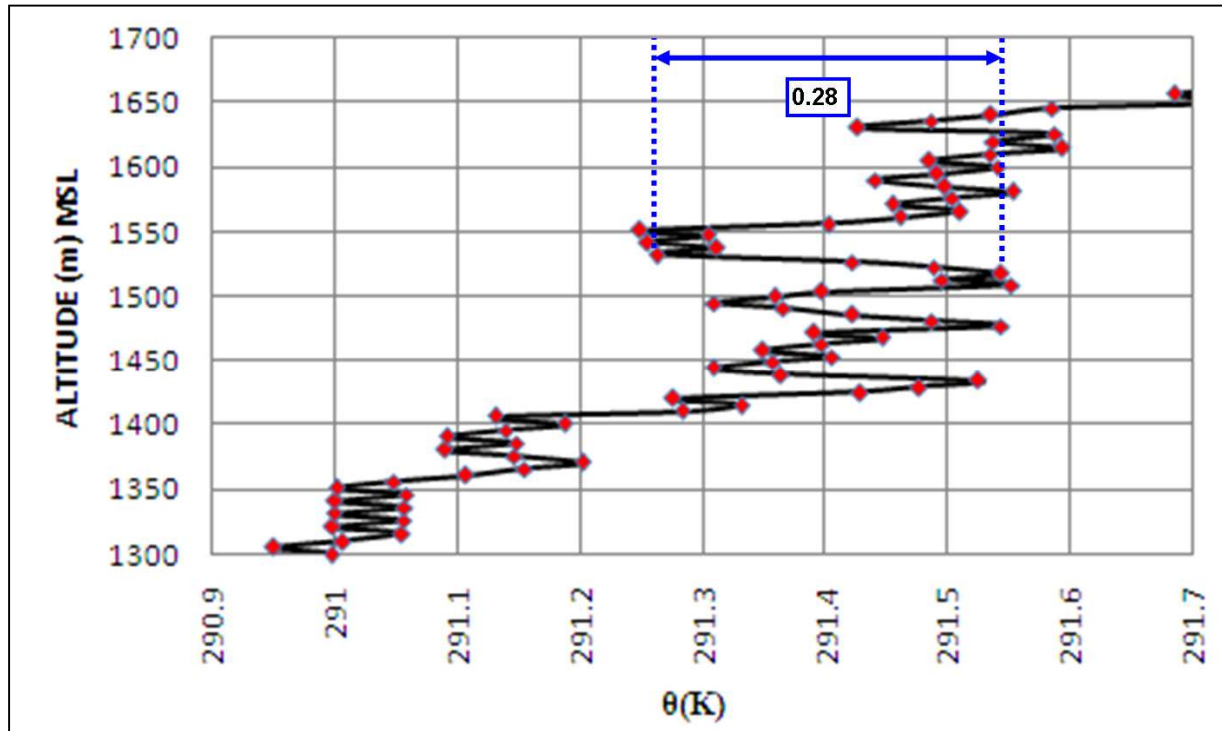
Figure 4.20: S6 Stability areas using Potential Temperature

The isopleths analysis for S6 is shown in Figure 4.21. The 310 K isopleth coincided with the profile curve (black curve) for a longer distance than other isopleths. It thus served as a good reference in the isopleths estimation. The position of the 310 K isopleth suggested that the primary wave position was not near the vertical red dashed line, which is the position where the first prominent downdraft started (see Figure 4.18). The vertical blue dashed line shows the position where the maximum downdraft speed occurred. It seemed to predict the wave crest position better than the red dashed line. Overall the interpolation of isopleths was far more cumbersome than the cases of S2 - S4. The positions of the 289.5, 301 and 310 K isopleths were used to interpolate the positions of the other isopleths in the analysis.
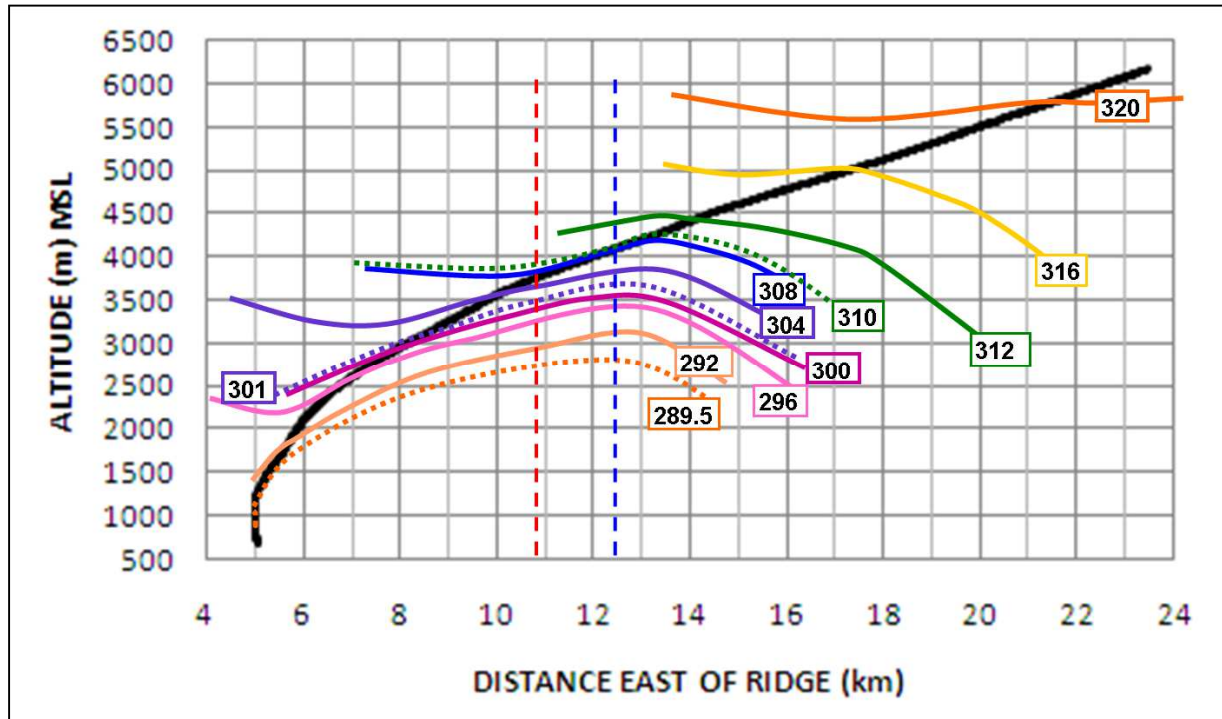
Figure 4.21: S6 Isopleth estimation

4.9   Sounding 7 (S7)

4.9.1   S7 Profile

The S7 profile curve, shown in Figure 4.22, reveals flow upstream towards the Hex River Mountains at altitudes below 1300 m above MSL. This flow continued for 110 m along a westerly vector. The synoptic scale wind data in the area (Figure 4.4) shows a strong bias towards westerly flow. There is thus no evidence of synoptic scale forcing of air from the east which could have resulted in the balloon moving towards the mountain. Decreases in the gradient of the curve are not very prominent. There are no drops in altitude in the curve.
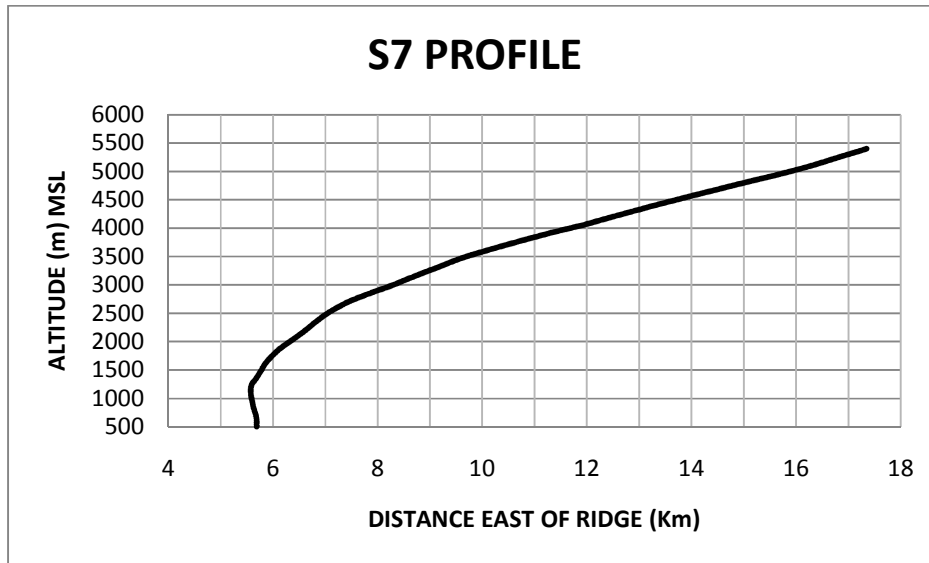
Figure 4.22: S7 Profile

4.9.2   S7 Richardson number (Ri)

The Richardson numbers for 300 m vertical intervals are shown in Figure 4.23. The data is predominantly positive, proving that the atmosphere is stable (Holton 1992). There is no clustering of data to indicate a trend within the data nor is there clustering of data points below the 0.25 critical value, which would prove support for turbulence within the stable atmosphere (Chan 2008, Gossard & Hooke 1975, Holton 1992 and Huschke 1959).
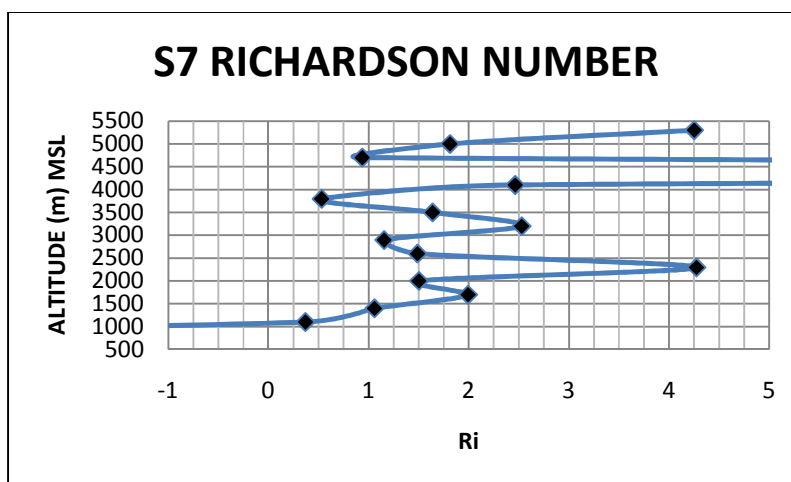
Figure 4.23: The S7 Richardson number

4.9.3   S7 Horizontal vorticity (η)

Figure 4.24 indicates that S7 mostly experienced positive η in Figure 4.24. Like the 22 July data, the larger negative values (green) coincide with a slight (15.3-17.3 km mark) drop in the gradient of the profile curve. This green area may be related to a trough area in the main mountain wave (Doyle & Durran 2007; Hertenstein & Kuettner 2005).
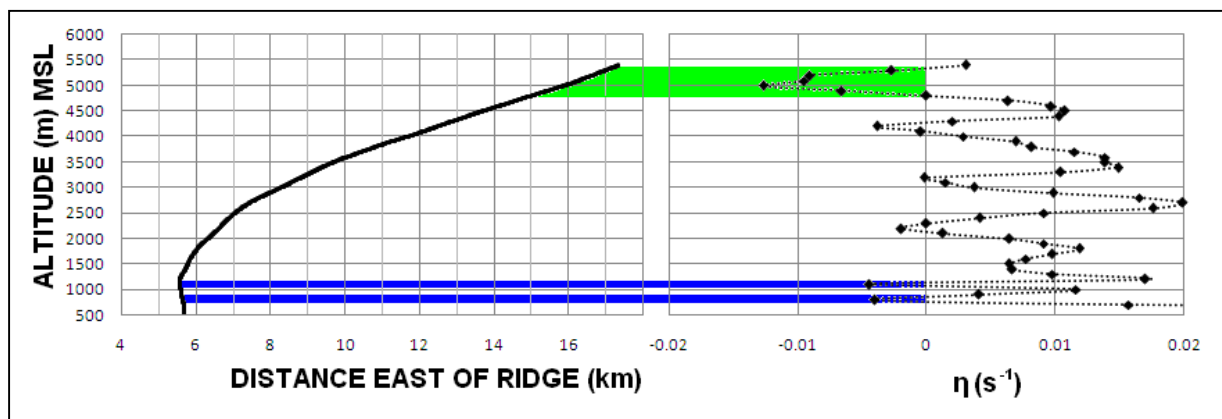
Figure 4.24: Comparison between S7 Profile and y-component horizontal vorticity

4.9.4   S7 Ascent Rate

The ascent rate graph for S7 for 50 m vertical intervals is shown in Figure 4.25. Between the 6 and 15 km marks, three peaks are observed with the distance between the first two approximately 3.2 km and that between the last two about 4.4 km. This translated to a wavelength of 3.2 – 4.4 km according to Shutts, Healy & Mobbs (1994), which is significantly shorter than the estimated 6.2 - 6.3 km of S6. However, a difference between the second and third peaks is observed. At the 8.3 km mark the curve rises above the blue line (6.2 ms^{-1}) to the second peak and then falls back to the blue line at the 11.2 km mark. The flow pattern around the third peak behaves differently. The graph rises from 6.2 ms^{-1} at the start of the red line (11.3 km) and after the peak is reached, does not drop to this same level. Instead it follows the gradient of the red line after the 15.3 km mark. This may indicate that the third peak is merely a small perturbation along the curve towards a more prominent peak at the 17.3 km mark. If this is indeed the case, then the

wavelength could be 7.6 km (17.3 – 9.7 km). This will mean an increase in wavelength slightly later in the day from the S6 period. According to Barry (1981) it is typical of mountain waves to show an increase in wavelength later in the day as the near surface temperature increases. Variation in ascent rate is mostly in the order of 1 ms^{-1} except for east of the 15.5 km mark where it increases to 2 ms^{-1}.
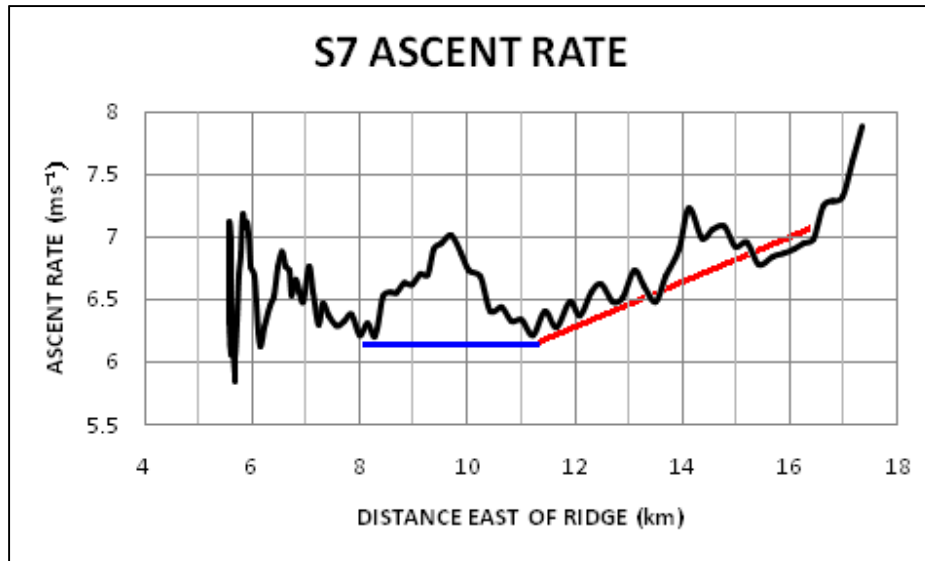
Figure 4.25:   S7 Ascent Rate.

4.9.5   S7 Vertical Velocity

For the vertical velocity calculations a 6.6 ms^{-1} average ascent rate was deducted from one second values (D-Met data). This method of Grubišić & Billings (2007) produced the curves in Figure 4.26 and 4.27. Figure 4.26 shows the vertical velocity points during the reversed flow period of S7 as red points and the associated parts of the profile curve as a red curve. A vertical velocity increase of 1.2 ms^{-1} was experienced during the reversed flow with a maximum velocity of 0.52 ms^{-1} reached. The balloon moved 110 m westwards. The fluctuation in vertical velocity occurred below the summit level and is thus indicative of a type 1 rotor (Hertenstein & Keuttner 2005).
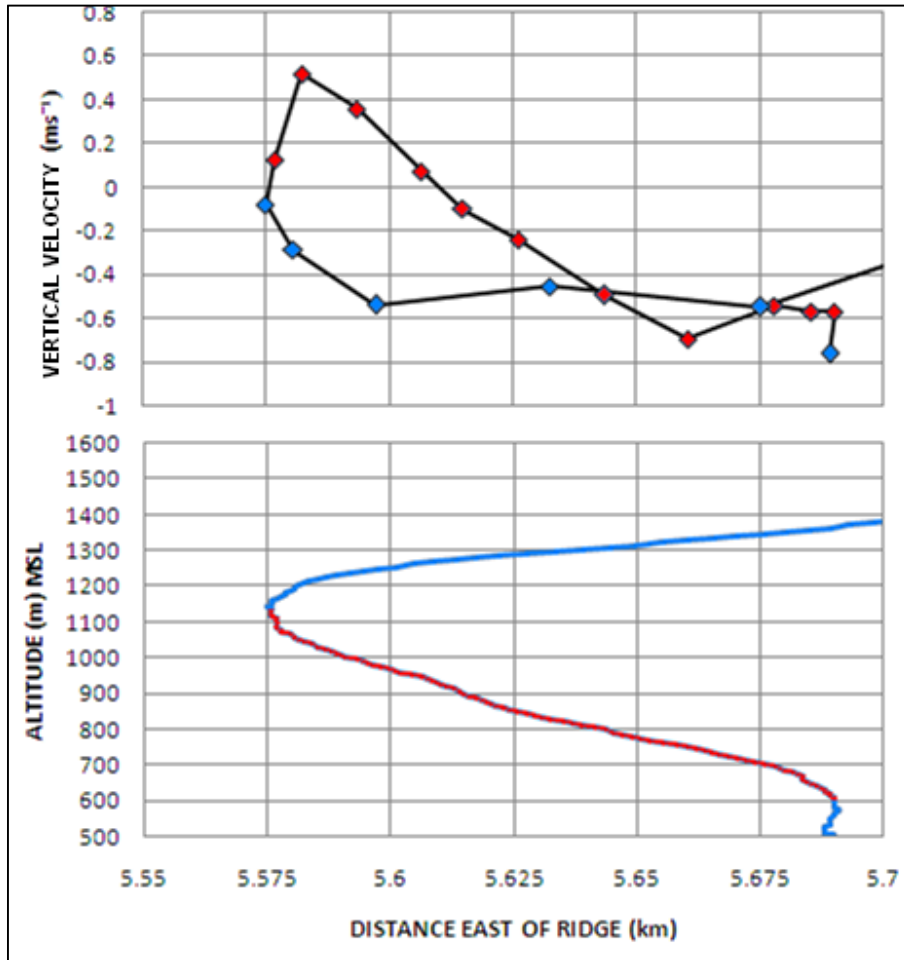
Figure 4.26:   S7 Vertical velocity associated with reversed flow.

Green areas in Figure 4.27 show downdrafts corresponding to areas in the profile curve. When similar images from S2 and S4 data are compared (Figures 3.16 and 3.38), it is observed that the low level reversed flow of S2 and S4 coincided with increased vertical velocity. In the case of the reversed flow of S7, a downdraft was experienced. This was also the case with S6, where Figure 4.17 confirmed slight reversed flow. Downdrafts observed in the S7 data are very weak, but do correspond with areas in the profile curve where the gradient of the curve decreased (areas A and B).
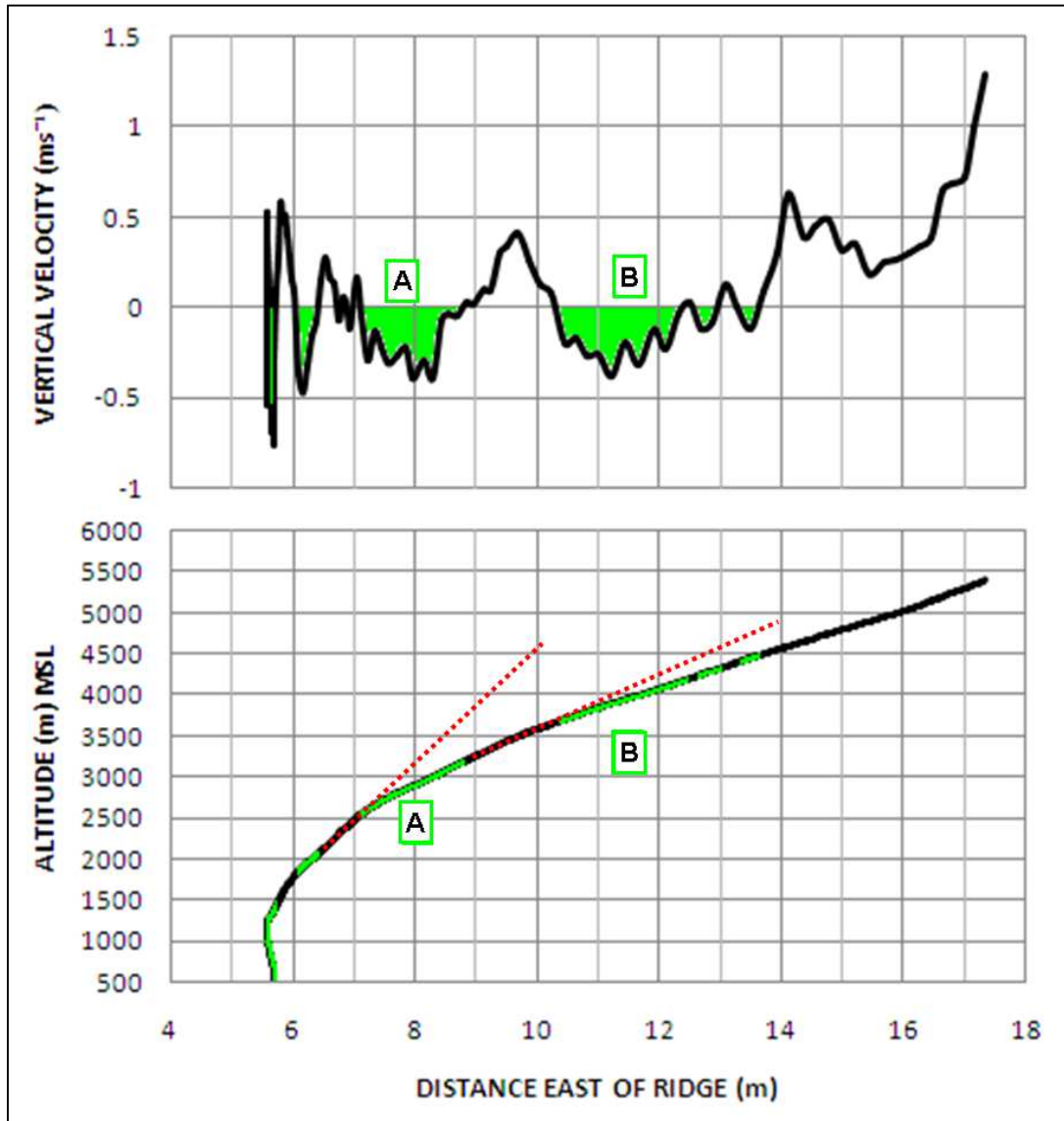
Figure 4.27:   S7 Vertical Velocity.

4.9.6   S7 Potential Temperature (θ) and Isopleths estimation.

The S7 θ graph is shown in Figure 4.28. It resembles the graph of S6 very well, although the drops in θ values were approximately 0.2 K.
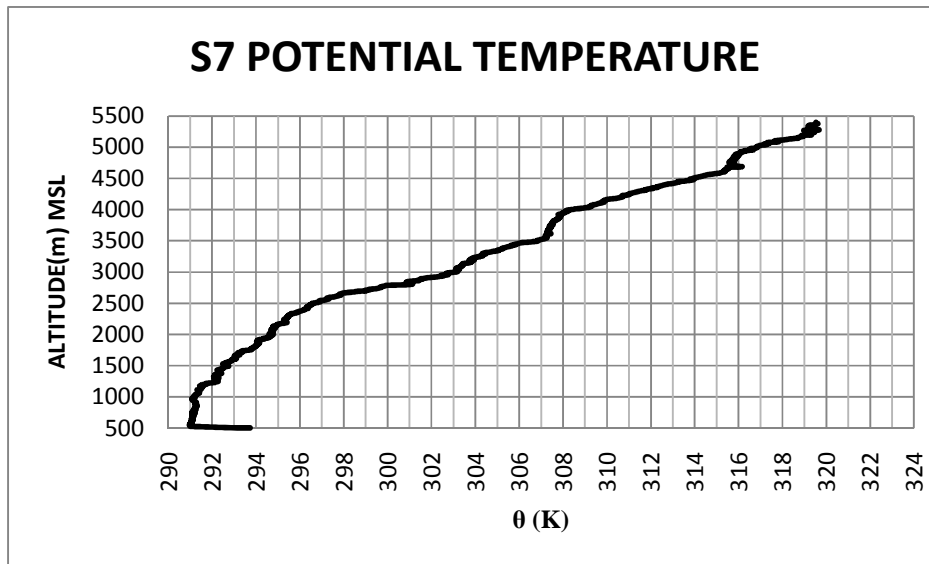
Figure 4.28: S7 Potential Temperature.

The θ graph below 1500 m above MSL is reproduced in Figure 4.29, showing three areas of instability (blue, green and orange) due to drops in θ values (Doyle & Durran 2007). They range between 0.22 and 0.25 K and are smaller in magnitude to that found in S6, while occurring more frequently than for the S6 case.
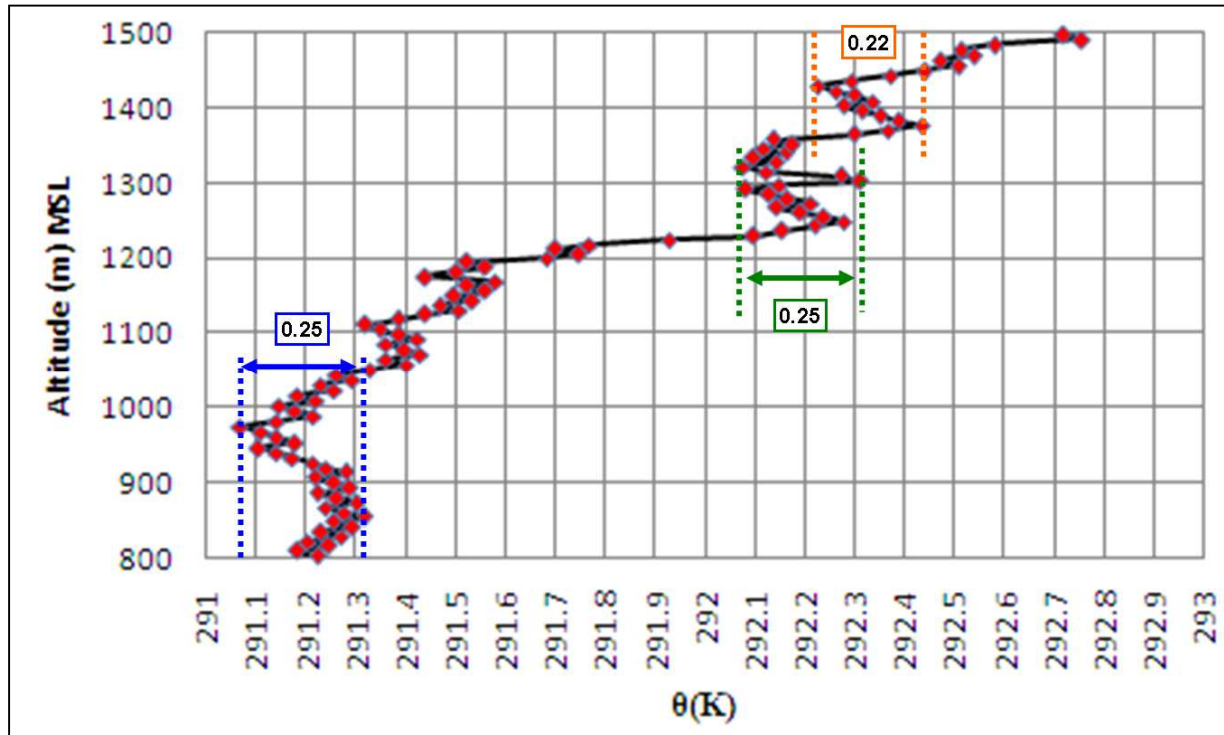
Figure 4.29: S7 Instability areas according to potential temperature.

The S7 isopleth analysis is shown in Figure 4.30. The 291, 294, 308 and 316 K isopleths served to guide the interpolation of the rest of the isopleths. This lead to a wave crest position estimated to lie near the 11 km mark. The overall shape of the wave system is supported by the maximum updraft positions (light blue arrows) and the maximum downdrafts positions (red arrows). The wavelength of 4.4 km as predicted by the method of Shutts, Healy & Mobbs (1996) from Section 4.9.4, fits the estimated wave system perfectly (blue and purple dashed lines). The dashed blue line further coincides with a position in Figure 4.27 where a maximum downdraft occurred. The position where this same downdraft commences in Figure 4.27 is indicated as a dashed red line in Figure 4.30. Thus as was the case with S6, maximum downdraft speed positions better predicted wave crests than positions where the downdraft started.
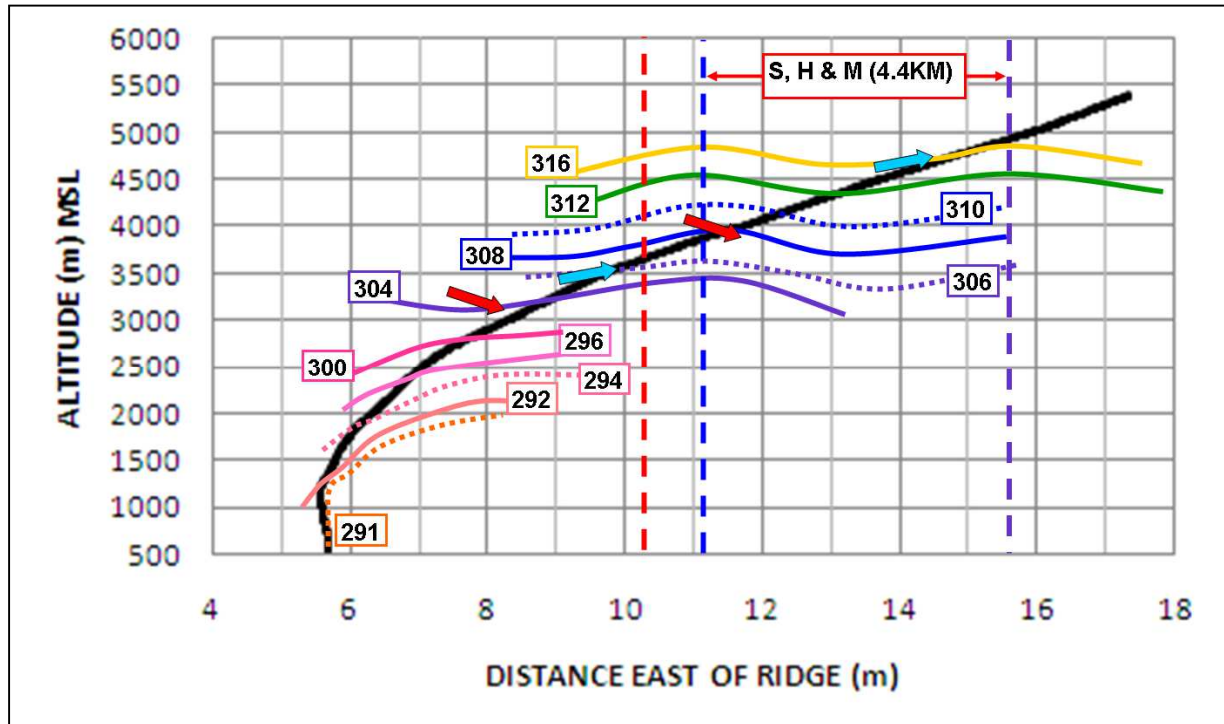
Figure 4.30: S7 Isopleth estimation

4.10   Sounding 8 (S8)

4.10.1 S8 Profile

The sounding profile of S8 in Figure 4.31 shows a general convex shape (black curve). Red dashed lines show how the gradient of the curve continues to drop with distance east of the ridge. No reversed flow was observed. This may be due to the distance away from the mountain as the S7 reversed flow was detected about 5.6 km from the ridge, with S8 launched near 13km from the ridge.
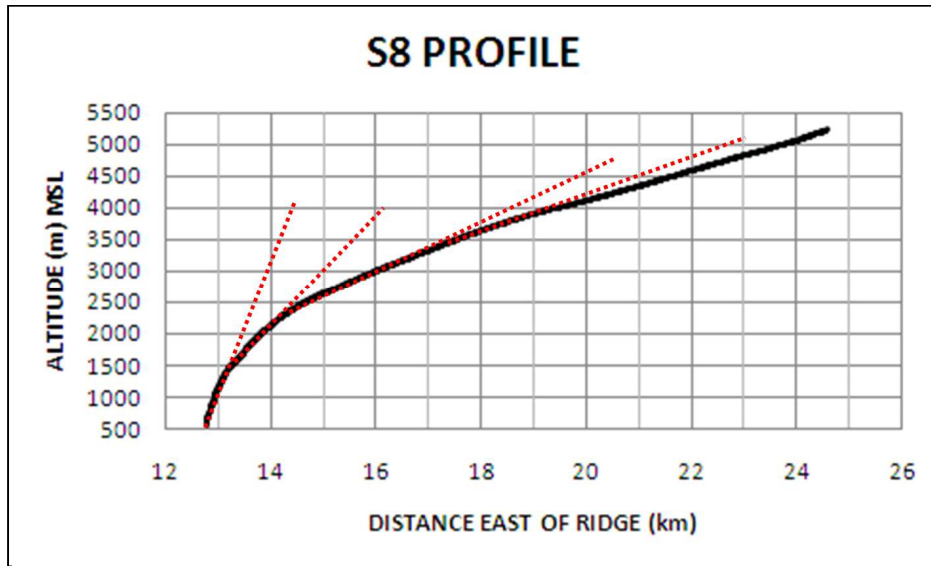
Figure 4.31: S8 Profile

4.10.2 S8 Richardson Number (Ri)

The S8 Ri values are shown in Figure 4.32 for 300 m intervals. All the Ri values above the altitude of 1100 m are positive, indicating a stable atmosphere according to Holton (1992). The values further exceed the critical value of 0.25, indicating that the lee atmosphere will be unable to support turbulence (Chan 2008, Gossard & Hooke 1975, Holton 1992 and Huschke 1959).
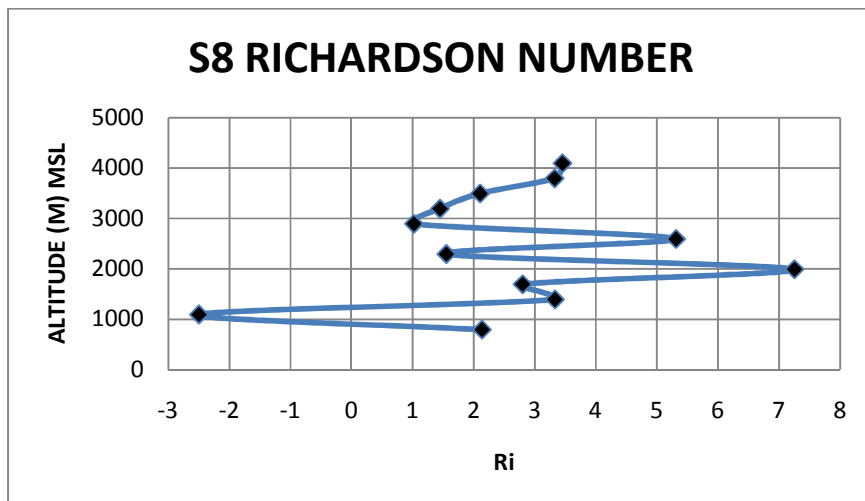
Figure 4.32: S8 Richardson Number

4.10.3 S8 Horizontal vorticity (η)

Figure 4.33 indicates that the η values resemble those detected for S7. Values of η are predominantly positive with very weak negative values (Green and blue areas).
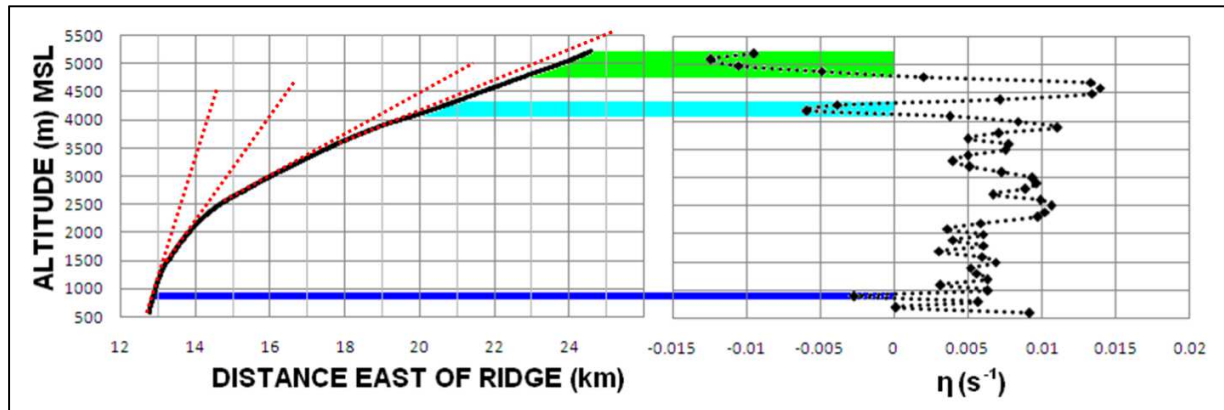
Figure 4.33: Comparison between S8 Profile and y-component horizontal vorticity

4.10.4 S8 Ascent Rate

The ascent rate curve for S8 in Figure 4.34 shows two peaks beyond the 14 km mark. The first peak is observed at the 17 km mark east of the ridge. From the experience with S7, the second peak is observed at 24.2 km, while the minor peak at 22.5 km was taken as a local perturbation rather than a major peak. The result is a wavelength of 7.2 km according to Shutts, Healy & Mobbs (1994).
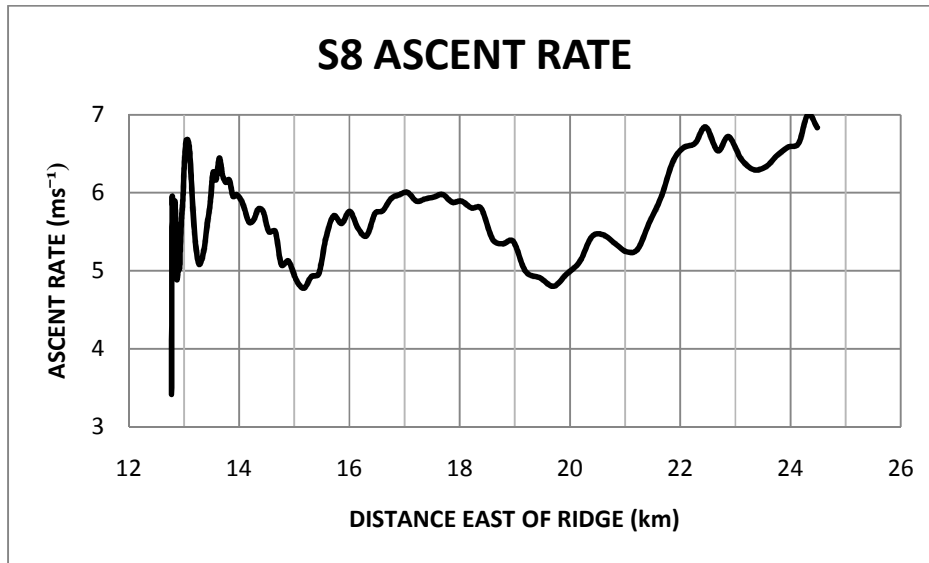
Figure 4.34: S8 Ascent Rate

4.10.5 S8 Vertical Velocity

A D-Met average ascent rate of 5.75 ms^{-1} was used to calculate the vertical velocity curve in Figure 4.35 from the method of Grubišić & Billings (2007). Ignoring the initial spike in the data, the green downdraft areas show downdraft speeds reaching 1 ms^{-1} while the downdrafts of S6 and S7 reached 0.75 and 0.5 ms^{-1} respectively. No reversed flow is observed for S8. Once again the downdraft areas correspond to areas of slight concavity (about the 15.5 and 20 km marks).
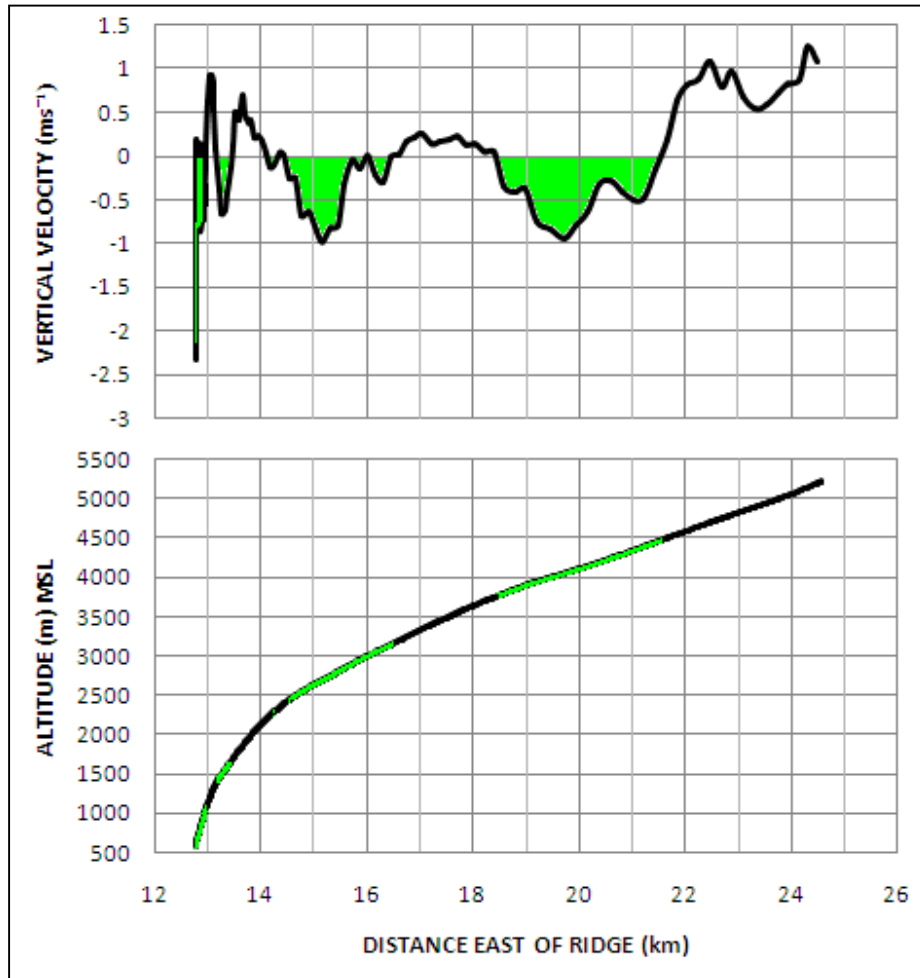
Figure 4.35: S8 Vertical Velocity

4.10.6 S8 Potential Temperature (θ) and Isopleth Estimation

The S8 θ graph in Figure 4.36 compares well with the θ graphs of S6 and S7. Drops in θ values were less than 0.2 K, hence instabilities are comparable to those of S6 and S7.
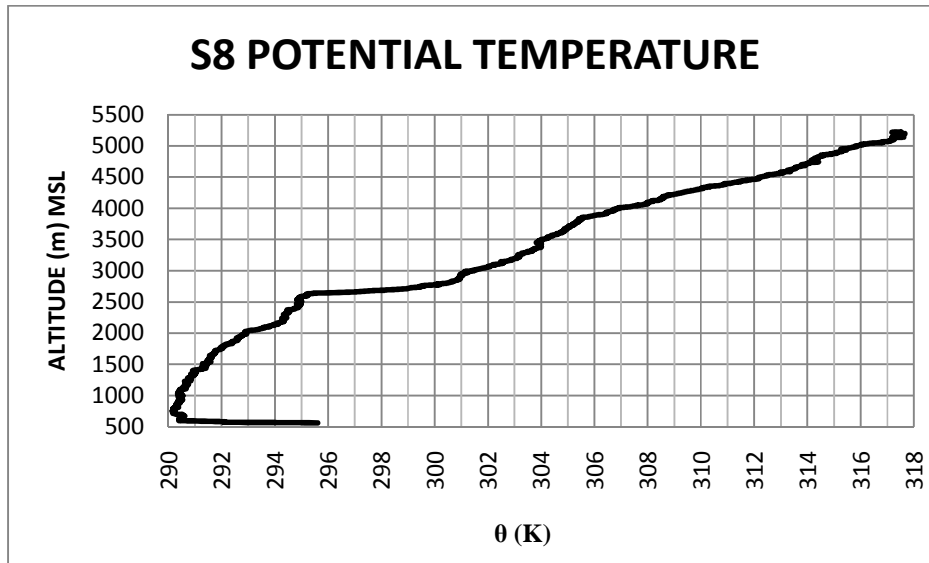
Figure 4.36: S8 Potential Temperature

With the aid of the 290.5 and 295 K isopleths, the 292, 296, 300 and 304 K isopleths positions could be predicted. Maximal downdraft (red arrow) and updraft (light blue arrow) positions further support the placing of the 304 K isopleth, which indicated a likely wave trough near the 18 km mark (red dashed line). Using the method of Shutts, Healy & Mobbs (1994), a second wave crest may have been situated at the 11.2 km mark (left hand side red dashed line). This position aided in predicting the shape of the isopleths.

The blue dashed line marked the maximum downdraft position. Thus in the case of S8 the start of the downdraft (right hand side red dashed line) is a better estimator of this position, as was the case with S2, S3 and S4. Of the 23 July soundings S8 experienced the strongest downdrafts (-1 ms^{-1}). It would appear that for S6 and S7 for downdraft magnitudes close to -0.5 ms^{-1}, the maximum downdraft positions rather than the start of downdraft areas, better estimate wave crests positions. It also seems likely that -1 ms^{-1} can serve as the critical downdraft speed which can predict the position of a wave crest. At such a speed (and higher negative values), the S2, S3, S4 and S8 balloons showed good agreement between wave crest position and the position where the downdraft started.
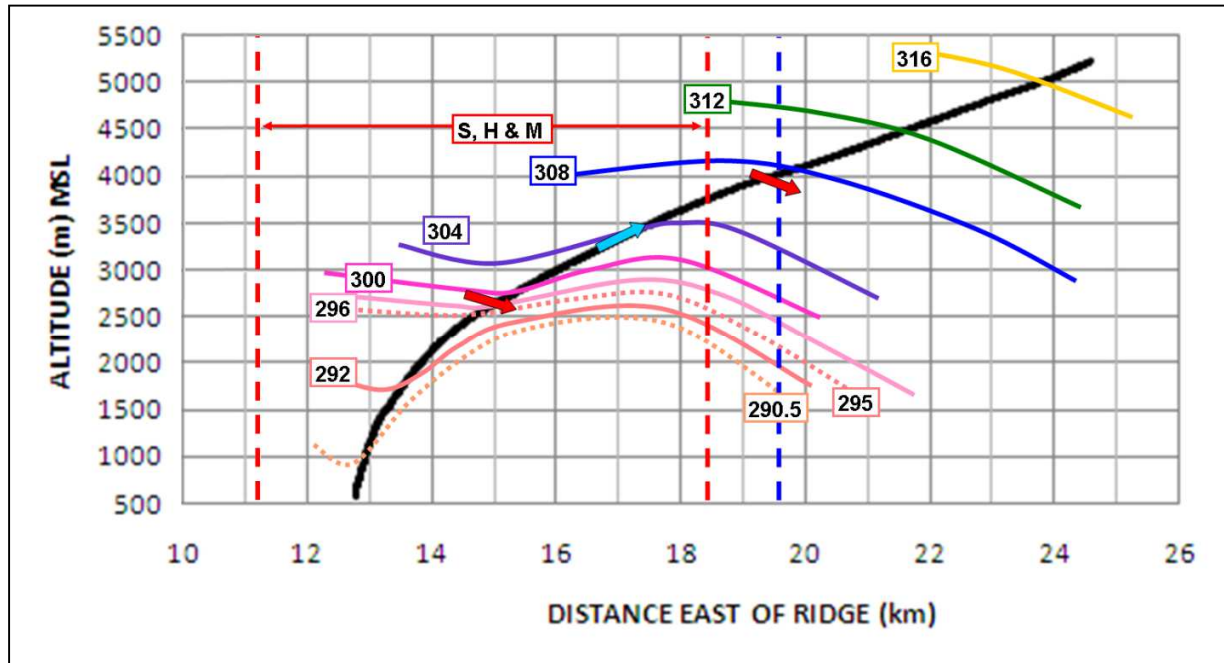
Figure 4.37: S8 Isopleth estimation

4.11   Field work summary for 22 and 23 July 2010

4.11.1 Synoptic conditions and observations

The prefrontal weather of 22 July 2010 resulted in stronger mountain wave features being detected than on 23 July when the surface front had passed. The synoptic analysis showed a marked increase in tilt of trough lines with height. This is evidenced in the increase of approximately 47% in the wind speed at the 700 and 500 hPa levels from S1 to S5. The sub-summit wind speed decreased to between 69 and 88%. The most significant observed wind feature was the lack of near-perpendicular wind direction observed after the passage of the front.

Surface temperature data showed a marked increase in temperature during the prefrontal period with evidence of adiabatic warming on the lee side during the morning (S3 time frame). This coincided with an increase in wavelength and stronger mountain wave features later in the day (S4 data).

4.11.2 Main mountain wave features

Table 4.2 summarizes the lee wave data from the 22/23 July soundings. Data is highlighted according to the classification of mountain waves (Table 1.1) used in JSP. Data falling within the categories of weak, moderate or strong are highlighted with respectively green, yellow and red. Two wavelength (λ) estimates are tabled: those according to ascent rate (Shutts, Healy & Mobbs 1994) and those using the start or midpoints of downdrafts. Variations in the isopleth estimations were performed conservatively by only considering isopleths which followed the profile curve through deep layers of the atmosphere. This was performed for all the soundings.

Table 4.2 clearly shows the degeneration of wave activity from 22 to 23 July. On 22 July S2 and S3 showed features of mainly moderate waves according to the JSP classification, while S4 showed predominantly strong wave features. The -7 ms^{-1} downdraft was 2 ms^{-1} short of the -9 ms^{-1} requirement for strong waves. It must be remembered that the JSP was conducted in the lee of the Sierra Nevada Mountains, thus the JSP classification is based on very different topography and air masses than the Western Cape. Lindemann, Heise & Herold (2001) further classify updrafts of 4 ms^{-1} as moderate to strong. Classifications like these are thus subjective and one would not be able to say for certain that the S4 data proved strong mountain wave activity.

Table 4.2: Mountain wave features relevant to the classification used by JSP

DATE	SOUNDING	MAX U/D DRAFT m/s	λ S, H & M km	λ DOWNDRAFTS km	MAX θ VARIATION m	PROFILE CURVE DROP
22-Jul	S2	-4	10	?	1200	NO
22-Jul	S3	-5.1	≈ 11.2	?	2000	YES
22-Jul	S4	-7	12.5	13.3	1200	YES
23-Jul	S6	1.3	6.3	3.6	<600	NO
23-Jul	S7	1.3	7.6	2.9	<600	NO
23-Jul	S8	1.1	7.2	4.2	<600	NO

From the downdraft speeds measured for S2, S3 and S4 only speeds in excess of -4 ms^{-1} were associated with drops in altitude in the balloon profile. Drops in the profile curve were proportional to the downdraft speeds as indicated in Table 4.3.

Table 4.3: Relationship between downdraft speed and drop in altitude.

BALLOON	DOWNDRAFT SPEED	DROP IN ALTITUDE
	ms^{-1}	m
S3	-4.764	20
S4	-5.029	38
S4	-7.063	161

4.11.3 Sub-wave features

The sub-wave observations for 22 July 2010 are classified according to unstable, turbulent and reversed flow layers in Figure 4.38 and those of 23 July in Figure 4.39. Unstable areas are identified from drops in θ values as was mentioned by Doyle & Durran (2007), Holton (1992) and Stull (1991). Turbulent areas are identifiable from the analysis of Richardson Numbers (Chan 2008; Gossard & Hooke 1975; Holton 1992; Huschke 1959). Reversed flow areas are likely areas where rotor activity took place (Grubišić & Billings 2007).

When the two figures are compared it is immediately apparent that no lee turbulence could be sustained according to the soundings on 23 July, while on 22 July all three soundings showed support for turbulence. The upper bound of reversed flow, thus rotors, occurred at higher altitudes on 22 than 23 July. Reversed flow was detected below the summit level, except for S2 where it occurred at the summit level. During 22 July turbulence could be sustained above the summit level during S4. All reversed flow was supported by evidence of increases in vertical velocity, proving according to Hertenstein & Keuttner (2005), the existence of type 1 rotors.

113
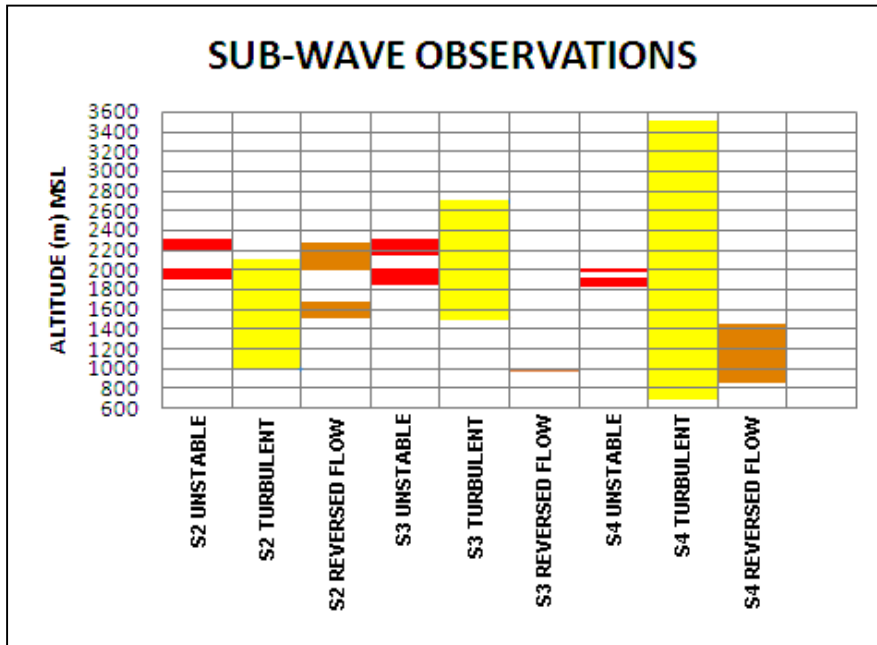
Figure 4.38: Sub-wave observations for S2, S3 and S4.
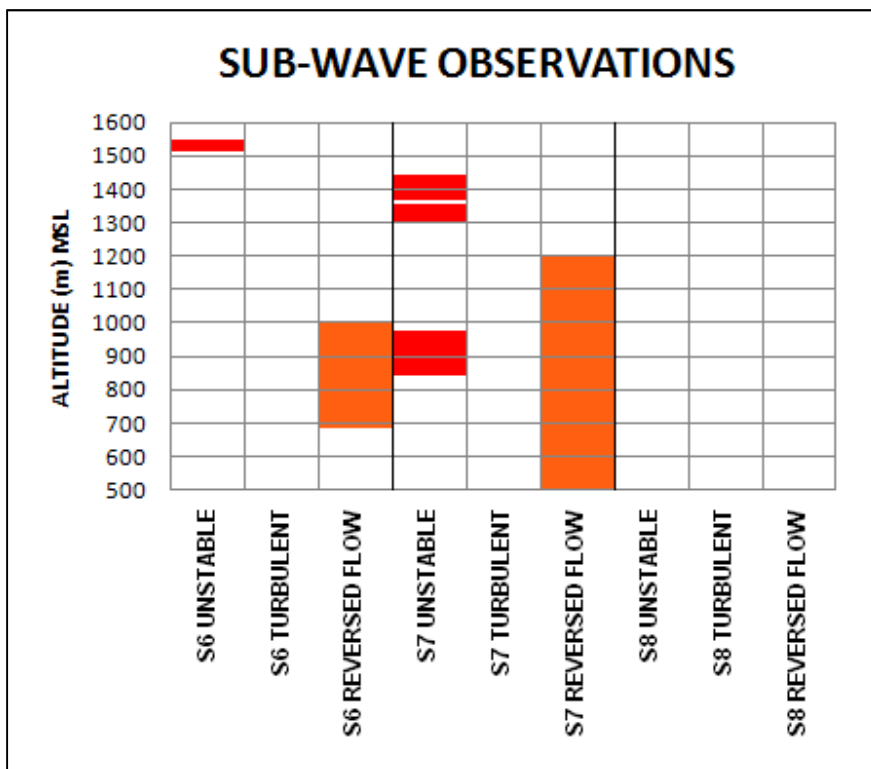
Figure 4.39: Sub-wave observations for S6, S7 and S8.

Rotor area data is tabulated in Table 4.4. Rotors were detected during each lee sounding. Each rotor was associated with updrafts, implying that the balloon on each occasion passed through the upwind part of the rotor. Updraft velocities on 22 July were far greater than those on 23 July. Thus a clear degeneration of sub-wave features is also observed in the 23 July post frontal weather.

Table 4.4: Vertical velocity and horizontal distance of reversed flow areas.

DATE	SOUNDING	CHANGE IN V.VELOCITY ms⁻¹	MAX V.VELOCITY ms⁻¹	HORIZONTAL DISTANCE m
22-Jul	S2	0.48	2.96	50.0
22-Jul	S2	1.62	3.35	190.0
22-Jul	S3	-0.92	3.99	1.8
22-Jul	S4	2.1	6.2	140.0
23-Jul	S6	0.16	0.04	60.0
23-Jul	S7	1.08	0.52	110.0

Near perpendicular upwind wind direction as well as greater trough line tilt, were features associated with better developed mountain wave features of 22 July 2010. Nevertheless the predominantly westerly upwind conditions of 23 July still yielded mountain waves as well as sub-wave features.

The y-component horizontal vorticity (η) graphs indicated small amounts of negative η in areas where reversed flow took place. It could be proven that positive η values were dominant in rotor areas and the occurrence of the negative values can be explained by the existence of small areas of negative η which are situated in the rotors (Doyle & Durran 2007; Hertenstein & Kuettner 2005). Table 4.5 summarises the negative η values detected in the soundings during reversed flow and shows that there appears to be no clear link between the magnitude of negative η values and the displacement within rotors as measured by the balloons.

Table 4.5: y-component vorticity.

SOUNDING	η	VERTICAL DISPLACEMENT	HORIZONTAL DISPLACEMENT
	s^{-1}	m	m
S2	-0.03	100	50
S2	-0.03	250	190
S3	0.12	60	1.8
S4	-0.04	600	140
S6	0.005	320	60
S7	-0.005	700	110

The most significant η data was recorded during S4 with very strong positive η values measured on the upwind side of a rotor. This was followed by a drop in the balloon's altitude, which was clearly marked by a negative η value. The magnitude of this positive η values compares well with NWP data of a type 1 rotor as displayed by Doyle & Durran 2001 (Appendix B, Figure B4).

A second field trip was conducted over 17 and 18 September 2010. The methodology and results of the first field trip was dealt with in great detail in Chapters 3 and 4. Rather than discussing details of every meteorological phenomenon of each subsequent sounding, the following chapter will summarise the significant findings of the soundings of 17 and 18 September 2010. A detailed synoptic discussion will be included as the synoptic conditions of the second field trip were significantly different from that of the first.

CHAPTER 5 FIELD WORK 17 AND 18 SEPTEMBER 2010

One of the research objectives of this study was to forecast suitable weather events during which field work could be conducted. Following the successful measurement of rotors in pre-frontal and post-frontal conditions, a cut-off low system was forecasted for 17 and 18 September 2010 which could possibly lead to the development of mountain waves.

5.1   Surface conditions on 17 September 2010 (NCEP reanalysis)

Figure 5.1 shows the sea level pressure isobars for 06:00 and 18:00 GMT for 17 September 2010. There was a high pressure system situated just south of the country. The low pressure over Namibia at 06:00 GMT deepened from 1014 hPa to 1010 hPa with the trough line (blue dotted line) extending a trough of low pressure from Namibia into the Western Cape by 18:00 GMT. There were no visible fronts, thus an entirely different surface weather system than that of 22-23 July was in place. According to the placement of the isobars, the surface winds (blue arrows) near the study area were approximately NE at 06:00 GMT and E at 18:00 GMT (Lankford 2000).
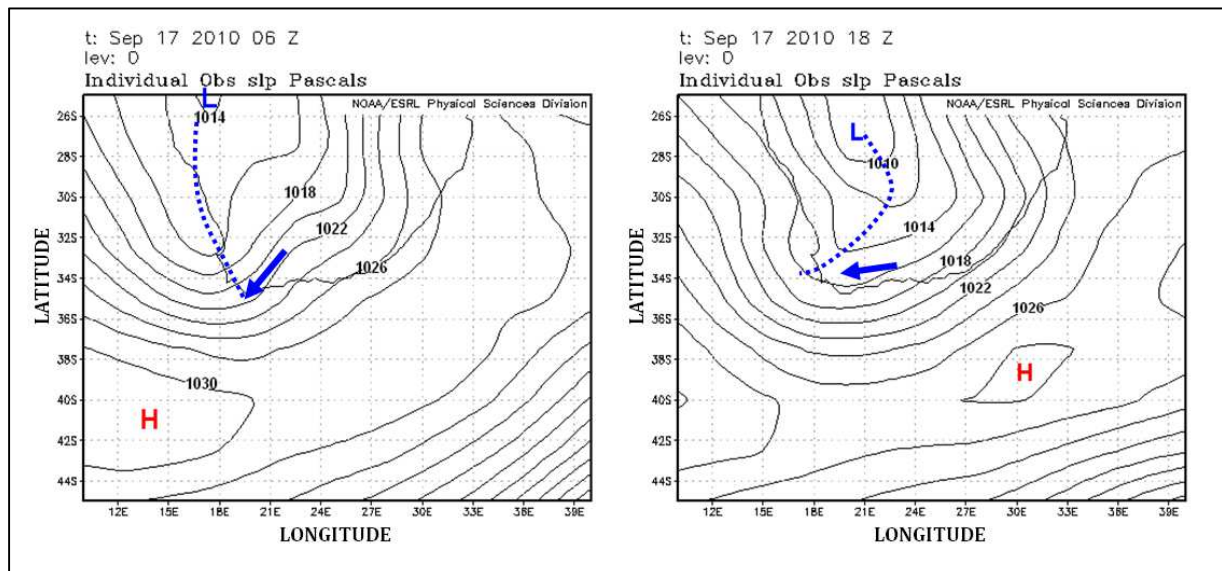
Source: NCEP Reanalysis (2011)

Figure 5.1: Sea level pressure for 06:00 and 18:00 GMT on 17 September 2010.

5.2   Upper air conditions on 17 September 2010 (NCEP reanalysis)

In Figure 5.2 the 06:00 GMT 850, 700 and 500 hPa geopotential height lines are respectively shown in boxes numbered 1, 2 and 3 with trough lines indicated by dotted lines. Likewise for 18:00 GMT the 850, 700 and 500 hPa geopotential height lines are shown in boxes 4, 5 and 6. At 06:00 GMT the trough lines leaned westwards with height. According to Highwood (2003) and Nielsen-Gammon (2010) the approximate 850 hPa wind direction (blue arrow) was NE while higher up at both 700 (green arrow) and 500 hPa (red arrow) it was NW. In box 3 a trough line is not yet visible at the 500 hPa level, but the wind direction is indicative of pre-trough upper winds. At 18:00 GMT all the height lines have advanced further east, still leaning westwards with height (boxes 4, 5 and 6). Wind directions remained more or less the same as for the 06:00 GMT period.
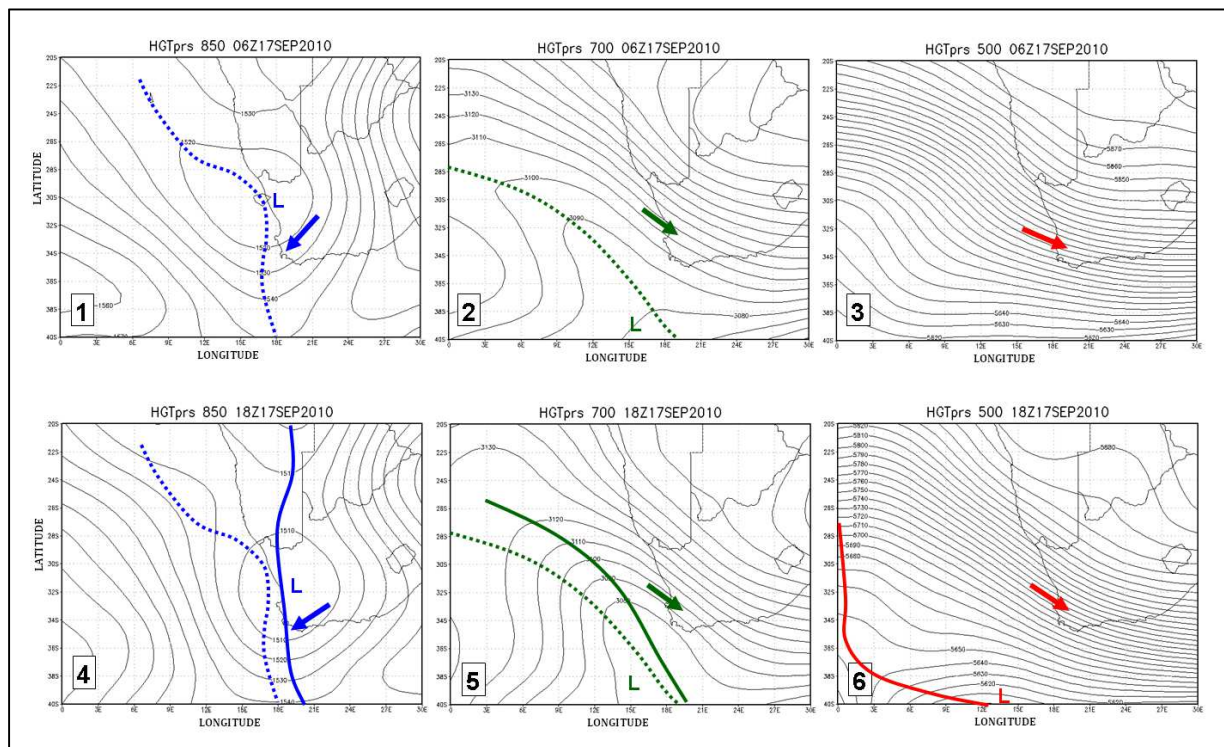
Figure 5.2: 850,700 and 500 hPa trough axes on 17 September 2010.

5.3   **Upper air conditions on 17 September 2010 (S9 data)**

S9 was the designated number for the upwind sounding on 17 September 2010. Figure 5.3 shows the upwind S9 sounding data. The wind direction below 1350 m above MSL did not fall within the favourable range for the development of mountain waves (yellow area). This low level direction was approximated well by the 850 hPa level as discussed in Section 5.2. However, the sounding data showed that the wind direction became favourable above 1350 m, 170 m below the actual 850 hPa level. The 700 and 500 hPa level wind estimation from Section 5.2 was indeed accurate (Figure 5.3). At the summit level the S9 wind speed was 12.8 ms^{-1} which according to Barry (1981) lies between the requisite wind speed for 1000 and 4000 m summits. With the summit of Matroosberg at 2251 m above MSL, it seems reasonable to assume that the wind speed was sufficient for the development of mountain waves.
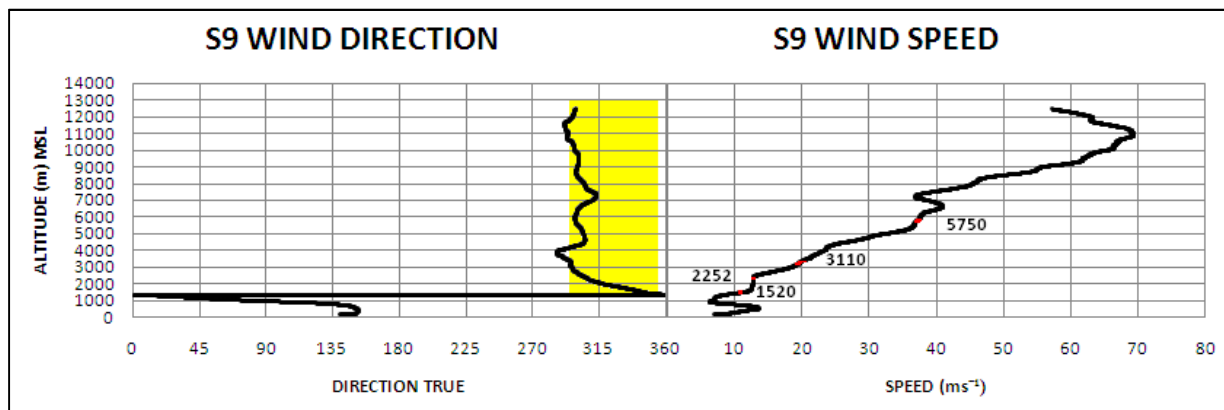
Figure 5.3: S9 wind direction and speed.

5.4   **Surface conditions on 17 September 2010 (SAWS data)**

Judging from the surface reanalysis in Section 5.1 the synoptic scale flow near the study area was south easterly. Figure 5.4 shows the surface wind direction for the closest stations to the study area. While Excelsior showed almost no clustering of data points about any one direction, Worcester showed a clear south easterly flow up to 10:00 GMT (see Figure B.1, Appendix B for map of the area). This was followed by slight veering to SSE and S which lasted until 16:00 GMT. The Worcester wind direction thus compliments the synoptic scale data well. The

Kwadousberg, north east of Worcester, would have sheltered the Hex River Valley from synoptic scale south easterly flow.
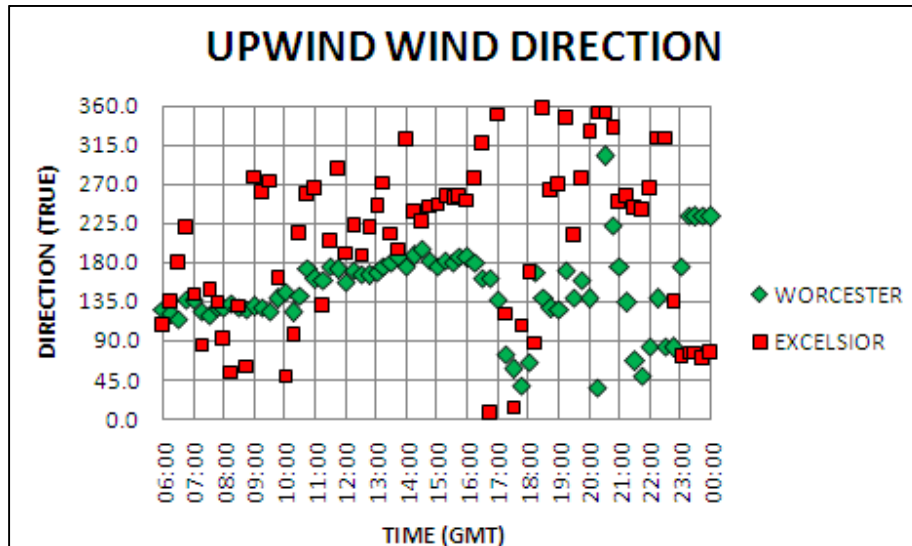
Figure 5.4: Surface wind direction near the study area

5.5 Sounding locations and objectives on 17 September 2010

The field work on this day was planned to investigate the effect that a developing cut-off low has on the formation of mountain waves. Three soundings were performed. S9 was the upwind sounding which provided potential temperature, Scorer parameter and lee wave length data. S10 and S11 were conducted in the lee of the Hex River Mountains and provided sounding profile, Richardson number, ascent rate, vertical velocity and isopleth data. The locations of launch sites are indicated in Figure 5.5. The upwind sounding site was moved further westwards in order to measure atmospheric conditions in an area less influenced by topography. This followed the experience of S1 and S5 where upwind atmospheric conditions measures were limited to altitudes below 4000 m above MSL. Following the pilot report received from the first field trip (Barker 2010, pers com), where turbulence was encountered at an altitude above 7000 m, the soundings were allowed to attain much higher altitudes. S10 was launched from the same site as S4 and S6. S11 shared a launch site with S8. Table 5.1 summarises the location, elevation and launch time data for each launch site.
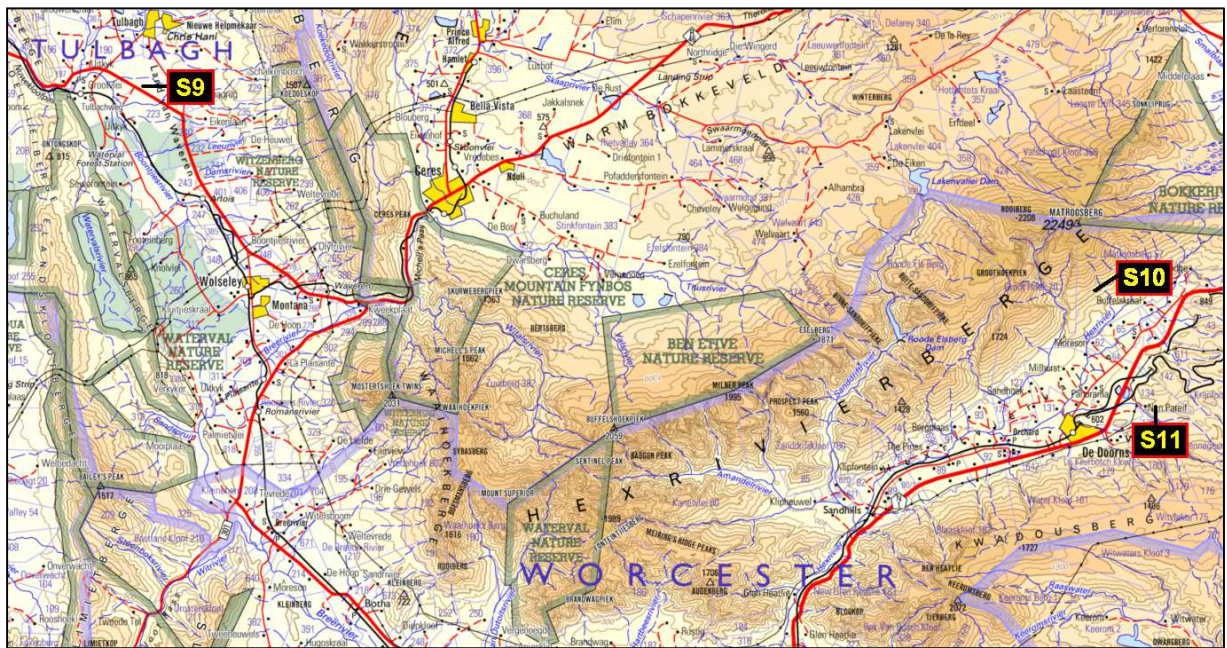
Source: Source: Chief Directorate Surveys and Mapping (2006)

Figure 5.5: Locations of launch sites for S9, S10 and S11

Table 5.1: Launch site data for S9-S11

SOUNDING	LATITUDE Degrees	LONGITUDE Degrees	ALTITUDE m MSL	TIME OF RELEASE GMT
S9	-33.3189	19.13607	172	07:30
S10	-33.4116	19.69926	688	10:40
S11	-33.4689	19.70656	568	16:06

5.6   On-site observations on 17 September 2010

During the S9 sounding parallel bands of altocumulus lenticularus cloud were observed to the east of the launch site. These cloud bands are marked 'L' in Figure 5.6 with an overlying band of cirrostratus (marked 'C') visible between the parallel bands. These waves were possibly produced by the flow over the Groot Winterhoek Mountains to the north of Tulbagh.
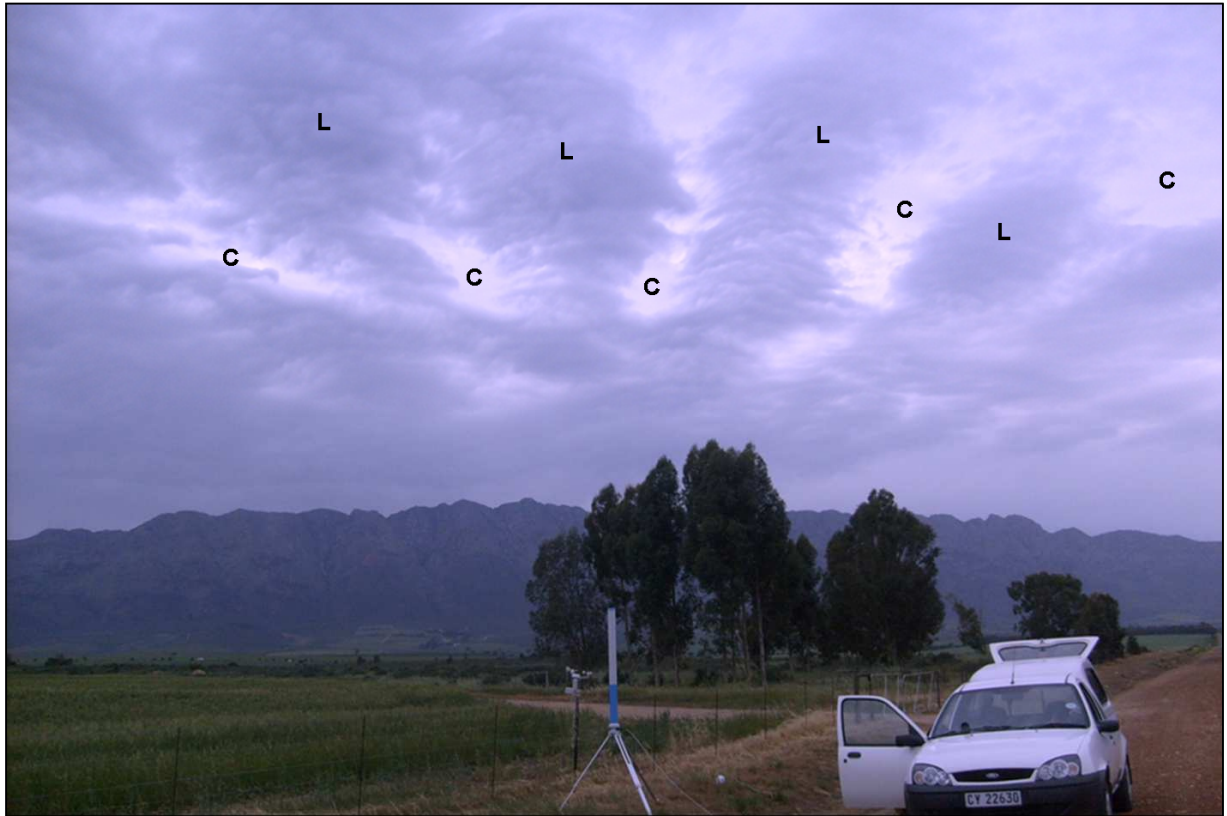
Figure 5.6: Lenticular cloud east of the S9 launch site.

In a study of a North American mid-latitude spring cyclone, Walcek (1994) found that approximately 60% of the 700 – 600 hPa layer was covered in cloud for an average layer relative humidity of 80%. The D-Met data for S9 showed 80% humidity between the 4500 – 5360 m above MSL. According to Lankford (2000) altocumulus clouds are typically found between 2000 and 6000 m above MSL. Thus the altocumulus cloud observation is well supported by the relative humidity data from S9.

The S11 data showed relative humidity approaching 75% at 4000 and again at 6000 m above MSL. During S11 altocumulus lenticularis was observed south westwards towards Worcester (Figure 5.7). At least seven mountain wave crests were observed, marked 1-7 from upwind side (right) to lee side (left).

Figure 5.7: Altocumulus lenticularis cloud to the south west of the study area.

5.7   Surface conditions on 18 September 2010 (NCEP reanalysis)

In Figure 5.8 the sea level pressure isobars for 06:00 and 18:00 GMT on 18 September 2010 are shown. The high pressure which dominated the previous day is confined to the north eastern corner of the country and over the study area the high pressure was replaced by an area of low pressure. From 06:00 GMT on 17 to 06:00 GMT on 18 September, the surface pressure near the study area dropped from 1020 hPa (see Figure 5.1) to 1016 hPa. The 06:00 GMT low pressure trough line is shown as a dotted blue line and that of 18:00 GMT as a solid blue line. During the day the trough line showed little movement, but a significant deepening in the low pressure took place over the eastern parts of the Western Cape. The surface pressure further dropped from approximately 1016 hPa to 1010 hPa. From the isobars the estimated wind direction near the study area was SE (blue arrows) for both time periods (Lankford 2000).
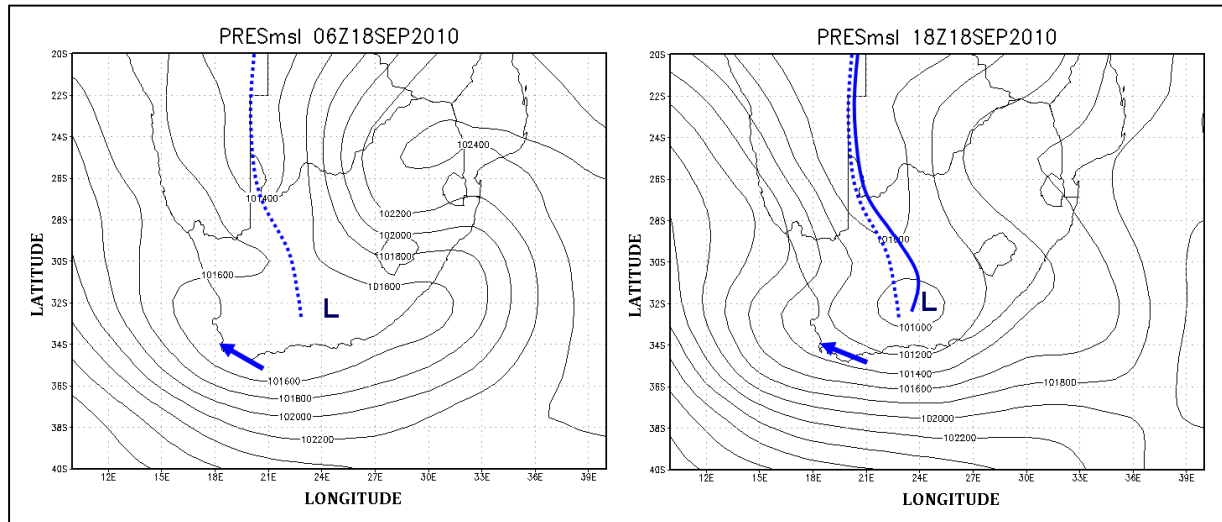
Figure 5.8: Sea level pressure for 18 September 2010

5.8   Upper air conditions on 18 September 2010 (NCEP reanalysis)

The geopotential height lines are shown in Figure 5.9 where boxes 1, 2 and 3 represent the 850, 700 and 500 hPa geopotential height lines for 06:00 GMT and boxes 4, 5 and 6 that of 18:00 GMT. At 06:00 GMT a closed low pressure area is shown at 850 hPa (light blue) with the trough line positions at 700 and 500 hPa indicated by green and red dotted lines respectively. These positions indicate that the trough system lay westwards with height. At 18:00 GMT closed low pressure areas are observed at all three levels. The original closed low at 850 hPa is again reproduced as a light blue area with the dark blue area (box 4) the 18:00 GMT position of the 850 hPa low. In box 5 and 6 the closed lows of the 700 and 500 hPa layers (green and orange respectively) are added. There is thus clear westward leaning of the low pressure areas with height at 18:00 GMT. These closed lows characterise a cut off low according to Singleton & Reason (2007). The upper air analysis for 17-18 September 2011 thus shows clear evolution from a steep upper trough to a cut-off low. According to Highwood (2003) and Nielsen-Gammon (2010) the approximate wind direction over the research area had an easterly component up to at least 850 hPa (blue arrows), after which it veers to north westerly at 700 and 500 hPa (green and red arrows).
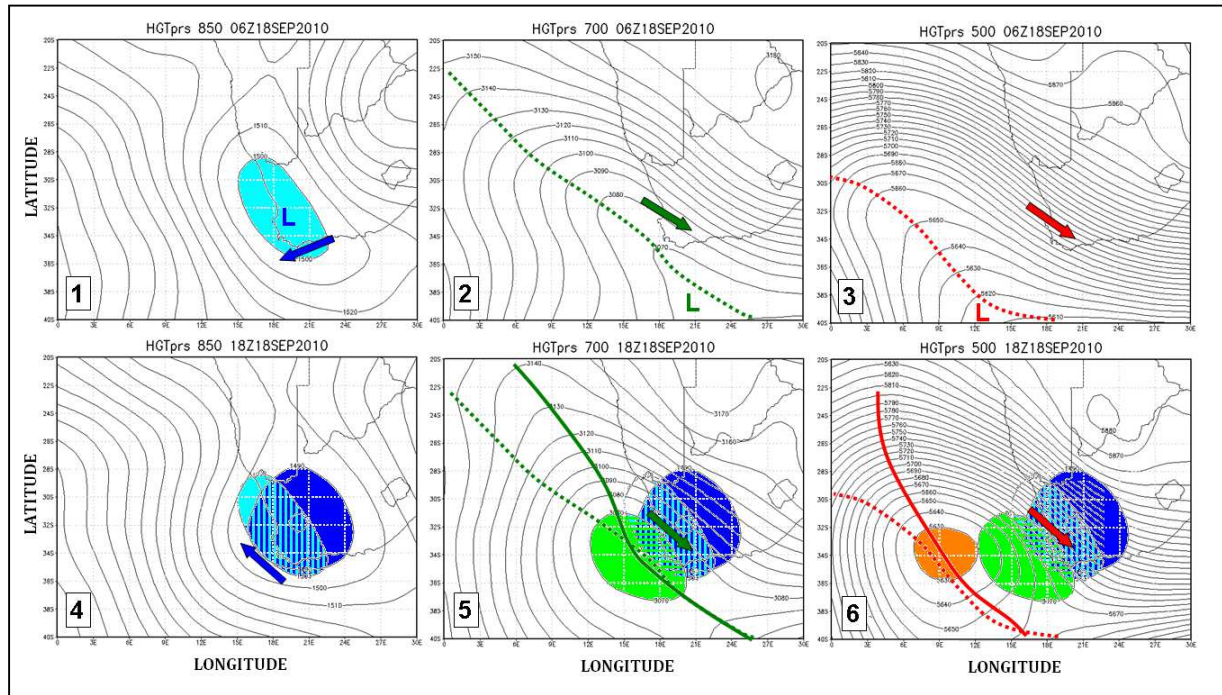
Source: NCEP Reanalysis (2011)

Figure 5.9: 850, 700 and 500 hPa geopotential height lines for 18 September 2010

Singleton & Reason (2007) further mention that cut-off lows have a pool of warm air in the upper troposphere above the closed lows and a cold pool below. Figure 5.10 represents the temperatures at different levels at 18:00 GMT on 18 September. The green line indicates the position of the cut-off low at the 500 hPa level. The 200 hPa warm pool at approximately 38 000 ft (orange and red) is situated above the cut-off low. The cold pool at this level lies over the central interior of South Africa. In the lower atmosphere below the cut-off low a cold pool is situated at the 850 hPa level west of the 850 hPa closed low (see Box 4 in Figure 5.9).
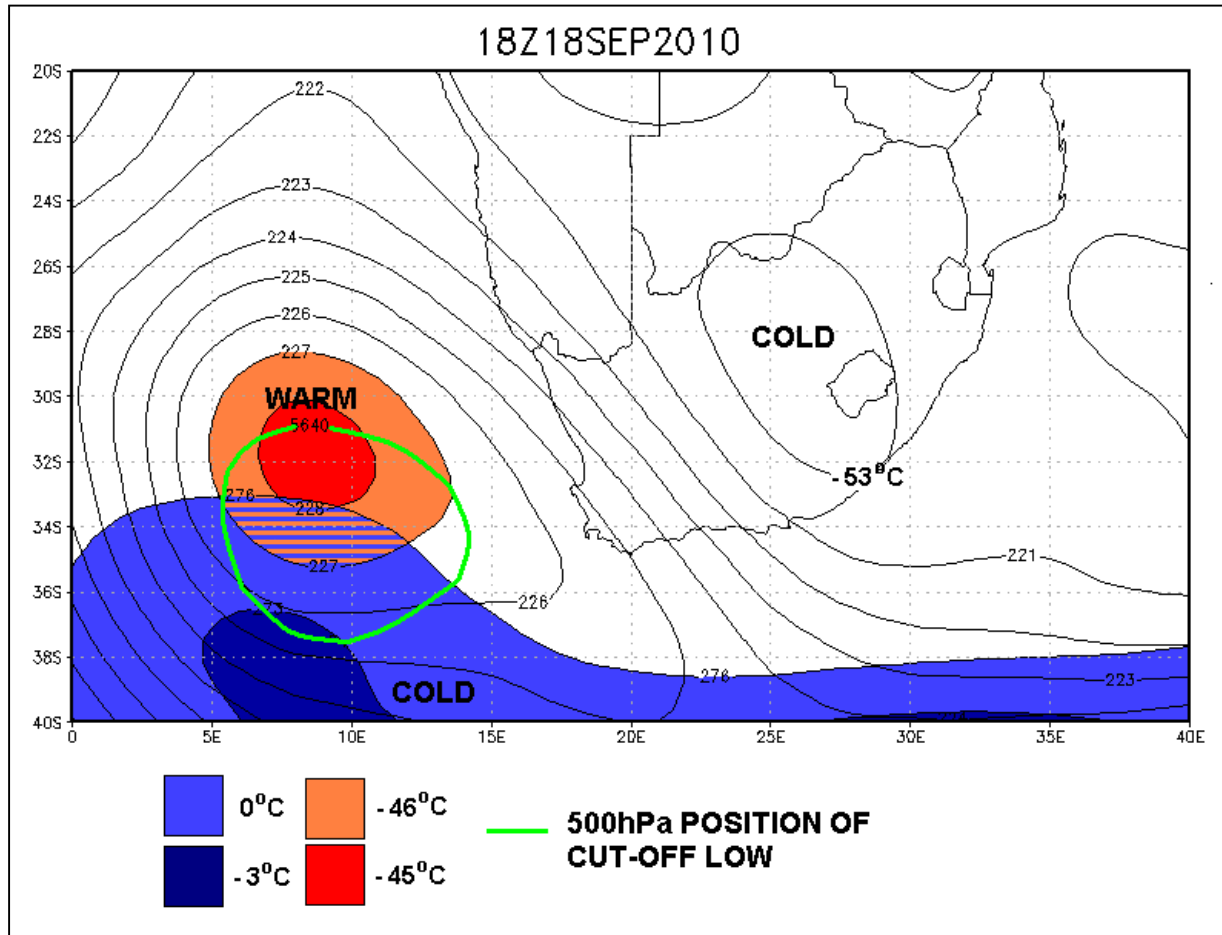
Source: NCEP Reanalysis (2011)

Figure 5.10: Cold and warm pools of air in relation to the cut-off low.

5.9   Upper air conditions on 18 September 2010 (S12 data)

The upwind balloon on 18 September 2010 was numbered S12. As was the case for the upwind sounding on 17 September, the S12 data in Figure 5.11 show SE low level winds (below 1180 m aboveMSL). These SE winds fell outside of the favourable range of directions (yellow area) for the development of mountain waves. This SE direction was predicted for the 850 hPa level, but from Figure 5.11 it is clear that the wind direction had veered to within the favourable range some 315 m below the 850 hPa level. When the upwind slopes of the Hex River Mountains were considered in Figure B.2 (Appendix B), it was found that the terrain along the entire distance from the 1200 m contour to the summit ridge experienced near-perpendicular flow on

18 September, while on 17 September only 76% of that distance experienced this flow. Vertically, taking an average ridge height of 1800 m above MSL, only the upper 75% of the upwind slope experienced near-perpendicular flow on 17 September, while the entire slope experienced this flow on 18 September.

The closest representative summit wind was measured at 2253 m above MSL and was 9.2 ms^{-1} in magnitude. This was less than the summit wind of the previous day but sufficient for mountains of 1000 m above MSL according to Barry (1991).
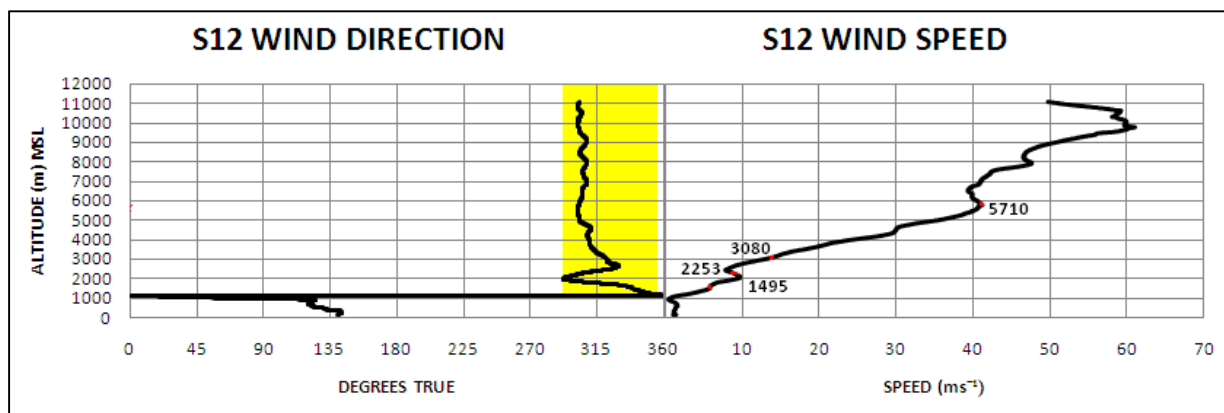
Figure 5.11: S12 wind direction and speed.

5.10   Surface conditions on 18 September 2010 (SAWS data)

Fifteen minute averaged wind direction for the nearest two SAWS weather stations is shown in Figure 5.12. Excelsior experienced mostly SW to W directions. As the synoptic scale surface winds were expected to be SE according to Section 5.7, channeling must have played a large part in governing the actual surface wind direction. The Worcester data shows better agreement with the general synoptic scale flow with an average SE flow for the entire day. Surface wind direction thus did not contribute to perpendicular flow NW of the Hex River Mountains. Like the case on 17 September the Kwadousberg north of Worcester would have sheltered the Hex River Valley from the synoptic scale south easterly wind.
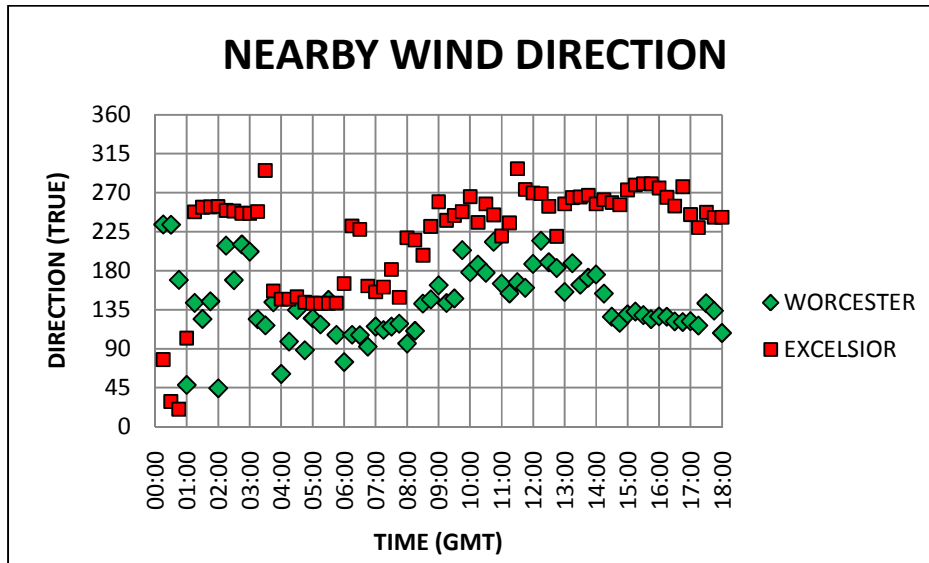
Figure 5.12: Wind direction close to the study area.

The soundings on 17 September 2010 were conducted with a low level high pressure system in place which was overlaid by an upper air trough that was developing into a cut-off low. As far as the upwind wind profile was concerned this synoptic situation lead to an increase in the amount of depth of perpendicular wind against the upwind slopes, with the entire slope experiencing perpendicular flow on 18 September as opposed to only the upper 75% on the previous day. Figure B.2 (APPENDIX B) and its associated discussion illustrate how this data was determined.   Below the 500 hPa level the upwind wind speed generally dropped from 17 to 18 September.

5.11   Sounding locations and objectives on 18 September 2010

The work on 18 September continued to investigate the effect of a cut-off low system on mountain wave development. The upwind sounding (S12) was again launched from near Tulbagh from the same site as S9. In the lee of the Hex River Mountains, S13 and S15 were launched from the near-mountain site used for S4, S6 and S10 in the hope to capture reversed flow. Both S14 and S16 were launched further downwind from the mountain in an effort to detect sub-wave features further downstream from the primary wave position. The launch site

locations are indicated in Figure 5.13. In Table 5.2 the positions and elevation of launch sites are tabled.
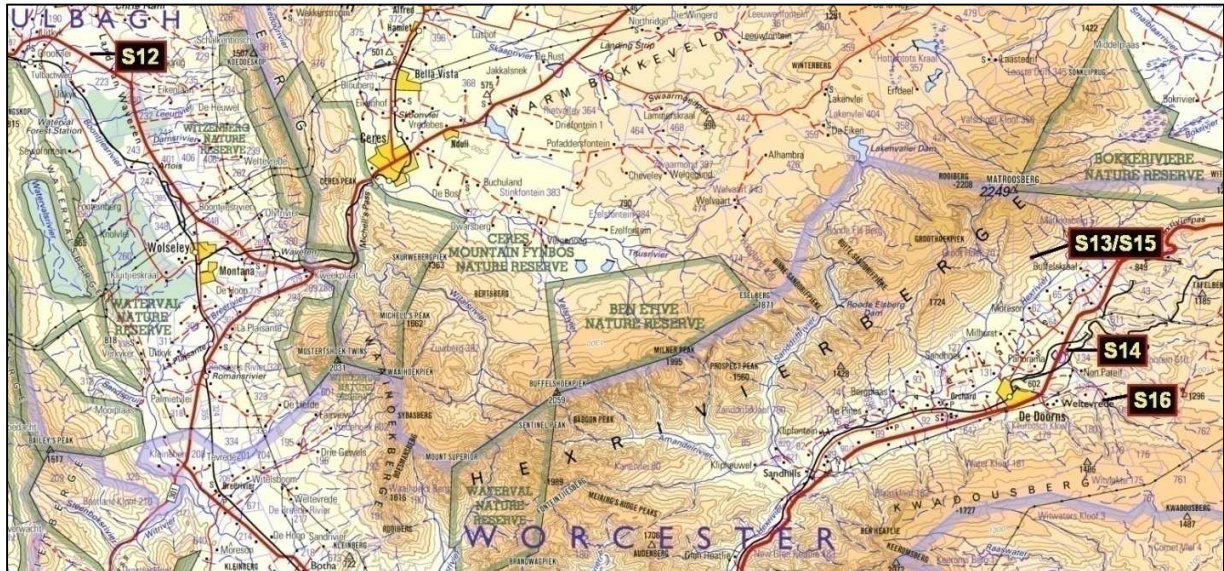
Source: Chief Directorate Surveys and Mapping (2006)

Figure 5.13: The location of launch sites for S12 – S16.

Table 5.2: Launch site data for S12-S16

SOUNDING	LATITUDE Degrees	LONGITUDE Degrees	ELEVATION m MSL	TIME OF RELEASE GMT
S12	-33.3189	19.13607	155	06:14
S13	-33.4116	19.69928	688	09:22
S14	-33.4581	19.69805	548	11:09
S15	-33.4116	19.69928	688	12:27
S16	-33.481	19.7223	646	14:30

5.12   On-site observations on 18 September 2010

During S14 Kelvin-Helmholtz (K-H) type instabilities were observed. According to Socolofsky & Jirka (2004:190) the Richardson number critical value 0.25 threshold: "provides a rule of thumb for the onset of Kelvin-Helmholtz instability." Doyle & Durran (2007) use the Miles-Howard condition $Ri < 0.25$, thus including negative values, to test for Kelvin-Helmholtz (K-H)

type of instabilities in the rotor region. According to Socolofsky & Jirka (2004) K-H instabilities can develop in areas of wind shear where a steep density gradient is created. Within such an area, which they term a picnocline, the density rapidly decreases with height while the wind speed increases with height. Small waves can become unstable and roll up into cloud billows.

Figure 5.14 shows the phenomenon photographed at approximately ten second intervals. Individual cloud billows formed from right (west) to left (east). The S14 data showed relative humidity approaching 75% at 4200 m above MSL. In addition the S14 Ri data also supports the development of K-H instabilities for all levels between 2500 and 6500 m above MSL, since Gramer (2007) states that $Ri < 0.25$ as a necessary condition for the existence of K-H instabilities. These K-H instabilities thus serve as visual evidence of rotor development within the S14 atmosphere. Mountain wave features were thus visible on both 17 and 18 September 2010 in the form of lenticular cloud and Kelvin-Helmholtz billows, respectively.

Figure 5.14: Kelvin-Helmholtz type cloud billows.

5.13   Data summary for 17 and 18 September 2010

5.13.1 Upwind data

As upwind soundings, S9 and S12 provided confirmation on the possibility of trapped lee wave formation on 17 and 18 September 2010 respectively. The data is summarized in Table 5.3. Both upwind soundings proved that trapped lee waves were likely to develop, as both Equation 2.4 and Equation 2.19 were satisfied. The wave amplitudes resulting from the theory of Lindsay (1962) compare very well with those obtained from Shun *et.al.* 2004.

Table 5.3: Upwind sounding summary

DATE	SOUNDING	Eq. 2.4 TEST	Eq. 2.19 TEST	AMPLITUDE (m) (Lindsay 1962)	AMPLITUDE (m) (Shun *et.al.* 2004)	λ (km) (Eq. 2.5)
17-Sep	S9	YES	YES	3000	2900 - 3700	7 -22
				4500	4500 - 4900	6.7 - 25.3
18-Sep	S12	YES	YES	2800	2700 - 3000	3.4 - 5.8
				3200	3200	7.1 - 23.8
				4000	4000	8.5 - 24.5
				5000	5000	7.8 - 23.3

5.13.2 Lee side main wave data

S10, S11, S13, S14, S15 and S16 supplied the lee side data. Table 5.4 summarizes the main mountain wave features for the second field trip. The JSP classification (Table 1.1) was again used with red, yellow and green indicating strong, moderate and weak waves respectively. Using the JSP classification proved more difficult than for the first field trip. Overall the vertical velocity was comparable to that of the post frontal data of 23 July. The wavelength increased overall reaching the strong JSP category for half the soundings. The downdraft positions yielded wavelengths in support of those taken from the ascent rate data. Variations in the isopleths are less accurate than those in Table 4.2. S15 in particular seemed likely to be classified as a moderate wave event. Once again due to the lack of South African data, this observation is rather subjective.

Wave crests were found to coincide with the positions where downdrafts started in cases where the maximum downdraft speed exceeded 1 ms^{-1}. This was the case for S10, S13, S14, S15 and S16. In the case of S11 and S13 the maximum downdraft was less than 1 ms^{-1} and wave crests in these soundings were found to coincide with the positions of maximum downdraft.

Table 5.4: Mountain wave features relevant to the classification used by JSP

DATE	SOUNDING	MAX U/D DRAFT m/s	λ S, H & M km	λ DOWNDRAFTS km	MAX θ VARIATION m	PROFILE CURVE DROP
17-Sep	S10	1.5	?	?	<600	NO
17-Sep	S11	1.4	15	?	<600	NO
18-Sep	S13	1.5	13	10-17	1000	NO
18-Sep	S14	2.7	12.7	12	<600	NO
18-Sep	S15	3.5	22	22	1400	NO
18-Sep	S16	1.2	5	6.2	1000	NO

5.13.3 Lee side sub-wave features

In Figure 5.15 the sub-wave observations are summarized for the atmosphere below 5000 m. Unstable layers were identified from potential temperature (θ) data, where drops in θ marks unstable areas (red). Layers with Richardson numbers between 0 and 0.25 were identified as layers where turbulence could be sustained (yellow). Reversed flow data was taken from profile curves (orange).

Layers of instability were only detected in the S10 and S15 data. On both occasions it coincided with layers in the atmosphere where turbulence could be sustained. Turbulent layers below the 5000 m above MSL altitude were detected for all lee side soundings, except S13. S13 did experience a turbulent layer between 11 000 and 12 000 m above MSL.

Reversed flow was experienced on a number of occasions. As was mentioned in the synoptic discussions (Sections 5.6 and 5.10), the synoptic wind was sheltered from the Hex River mountains by the Kwadousberg to the southeast. Thus reversed flow must have been the result of a mechanism other than synoptic scale winds. In the case of S11 reversed flow commenced

during a downdraft period. This indicates that the balloon entered the upwind side of a rotor. S13 and S15 were launched from the same site. The S15 data from later in the day shows a continuation of the reversed flow (rotors) measured in the S13 case.

S16 experienced two separate reversed flow regions (rotors), both at higher altitudes than the other three reversed flows. This is indicative of sub-wave formation (Doyle & Durran 2007). The balloon experienced downdrafts in the lower region and updrafts in the upper region. The balloon thus moved through the downwind side of the lower sub-rotor (downdraft area) and then entered the upper sub-rotor on the upwind side (updraft area). Very small fluctuations in ascent rate were detected associated with the reversed flow.
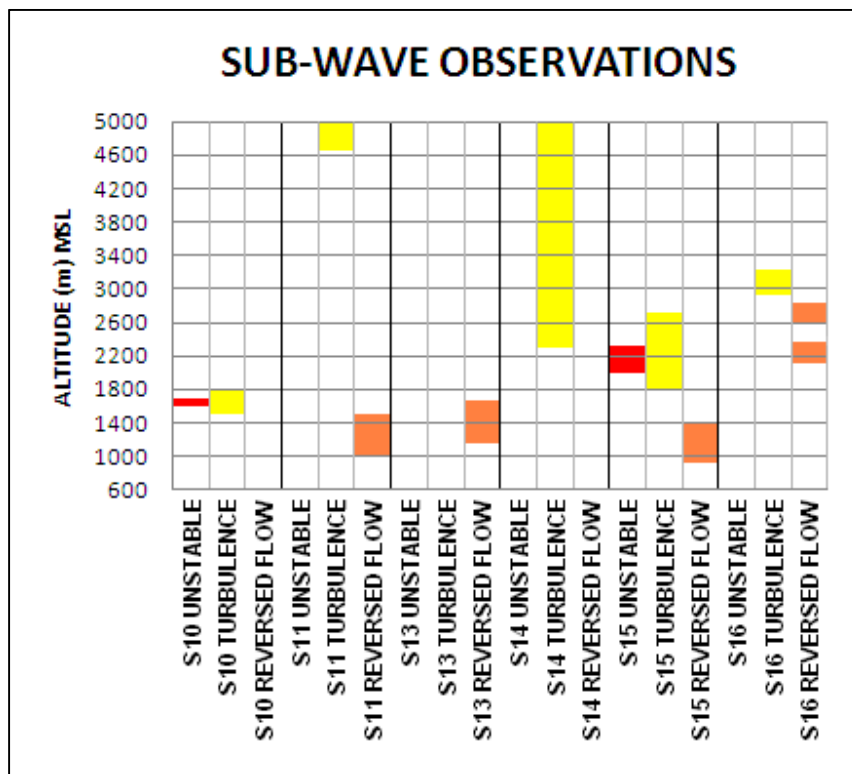
Figure 5.15: Sub-wave features detected on 17 and 18 September 2010.

Some reversed flow (rotor area) features are summarized in Table 5.5. Overall the changes in vertical velocity as well as the maximum updrafts were smaller than that experienced during the first field trip. The largest horizontal distance was covered by the S11 balloon on 17 September.

On 18 September the horizontal distances were on average half that of the S11 case. Both S11 and S16 experienced downdrafts during the reversed flow. Both S13 and S15 showed increases in updraft speed during reversed flow below the summit level, indicative of type 1 rotors (Hertenstein & Keuttner 2005). These fluctuations were much smaller in magnitude than those detected from the same launch site during the first field trip.

Table 5.5: Vertical velocity and horizontal distance of reversed flow areas.

DATE	SOUNDING	CHANGE IN V.VELOCITY ms^{-1}	MAX V.VELOCITY ms^{-1}	D.DRAFT IN FLOW	HORIZONTAL DISTANCE m
17-Sep	S11	0.86	0.86	YES	82.0
18-Sep	S13	1.85	2.1	NO	42.0
18-Sep	S15	0.39	0.53	NO	36.2
18-Sep	S16	0.32	0.46	YES	43.0

The y-component horizontal vorticity produced predominantly positive values η for 17 and 18 September but the data was much less impressive than that experienced in the frontal weather during the first field trip.

CHAPTER 6 CONCLUSIONS

Twelve lee side soundings were performed and in nine of these soundings mountain wave induced rotors (type 1 rotors) were detected. The detection of these rotors was based on reversed flow as well as fluctuations in the ascent rate and vertical velocity. Of the nine occurrences of rotors, eight showed horizontal flow upwind of 30 m or more.   The vertical depth of the reversed flow varied between 300 and 700 m. Two soundings detected sub-rotor development – one in prefrontal and a second under cut-off low conditions.

The y-component horizontal vorticity was predominantly positive, indicative of type 1 rotors. Negative y-component horizontal vorticity values could be explained as small scale features in the rotors or as part of the troughs of the main mountain waves situated above the rotor areas. Downdrafts associated with the rotors were detected in two soundings but were very small in magnitude. The analysis of data was thus sensitive enough to detect upwind and downwind sectors of small rotors. In one sounding the positive y-component horizontal vorticity was comparable to values relating to type 1 rotors. The balloon trajectory appeared to coincide with the upwind side of the rotor, preventing the stronger wind speed inside the rotor to be measured.

Rotors were most prominent in prefrontal synoptic conditions. They were less prominent in cut-off low conditions where the low level winds were not perpendicular to the lee side slopes. With the development of the cut-off low, the near perpendicular winds eventually reached down to the bottom of the upwind slope of the Hex River Mountains. This resulted in an increase in all mountain wave activity including rotors and sub-rotors.

6.1   Possible improvements to the methodology

Although this research has successfully measured mountain wave features in what seems to be the first South African study entirely dedicated to mountain wave turbulence, it failed to detect any strong downdrafts associated with rotor flow. Strong downdrafts of up to -7 ms^{-1} (moderate turbulence) were measured in the mountain waves above the rotor areas. In order to improve the chances of detecting rotor downdraft, it will be necessary to extract a profile curve from the data

onsite. Any reversed flow can then be used as a guide to better positioning of the equipment to do follow-up ascents at other sites. The soundings can be terminated at any point, buying enough time to possibly fit in three soundings at three nearby sites in as little time as one hour. The radio sondes can be set to 4 distinct frequencies, and second or third soundings do not run the risk of signal interference from previous balloons still airborne.

The greatest improvement that can be proposed to the methodology is to calculate the data using a north east southwest coordinate axis. This will be very close to the orientation of the Hex River Mountains and should improve the quality of data.

6.2   Other possible study areas

This balloon methodology used a very portable, highly advanced and reasonably inexpensive technology to detect atmospheric conditions pertaining to mountain waves. Pilots flying near the George Airport in the Western Cape often have to deal with mountain induced turbulence. Reports of mountain waves east of the Sneeuberg in the Eastern Cape seem to indicate that mountain wave downdrafts are at times strong enough to cause pilots to lose altitude to levels below the mountain ridges. These areas could therefore be possible sites for further researching South African mountain waves.

REFERENCES

Air Ministry Meteorological Office 1960. *Handbook of Aviation Meteorology*. London: Her Majesty's Stationary Office.

Alaka MA(ed) 1968. The airflow over mountains. Geneva: *World Meteorological Organisation Technical Note* no 34.

American Meteorological Society 2010: Glossary of Meteorology 2nd ed [Online]. Available from: http://amsglossary.allenpress.com/glossary [Accessed 14 February 2010].

Ansmann A, Fruntke J & R. Engelmann R, 2010. Updraft and downdraft characterization with Doppler lidar: cloud-free versus cumuli-topped mixed layer. *Atmospheric Chemistry and Physics* 10: 7845–7858.

Atkinson BW 1981. *Meso-scale atmospheric circulation.* London: Academic Press Incorporated.

Aviation safety network 2010. *ASN aviation safety database* [Online]. Available from: http://aviation-safety.net/database/record.php?id=19921209-1 [Accessed 4 April 2010].

Barry RG 1981. *Mountain weather and climate.* 2rd ed. New York: Methuen and Co.

Breedlove G & Fraser F 2011. Environmental potential atlas for the Western Cape [Online]. Available from: http://www.environment.gov.za/enviro-info/prov/other/wcmount.jpg. Accessed on 18 August 2011.

Brinkman WAR 1974. Strong downslope winds at Boulder, Colorado. *Monthly Weather Review* 102: 592-602.

Caccia JL, Benech B & Klaus V 1997. Space-time description of nonstationary trapped lee waves using ST Radars, Aircraft, and Constant Volume Balloons during the PYREX Experiment. *Journal of the Atmospheric Sciences* Vol 54, No 14: 1821-1833.

Carrera, ML, Gyakum JR & Lin CA, 2009. Observational study of wind channeling within the St. Lawrence River Valley. *Journal of Applied Meteorology and Climatology* 48: 2341–2361.

Cassano J 2010. Atmospheric thermodynamics [Online]. Department of Atmospheric and Oceanic Sciences, University of Colorado at Boulder. Available from: http://atoc.colorado.edu/~cassano/atoc5050/Lecture_Notes/wh_ch3_part1.pdf. [Accesses on 3 September 2010].

Cavcar M 2011. *International Standard Atmosphere* [Online]. Available from: http://home.anadolu.edu.tr/~mcavcar/common/ISAweb.pdf. [Accessed 24 July 2011].

Chan PW 2008. Determination of Richardson number profile from remote sensing data and its aviation application. Proceedings of the 14th International Symposium for the advancement of Boundary Layer Remote Sensing held 23-25 June 2008, Copenhagen, Denmark. *IOP conf series: Earth and Environmental Science* 1 (2008): 012043.

Chan PW & Tam CM 1996. Trapped Lee Waves over Lantau Island: Case Studies. *Hong Kong Meteorological Society Bulletin* 6, no 2: 41-55.

De Villiers MP & van Heerden J 2001. Clear air turbulence over South Africa. *Meteorological Applications 8: 119-126.*

Dortmund Data Bank Software and Separation Technology 2010. Saturated vapor pressure [Online] DDBST. Available from: http://www.ddbst.com/en/online/Online_Calc_vap_Form.php [Accessed 15 April 2011].

Doyle JD & Durran DR 2001. The dynamics of mountain wave induced rotors.   *Journal of the Atmospheric Sciences* 59: 186 – 201.

Doyle JD & Durran DR 2007. Rotor and subrotor dynamics in the lee of three-dimensional terrain. *Journal of the Atmospheric Sciences* 64: 4202-4221.

Doyle JD, Grubišić V, Brown WOJ, De Wekker SFJ, Dörnbrack A, Jiang Q, Mayor SD and Weissmann M, 2009. Observations and Numerical Simulations of Subrotor Vortices during T-REX. *Journal of the Atmospheric Sciences* 66: 1229-1249.

Durran DR 1986. Another look at downslope winds. Part I: the development of analogs to supercritical flow in an infinitely deep, continuous stratified fluid. *Journal of the Atmospheric Sciences* 43:2527-2543.

Durran DR 2003. Lee Waves and Mountain Waves. *Encyclopedia of Atmospheric Science*: 1161-1170.

Ferguson NA 2010. *In the lee of giants: riding high on mountain waves* [Online]. Available from: http://www.nateferguson.com/glider.html [Accessed 30 March 2011].

Finney RL & Thomas GB, 1994. *Calculus.* 2nd ed. Reading: Addison-Wesley.

Flight simulation systems 2006. *Accident reports on DVD* [Online]. Available from: http://www.fss.aero/accident-reports/look.php?report_key=187 [Accessed on 4 April 2010].

Geerts B 1998. *Radio acoustic sounding system* [Online]. Available from: http://www-das.uwyo.edu/~geerts/cwx/notes/chap15/rass.html [Accessed 1May 2011].

Gossard EE & Hooke WH, 1975. *Waves in the atmosphere – Atmospheric infrasound and Gravity waves – their Generation and Propagation.* New York: Elsevier Scientific Publishing Company.

Gramer L 2007. *Kelvin-Helmholtz Instabilities* [Online].
Available from: http://www.rsmas.miami.edu/users/isavelyev/GFD-2/KH-I.pdf. [Accessed on 18 July 2011].

Grubišić V & Billings BJ 2007. The intense lee-wave rotor event of Sierra rotors IOP 8. *Journal of the Atmospheric Sciences* 64: 4178 – 4201.

Grubišić V & Lewis JM 2004. Sierra Wave Project revisited: 50 years later. *Bulletin of the American Meteorological Association* 85: 1127 - 1142.

Hertenstein RF & Keuttner JP 2005. Rotor types associated with steep lee topography: influence of the wind profile. *Tellus* 57A: 117-135.

Highwood E 2003. *Lecture T5: Thermal wind shear* [Online]. Available from: http://www.met.reading.ac.uk/aer/MT11B/T5.doc. [Accessed on 7 July 2011].

Holmboe J & Klieforth H 1957. *Investigations of mountain lee waves and the air flow over the Sierra Nevada.* Los Angeles: University of California, Department of Meteorology.

Holton JR, 1992. *An introduction to dynamic meteorology*, 3rd ed. San Diego: Academic Press.

Huschke RE (ed) 1959. *Glossary of Meteorology*. Boston: American Meteorological Society.

Krause SS 2003. *Aircraft safety: Accident investigations, analysis and applications*. 2nd ed. New York: McGraw-Hill.

Koch SE, Bernardet LR, Jamison BD & and Brown JM 2006. Modeling of mountain waves in T-REX. Proceedings of the 12th Conference on Mountain Meteorology. Meeting held 28 August-1 September 2006, Santa Fe, NM, *American Meteorological Society*.

Kuettner JP & Hertenstein RF 2002. Observations of Mountain-induced Rotors and related hypotheses: a review. Proceedings of the 10th Conference on Mountain meteorology and MAP. Meeting held 17-21 June 2002, Park City, UT, Amer. Meteor. *American Meteorological Society: 326 – 329.*

Lalas DP & Einaudi, 1980. Tropospheric gravity waves: their detection by and influence on rawinsonde balloon data. *Quarterly Journal of the Royal Meteorological society* 109: 855-864.

Lankford TT, 2000. *Aviation weather handbook.* New York: McGraw-Hill.

Leeb-du Toit 2006. *Cloudbase: a reference manual for glider pilots* [Online], Chapter 10(7). Worcester: Cape Gliding Club. Available from: http://www.cgc.org.za/downloads/cloudbase [Accessed on 3 March 2010].

Lilly DK & Klemp JB 1979. The effects of terrain shape on nonlinear hydrostatic mountain waves. *Journal of Fluid Mechanics* 95: 241-261.

Lilly DK & Zipster EJ 1972. The Front Range windstorm of 11 January 1972: A meteorological narrative. *Weatherwise* 25: 56-63.

Linacre E & Geerts B 1998. *The Reynold's, Richardson and Froude numbers* [Online]. Available from: http://www-das.uwyo.edu/~geerts/cwx/notes/chap07/reynolds.html [Accessed 25 June 2011].

Lindemann C, Heise R & Herold W 2008. Lee waves in the Andes region, Mountain Wave Project (MWP) of OSTIV. *Technical Soaring* 32: 3.

Lindsay CV 1962. Mountain waves in the Appalachians. *Monthly Weather Review* 90: 271-276.

Mahalov M, Moustaoui M & Grubišić V 2011. A numerical study of mountain waves in the upper troposphere, which according to and lower stratosphere. *Atmospheric Chemistry and Physics Discussion* 11: 4487–4532.

Mahoney MJ, 2008. *A discussion of various measures of altitude.* [Online]. Pasadena: Jet Propulsion Laboratory. Available from: http://mtp.mjmahoney.net/www/notes/altitude/altitude.html [Accessed 24 October 2011].

McHugh JP, Dors I, Jumper GY, Roadcap JR, Murphy EA & Hahn DC 2008. Large variations in balloon ascent rate over Hawaii. *Journal of Geophysical Research* 113: D15123.

Mobbs SD, Vosper SB, Sheridan PF, Cardoso R, Burton RR, Arnold SJ, Hill MK, Horlacher V & Gadian AM 2005. Observations of downslope winds and rotors in the Falkland Islands. *Quarterly Journal of the Royal Meteorological Society* 131, 329-351.

Muller B 2010. *Mountain and lee waves in satellite imagery.* [Online]. Available from: http://wx.db.erau/faculty/mullerb/Wx365/Mountain_waves/mountain_waves.html [Accessed 25 March 2012].

Nance LB & Colman BR 2000: Evaluating the Use of a Nonlinear Two-Dimensional Model in Downslope Windstorm Forecasts. *Weather Forecasting* 15: 715–729.

National Transportation Safety Board 2010. *Aviation Accident Report: Runway Side Excursion during Attempted Takeoff in Strong and Gusty Crosswind Conditions Continental Airlines Flight 1404, Boeing 737-500, NN18611, Denver, Colorado, December 20, 2008* [Online]. Available from: www.ntsb.gov/publictn/a_acc1.htm [Accessed on 15 April 2010].

National Transportation Safety Board 2006. *NTSB - Nov 2001 Aviation Accidents* [Online]. Available from: http://www.ntsb.gov/aviationquery/brief.aspx?ev_id=20011206X02358&key=1 [Accessed on 14 March 2010].

National Weather Service 2011. *National Weather Service Glossary* [Online]. Available from: http://www.crh.noaa.gov/glossary.php?letter=h. [Accesses on 24 August 2011].

Nielsen-Gammon J 2010. *Weather observation and analysis, Chapter 10: Geostrophic Balance* [Online]. Available from: http://atmo.tamu.edu/class/atmo251/book10geostrophic.pdf [Accessed on 7 July 2011].

Quinlan R & Wahl D 2010. *Experience with LIDAR performance in complex terrain* [Online]. Available from: http://windenergy.org.nz/documents/conference10/dwahl.pdf. [Accessed on 8 August 2011].

Reichmann H 1978. *Cross-country souring.* Santa Monica: Thomson Publications.

Reid, SJ 1972. An observational study of lee waves using radiosonde data. *Tellus* 24: 593-596.

Reklaitis GV 1983. *Introduction to material and energy balances.* New York: John Wiley & Sons Inc.

Sheridan PF & Vosper SB 2006. Numerical simulations of rotors, hydraulic jumps and eddy shedding in the Falkland Islands. *Atmospheris Science Letters* 6: 211-218.

Shun CM, Lau SY, Cheng CM, Lee OSM & Chiu HY 2004. *LIDAR observations of wind shear induced by mountain lee waves.* Proceedings of the 11th Conference on Mountain Meteorology and MAP Meeting 2004 held 21-25 June 2004, Mount Washington Valley, NH, USA.

Shutts GJ, Healy P & Mobbs SD 1994. A multiple sounding technique for the study of gravity waves. *Quarterly Journal of the Royal Meteorological Society* 120: 579-594.

Socolofsky SA & Jirka GH 2004. Special topics in environmental fluid mechanics: Chapter 11 [Online]. Zachry Department of Civil Engineering, Texas A & M University. Available from: https://ceprofs.civil.tamu.edu/kchang/ocen689/ocen689ch11.pdf.

South Africa 2000. *South Africa 1:250 000 sheet 3319 BC De Doorns.* Third edition. (Map). Cape Town: Chief Directorate of Surveys and Mapping.

South African Civil Aviation Authority 2010. Accident and Incident investigation – reports 2005 (Ref 7904) [Online]. Available from http://www.caa.co.za [Accessed on 2 August 2010].

Stromberg IM, Mill CS, Choularton TW & Gallagher MW 1989. A case study of stratified airflow over the Pennines using an instrumented glider. *Boundary-Layer Meteorology* 46: 153-168.

Stull RB 1991. Static Stability – an update. *Bulletin of the American Meteorological Society* 72: 1521–1529.

Veness C, 2010. *Calculate distance, bearing and more between Latitude/Longitude points.* [Online] United Kingdom: Movable Type Scripts. Available from: http://www.movable-type.co.uk/scripts/latlong.html.

Vieira A 2005. *Mountain Wave Activity over the Southern Rockies* [Online]. Albuquerque Center Weather Service Unit (CWSU): Albuquerque. Available from: http://www.srh.noaa.gov/media/abq/LocalStudies/MountainWavesUpdate.pdf. [Accessed 15 April 2011].

Vosper SB 2004. Inversion effects on mountain lee waves. *Quarterly Journal of the Royal Meteorological society* 130: 1723-1748.

Vosper SB & Mobbs SD 1996. Lee waves over the English Lake District. *Quarterly Journal of the Royal Meteorological society* 122: 1283-1305.

Walcek CJ 1994. Cloud cover and its relationship to relative humidity during a springtime midlatitude cyclone. *Monthly Weather Review* 122: 1021 – 1035.

Wang C & Chen GT 2002. Case Study of the Leeside Mesolow and Mesocyclone in TAMEX. *Monthly Weather Review* 130:2572-2592.

Welch A 1973. *Pilot's weather: A flying manual.* London: John Murray.

Wolyn PG 2003. *Mountain-wave induced windstorms west of Westcliffe, Colorado.* Proceedings of the 10th Conference on Mountain Meteorology held on 17-21 June 2002, Park City, UT, USA.

World Meteorological Organisation 2009. *Weather forecasting for soaring flight.* Geneva, Switzerland: Organisation Scientifique at Technique Internationale du Vol à Voile.

REFERENCES: PERSONAL COMMUNICATION

Barker D 2010 (dbarker@csir.co.za) 23 July 2011. RE: Mountain wave turbulence experienced near Beaufort West.   Email to D van der Mescht (deon.vandermescht@weathersa.co.za).

Bester A 2010. Member of Eastern Province Sailplane Club. Port Elizabeth. Interview on 21 February about rotor turbulence as experienced by glider pilots.

Cape Gliding Club 2010. Members of Cape Gliding Club. Cape Town. Meeting on 4 March about gliding conditions near the Hex River Mountains.

Davis J 2010 (jimdavis@telkomsa.net) 12 February 2011. RE: Significance of measured updrafts. Email to D van der Mescht (deon.vandermescht@weathersa.co.za).

De Coning E (Estelle.deconing@weathersa.co.za) 8 April 2011. RE: MSG Training. Email to D van der Mescht (deon.vandermescht@weathersa.co.za).

Elzinga N (starship@worldonline.co.za) 5 February 2010. RE: Crash of aircraft on Table Mountain. Email to D van der Mescht (deon.vandermescht@weathersa.co.za).

Malan L 2010: Widow of victim of aircraft accident in the Hex River Mountains. De Doorns. Interview on 23 July about Hex River Mountains aircraft accident.

Smit R (rian.smit@weathersa.co.za) 6 June 2011. RE: passage of the cold front on 23 July 2011. Email to D van der Mescht (deon.vandermescht@weathersa.co.za).

Uys W (wynand@ottersden.co.za) 11 February 2011. RE: effect of updraft speed on light aircraft performance. Email to D van der Mescht (deon.vandermescht@weathersa.co.za).

Wium TC 2010: Farmer in Hex River Valley. De Doorns. Interview on 17 September 2010 about weather in the Hex River Valley.

APPENDIX A: ADDITIONAL DEFINITIONS

A.1. Turbulence

In meteorology, turbulence is defined as irregular fluctuations that occur within the motions of fluids (AMS 2010). Holton (1992:117) describes turbulent flow to contain "irregular quasi-random motions".

A.2 Stability

Huschke (1959) states that stability and static stability is the same. The latter term is used by Barry (1981). Huschke further defines stable motion as motion where small perturbations do not grow in magnitude and unstable motion as motion where small perturbations grow (Stull 1991).

A.3 Radio acoustic sounding system.

A radio acoustic sounding system (RASS) consists of one or more vertically pointed loudspeakers, surrounded by focusing dishes and an antenna that receives the return signal from above. It is a remote sensing technique for the measurement of virtual temperature profiles (Geerts 1998).

A.4 LIDAR and SODAR

LIDAR is an acronym for Light Detection And Ranging (Quinlan & Wahl 2010). Quinlan & Wahl explain that this ground based device measures wind direction and speed by emitting a light source and measuring the backscattered light which is received at a different frequency due to the Doppler Effect.

According to Quinlan & Wahl (2010) SODAR (Sonic Detection and Ranging) measures wind speed and direction by emitting acoustic pulses. These pulsed are received as backscatter due to density fluctuations in the atmosphere and the data is translated into wind information.
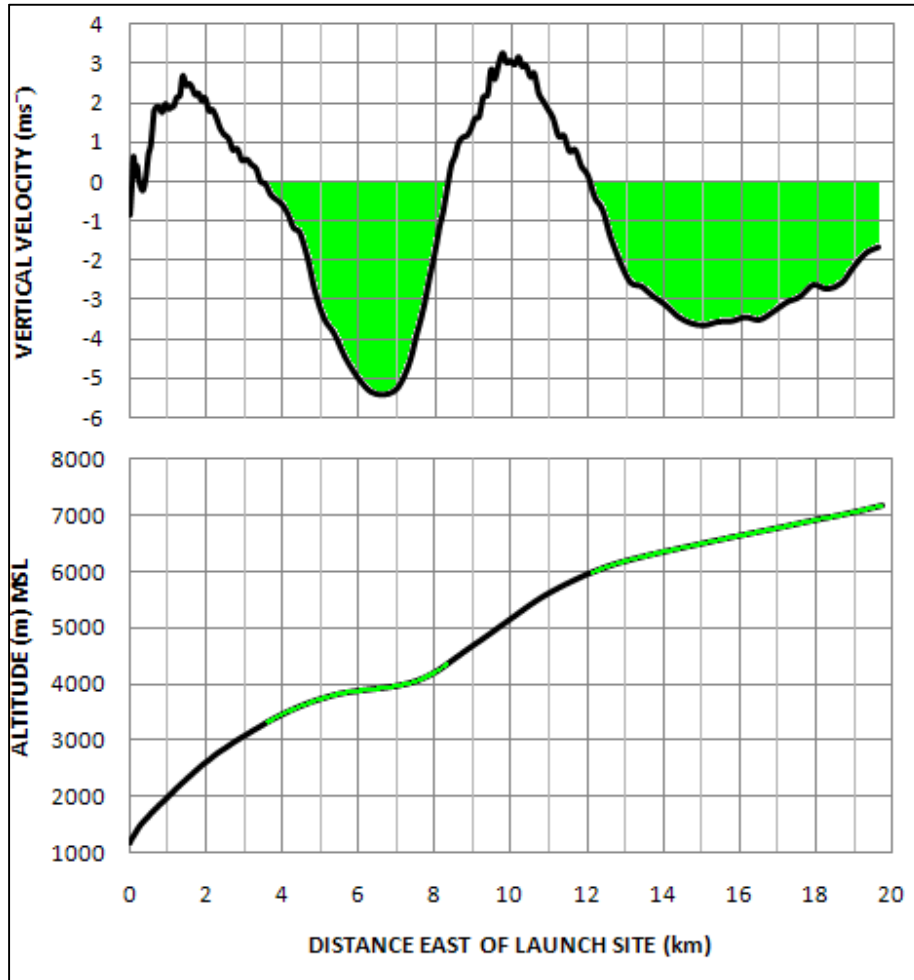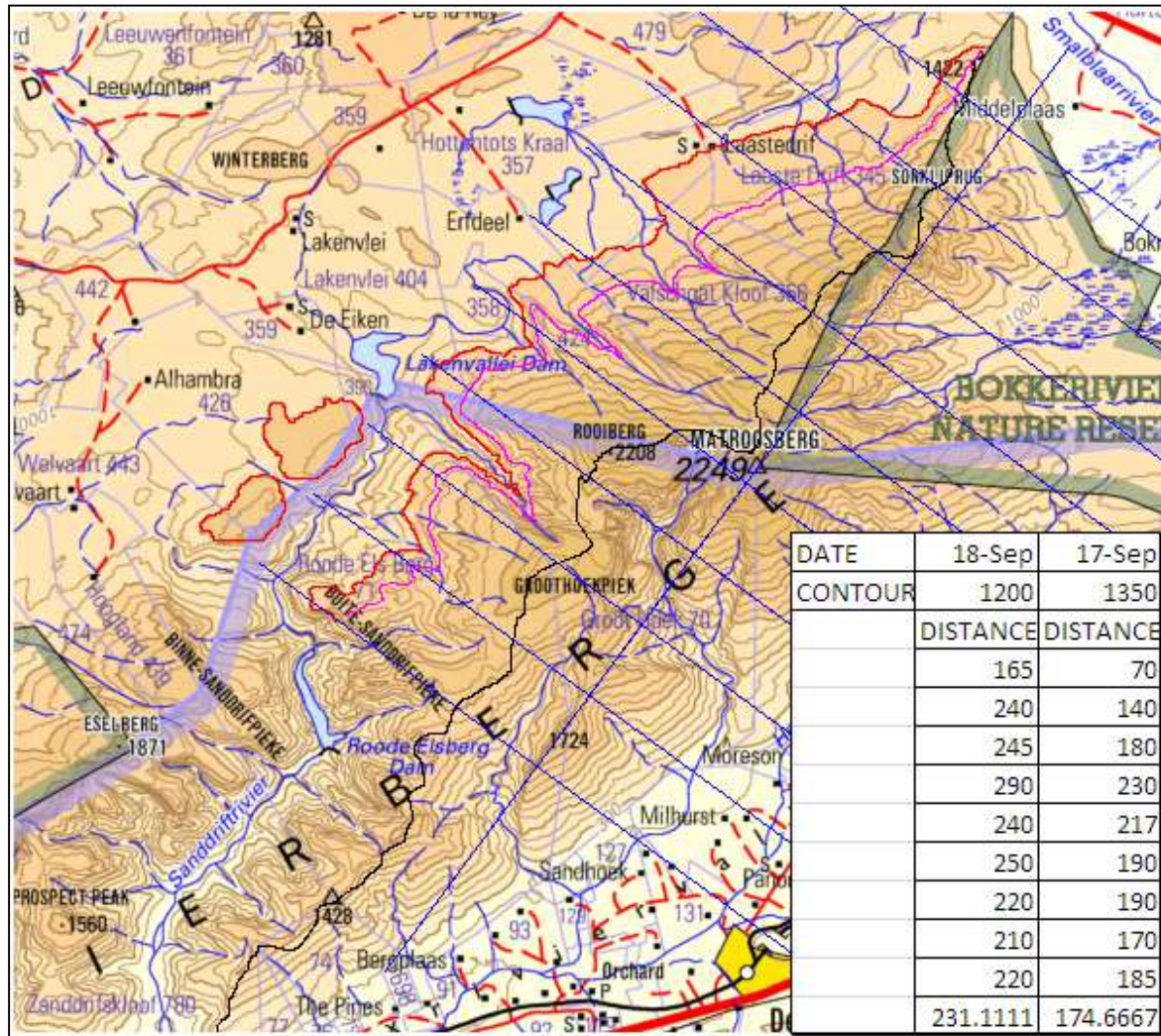
APPENDIX B: ADDITIONAL GRAPHICS

Figure B.1: Vertical velocity compared to profile curve for S1

| DATE	18-Sep	17-Sep
CONTOUR	1200	1350
	DISTANCE	DISTANCE
	165	70
	240	140
	245	180
	290	230
	240	217
	250	190
	220	190
	210	170
	220	185
	231.1111	174.6667

Source: Chief Directorate Surveys and Mapping (2006)

Figure B.2: Measurement of upslope distance.

In Figure B.2 a blue line is drawn from the bottom left to top right of the image. It shows the line and orientation used for distance calculations. Perpendicular lines to this line intersect the 1200 and 1350 m contours (red and pink lines) as well as the summit ridge, indicated by a black line. On 17 September perpendicular winds blew along the slope from the 1350 m elevation to the summit and from the 1200 m elevation on 18 September. This analysis allowed for the determining of the increase in perpendicular slope flow from 17 to 18 September.
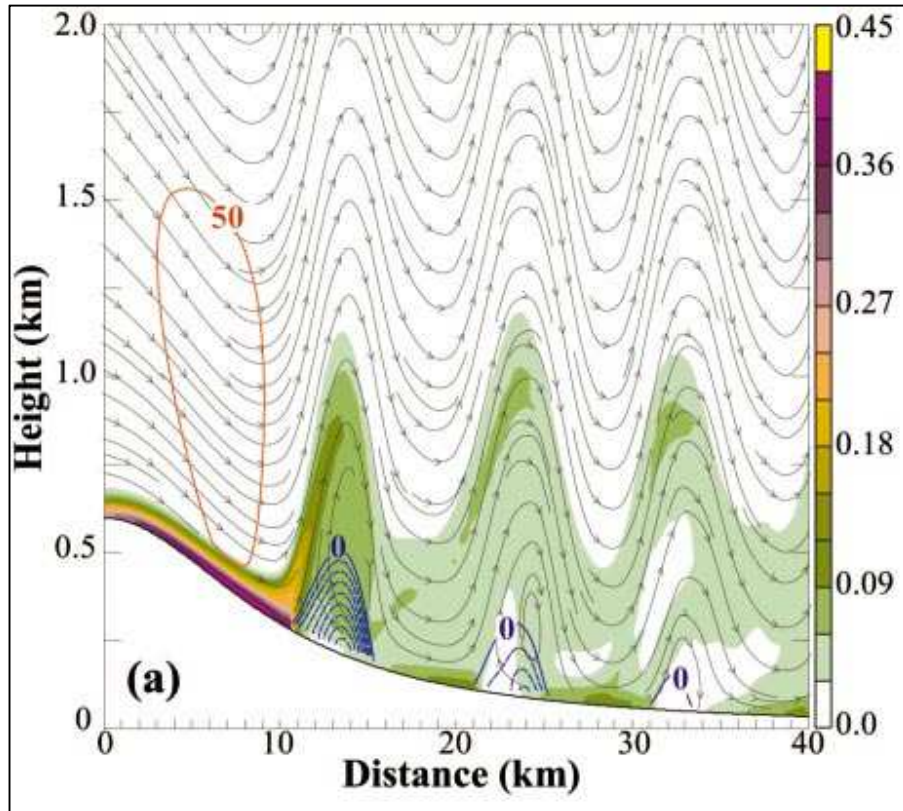
Source: Doyle & Durran 2001: 193

Figure B.3: y-component horizontal vorticity (values along the y-axis of the graph) and reversed flow speed. (blue contours)
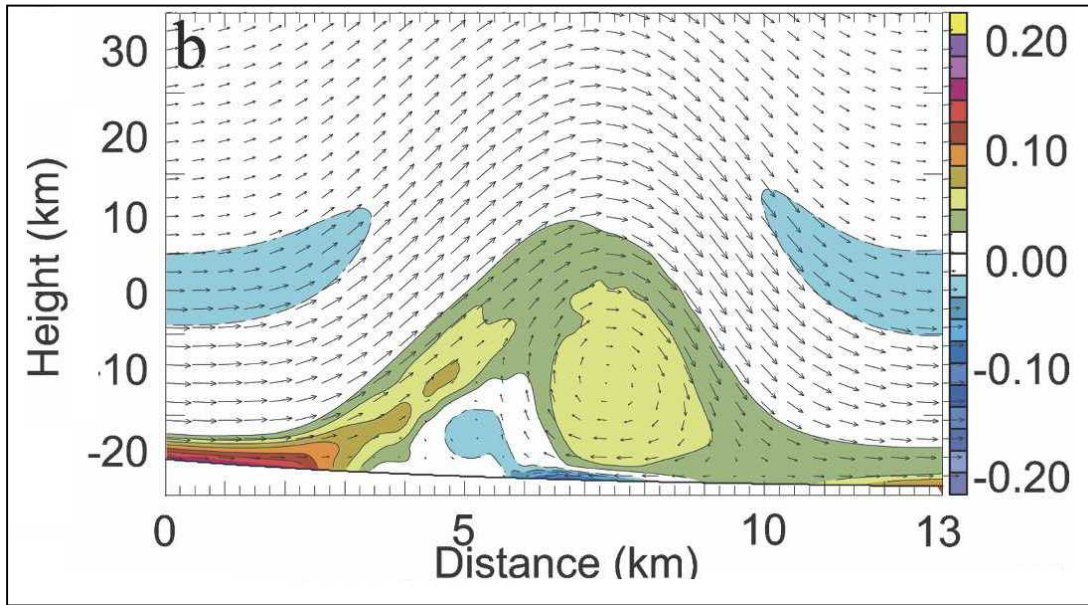
Source: Doyle & Durran 2007: 4208

Figure B.4: y-component horizontal vorticity (values along the y-axis of the graph).